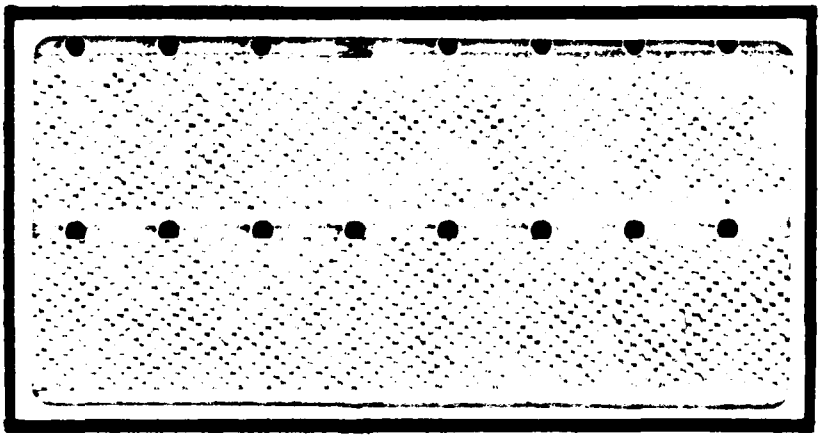

DEPARTMENT OF THE AIR FORCE

AIR UNIVERSITY

AIR FORCE INSTITUTE OF TECHNOLOGY

Wright-Patterson Air Force Base, Ohio

AFIT/DS/PH/83-2

FAR FIELD FALLOUT PREDICTION TECHNIQUES

DISSERTATION

Winfield Scott Bigelow, Jr.
Major USAF

AFIT/DS/PH/83-2

This work sponsored by the Defense Nuclear Agency
under RDT&E RMSS Code B325079464 V99QAXNA01111 H2590D

AFIT/DS/PH/83-2

FAR FIELD FALLOUT PREDICTION TECHNIQUES

DISSERTATION

Presented to the Faculty of the School of Engineering

of the Air Force Institute of Technology

Air University

In Partial Fulfillment of the

Requirements of the Degree of

Doctor of Philosophy

Winfield Scott Bigelow, Jr., B.S., M.S.

Major, USAF

December 1983

AFIT/DS/PH/83-2

FAR FIELD FALLOUT PREDICTION TECHNIQUES

Winfield Scott Bigelow, Jr., B.S., M.S.
Major, USAF

Approved:

Charles J. Bridgman, Chairman — 9 Dec 83

George John — 9 Dec '83

George D. Nickel — 28 Nov 83

Charles W. Richard, Jr. — 9 Dec '83

John F. Prince — 9 Dec 83

David L. Auton — 5 Dec. 83

Accepted:

J. S. Przemieniecki — 9 Dec. 1983
Dean, School of Engineering

Acknowledgment

I am especially indebted to Dr. Charles J. Bridgman, whose advice, support, and encouragement helped me to complete this work. His active interest in fallout prediction was invaluable. I also wish to thank Dr. David L. Auton of the Defense Nuclear Agency. In addition to providing sponsorship of my research, he arranged for me to receive the DELFIC computer code and instruction in its use. Finally, I must acknowledge the support of my wife, Faith, who assumed a greater burden at home, while I concentrated on completing this work.

W. S. Bigelow, Jr.

Contents

List of Figures

List of Tables

Abstract

A calculational technique for use in predicting fallout far downwind from nuclear bursts is developed and validated. Possible siting strategies for the next generation of missiles might invite a concentrated attack by thousands of nuclear warheads. Th resulting fallout field could consist of the superposition of thousa of single burst patterns. The downwind extent of damaging radiation vels would extend beyond the distances to which calculations are usual erformed for single bursts. Numerical models currently available cannot be extended to these large downwind distances because of the artificial pattern break up inherent in their numerical quadrature and because of prohibitive computing requirements. Two approaches to this problem are taken here. First, a numerical smoothing which conserves radioactivity is developed to help prevent pattern break up. This is partially successful in that it extends the predictive range farther downwind, but not far enough. The second approach is to abandon the numerical quadrature -- known as disc tossing -- and adopt a whole cloud smearing approach. The key function needed for the smearing approach, the fractional arrival rate of activity on the ground, is derived directly from physical principles and validated by comparison with an extensive series of numerical (disc tosser) predictions. The prediction of activity arrival rate appears to be successful; the smearing model results agree with the numerical method over a wide range of weapon yields and activity distributions. This function is also employed in a limited sensitivity study of particle size-activity distribution

effects on ground arrival of activity. This sensitivity study confirms that the range of carrier soil particle sizes available and the distribution of bomb activity over those particles is crucial in establishing the time history of fallout arrival. The smearing model is particularly sensitive to fractionation, defined here as the partition of activity between the volume and the surface of fallout particles.

FAR FIELD FALLOUT PREDICTION TECHNIQUES

I. Overview

Although fallout resulting from a nuclear attack against our existing strategic systems would unquestionably lead to significant damage to nearby civilian populations, the impact would be mitigated by the generally remote basing of the strategic missile forces. Post-attack fallout dose rates in the otherwise undevastated regions downwind of the burst point can reasonably be estimated by any one of several existing fallout models from information about the wind and either yield or exposure surveys. Possible future missile basing schemes, for example, the hotly debated MX missile system, present less tractable scenarios. Such schemes might invite a concentrated attack by thousands of nuclear warheads. The fallout field resulting from such an attack would consist of the superposition of thousands of single burst results. The downwind extent of lethal and incapacitating radiation levels would far exceed the distances for which calculations are now performed for single bursts. Otherwise competent single burst models now available for use in operational type studies cannot be extended to these large downwind distances because of the unrealistic fallout pattern break-up inherent in their numerical quadrature schemes, and because of prohibitive computer time and memory

requirements.

Most conventional fallout models either begin with or simulate the formation of a stabilized debris cloud consisting of radioactive entrained soil particles. The cloud is sectioned in the horizontal from base to top, defining a vertical stack of discs over ground-zero. For each disc, the constituent particles are grouped into a histogram by size. One-by-one, each group of particles from each disc is then tracked through prevailing winds until it reaches the ground some distance downwind. If the particle size and cloud quadratures are fine enough, there will be enough superposition of grounded discs to produce a reasonably accurate and smooth fallout pattern. Such codes are called disc tossers.

DELFIC is supreme among the disc tossers from the standpoint of modeling competency (1:7). In DELFIC, the rise, expansion, and stabilization of the debris cloud and the distribution of the entrained soil within it are all modeled dynamically. Cloud wafers are then transported to the ground through space and (potentially) time-varying wind fields using up-to-date models for particle fall rates and debris/atmosphere interactions. Activity is assigned to particles in the grounded wafers on the basis of empirical studies of debris samples from nuclear tests. Contributions from specific nuclides are computed by application of the Bateman equations to each fission product mass chain (2:242).

For all its sophistication, DELFIC is still plagued by one problem inherent to all disc tossers: generation of a realistic fallout pattern requires quadrature fine enough to guarantee that each point of

interest in the fallout field be overlaid by the contributions from several discs. As one follows the falling wafers farther and farther downwind, the grounding points of different particle size class wafers gradually separate until the wafers no longer overlap at all. As a result of this phenomenon, the MARK-V version of DELFIC required about 10000 wafers to adequately describe only the local fallout field (3:27). The original attempt by DELFIC's authors to alleviate this problem consisted of replacement of the original description of the horizontal distribution of activity within each disc as a constant, by a gaussian centered at the cloud vertical axis (1:31). In the resulting code, known as the ASA version of DELFIC, tops and bases of each monosized gaussian cloud wafer were transported separately to the ground. This eliminated discontinuities at the wafer edges and provided a greater horizontal extent to each wafer, thereby postponing the pattern break-up problem to points farther downwind. As a result, a given prediction could be computed with about half as many wafers as were required with the MARK-V version.

The approach taken by this author to extend DELFIC's capabilities yet farther downwind was to use an improved stratagem for transporting each wafer, so that its contents would be smeared over a more realistic area in the fallout plane. This wafer smearing or pattern smoothing technique is described in Chapter II. With wafer smearing, downwind voids were eliminated, and DELFIC's quadrature requirements were reduced by about a factor of five over those for the MARK-V version of the code. Local fallout patterns could be calculated reliably with only about 2000 cloud wafers.

Even with wafer smearing, pattern distortion and break-up remained a problem in attempts to calculate far field fallout. The logical extension of wafer smearing, whole cloud smearing and abandonment of the disc tossing concept, is described in Chapter III. In the development of this new calculational technique, DELFIC is discarded except as a comparison standard, and variable winds and the resulting curved pattern hotlines are sacrificed temporarily in the interest of providing an initial far field capability. In Chapter IV, the new smearing model is validated by comparison of its predictions for the rate of activity deposition with DELFIC's results for several yields and particle size-activity distributions.

An advantage of the smearing model is that it effectively decouples the various input parameters that determine fallout from one another. This makes practical sensitivity analyses such as that presented in Chapter VI.

II. Smoothing DELFIC Fallout Patterns

In the ASA (Atmospheric Sciences Associates) version of DELFIC, there is in the cloud at stabilization time a wafer of debris particles corresponding to each unique particle size class and cloud altitude (1:19). The vertical coordinates of each wafer are determined dynamically during the cloud rise simulation by the competing forces of lift (produced by the buoyancy of the cloud) and of gravity on each size class of particles. The motion of the smallest particles in each size class determines the stabilization altitude of the wafer top; that of the largest particles determines the altitude of the wafer base. After cloud stabilization, however, the ASA version of DELFIC no longer considers the particle size class extrema. Instead, in the advection-plus-settling method of transport, the geometric mean size for the size class is used in the equations describing the transport of the size-class/cloud-altitude wafer to the ground. The wafer top and base are transported separately (their initial altitudes may be considerably different), with the mean particle size for the size class used in computing the top and base trajectories. When the wafer top and base have both impacted, the wafer contents are smeared over the area between the top and base grounding locations. The resulting "footprint" of an individual wafer conserves activity and reflects the original vertical extent of the wafer and the horizontal distribution of particles within the wafer. It fails, however, to retain any information about the extent in size of the contributing particle size

class. Since this algorithm essentially treats the originally continuous particle size-frequency distribution as a series of Dirac delta functions, wafers for different size classes settle at different rates. The farther such wafers travel in the prevailing winds before impact on the ground, the greater will be the separation between their landing locations. Voids eventually develop downwind of ground-zero where wafers representing adjacent size classes fail to overlap.

The wafer smearing algorithm developed here seeks to eliminate the downwind voids and thus to produce a smoother fallout pattern than is possible with the standard (ASA) version of DELFIC. The new wafer smearing algorithm is a conceptually simple extension of the existing DELFIC approach, although the required coding modifications are extensive. The resulting code will be referred to here as the AFIT version of DELFIC.

The ASA version of DELFIC traces the motion of size class extrema, a cell boundary approach, only until the end of the cloud rise simulation. After that, it adopts a cell centered approach, tracing the motion of wafers on the basis of size class means. The vertical extent of each wafer remains fixed until the base impacts on the ground. In contrast, the AFIT model consistently employs a cell boundary transport algorithm, following the trajectories of size class extrema from cloud stabilization until eventual ground impact. Wafer tops are defined throughout transport by the motion of the smallest particles in the size class. Wafer bases are defined by the motion of the largest particles in the size class. The vertical extent of the falling wafer increases until the base impacts on the ground, because

the top and base fall at different rates. Thus, the horizontal extent of the grounded wafer is defined by computing the landing coordinates of the largest particles in the size class which originated at the base of a wafer and those of the smallest particles in the size class which originated at the top of the wafer. The crucial difference from the ASA approach is that wafer tops and bases are defined <u>throughout</u> transport by the predicted motion of the particle size extrema that define the bounds of each size class. Once a wafer has landed, the ground distribution of its contents is computed exactly as in the ASA version of DELFIC, by a geometric formalism involving grounded wafer base and top parameters (1:37).

While it might at first appear that there would be a substantial penalty in this method in terms of additional computer time and memory required to compute and store additional wafer descriptors, such is not the case. Since DELFIC is an overlayed program, its memory requirements are determined by the size of the largest overlay. In <u>both</u> the AFIT and ASA versions of DELFIC, the largest overlay is the output map processing module. Thus, the AFIT version requires no more memory to execute than does the ASA version. Moreover, by taking advantage of a computational short-cut which is impossible with the ASA version, the AFIT version of DELFIC is able to compensate for the computer time required to track its additional wafer descriptors. In transporting cloud wafer tops and bases, the ASA version is reportedly able to take advantage of the vertical adjacency of cloud wafers for each particle size class, in order to eliminate n-1 out of what would otherwise be 2n transport calculations (1:31). The code to accomplish

this simply does not, and indeed, cannot exist in the ASA version of DELFIC. Because the ASA version models each particle cloud wafer as a right circular cylinder of monosized particles, the dual identities of wafer tops and bases within a single size class are destroyed by wind shear and stem wafer subdivision before transport to the ground is begun. The AFIT version of DELFIC, on the other hand, is able to take full computational advantage of the dual identity that exists for most tops and bases of wafers belonging to adjacent particle size classes. Except at the top and base of the cloud and at the small and large particle extremes of the size distribution, and except for wafers located in the cloud stem, each wafer top and base has a dual identity. The description of the top of one wafer is identical to that of the base of the wafer above it in the cloud and belonging to the next smaller size class. Since the dual identity of all such top and base pairs is preserved by the AFIT version's cell boundary transport algorithm, computing time is saved by performing only one calculation for each unique wafer base and top. Preservation of this dual identity that exists for many of the cloud wafer tops and bases during both the drift that takes place during cloud rise and throughout subsequent transport to the ground guarantees continuity of grounded cloud wafers. Voids are eliminated.

Figure II-1 presents a comparison of dose rate contours from fallout produced for a hypothetical 2.35 KT surface burst by both ASA and AFIT versions of DELFIC. Both calculations used identical input parameters. The stabilized cloud was parceled into 2000 wafers consisting of 100 particle size classes and 20 vertical cloud layers, a

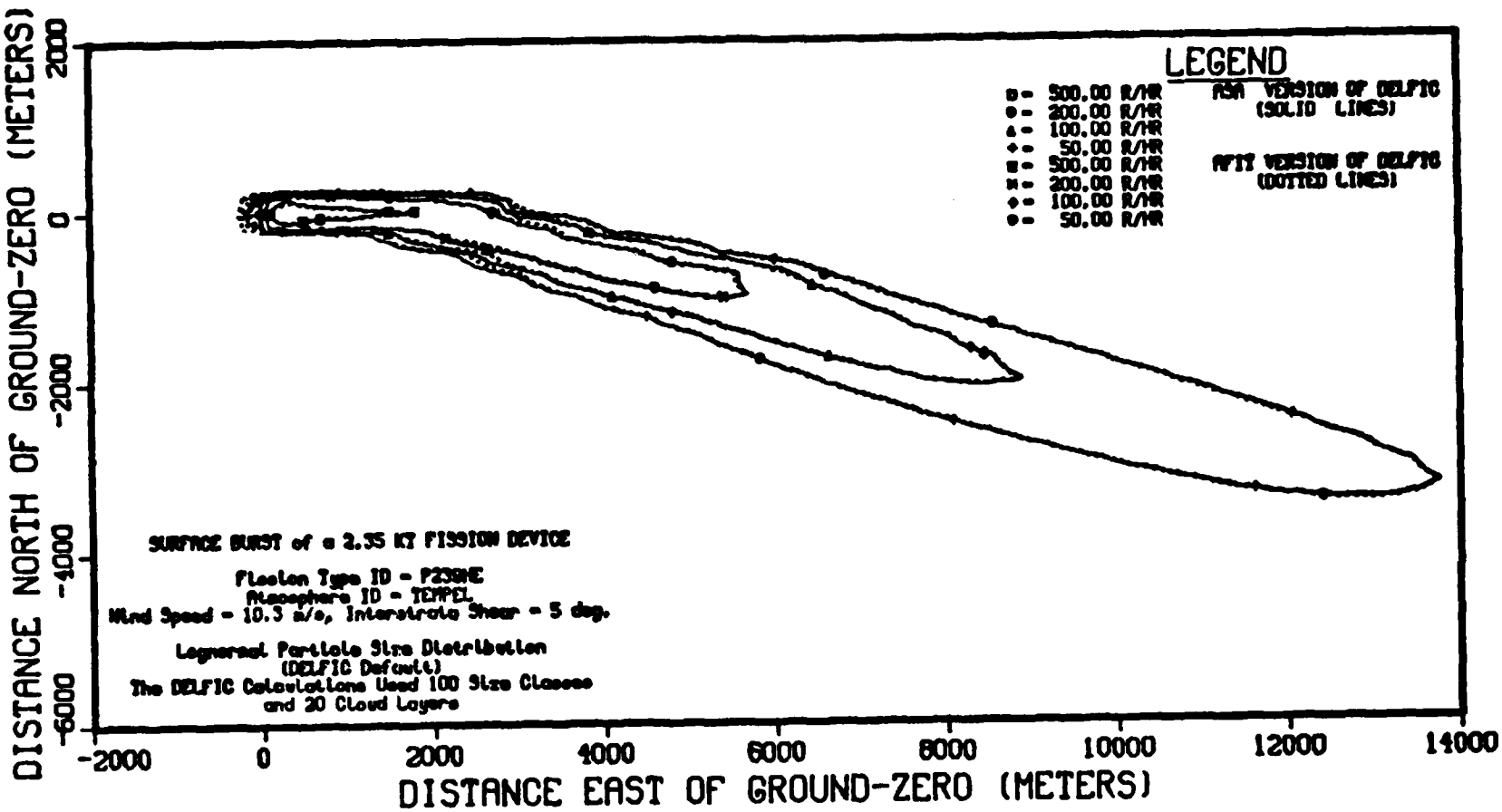

Figure II-1 Fallout Patterns for ASA and AFIT Versions of DELFIC

quadrature normally considered sufficient for a calculation for this yield with the ASA version of DELFIC. The contours overlay almost perfectly, except in the immediate vicinity of ground-zero, where stem fallout is significant. Since the radii of stem wafers depend on the size of the cloud cap at the time of wafer separation, there are generally great differences between stem wafer base and top parameters. The AFIT version of DELFIC accounts for these differences automatically. In the ASA version, it becomes necessary to subdivide stem wafers in the vertical in order to retain resolution of stem diameter (1:29).

In Figure II-2, the ASA calculation was the same as in the previous contour map. The AFIT calculation, however, used only 10 particle size classes. The patterns are still qualitatively the same; but the lower level AFIT contours are shorter than their ASA counterparts, and the 500 R/hr contour is shifted east of ground-zero. This not only demonstrates that 10 particle size classes is too small a number for modeling competency, but also suggests the sort of behavior to be expected at large downwind distances from higher yield shots. Where there are relatively few overlapping grounded wafers, the contour patterns begin to reflect more the assumed horizontal distribution of activity in the cloud and the formalism used to distribute that activity on the ground, than they do the actual process of fallout transport and deposition.

Figure II-3 vividly illustrates the modeling problem posed by non-overlap of grounded wafers. Here, both the ASA and AFIT versions used only 10 particle size classes. Although contours for the AFIT

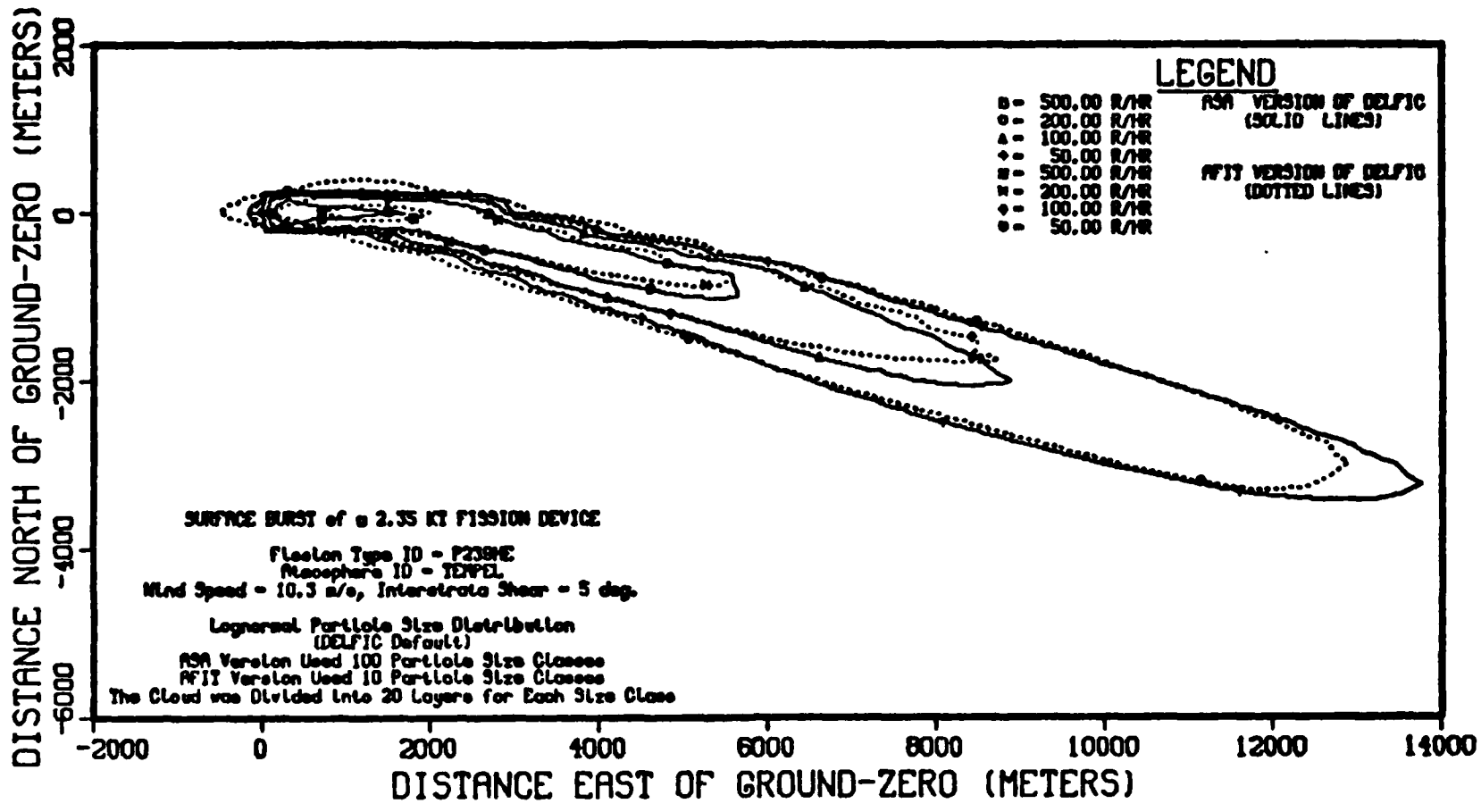

Figure II-2 Fallout Patterns for ASA and AFIT Versions of DELFIC

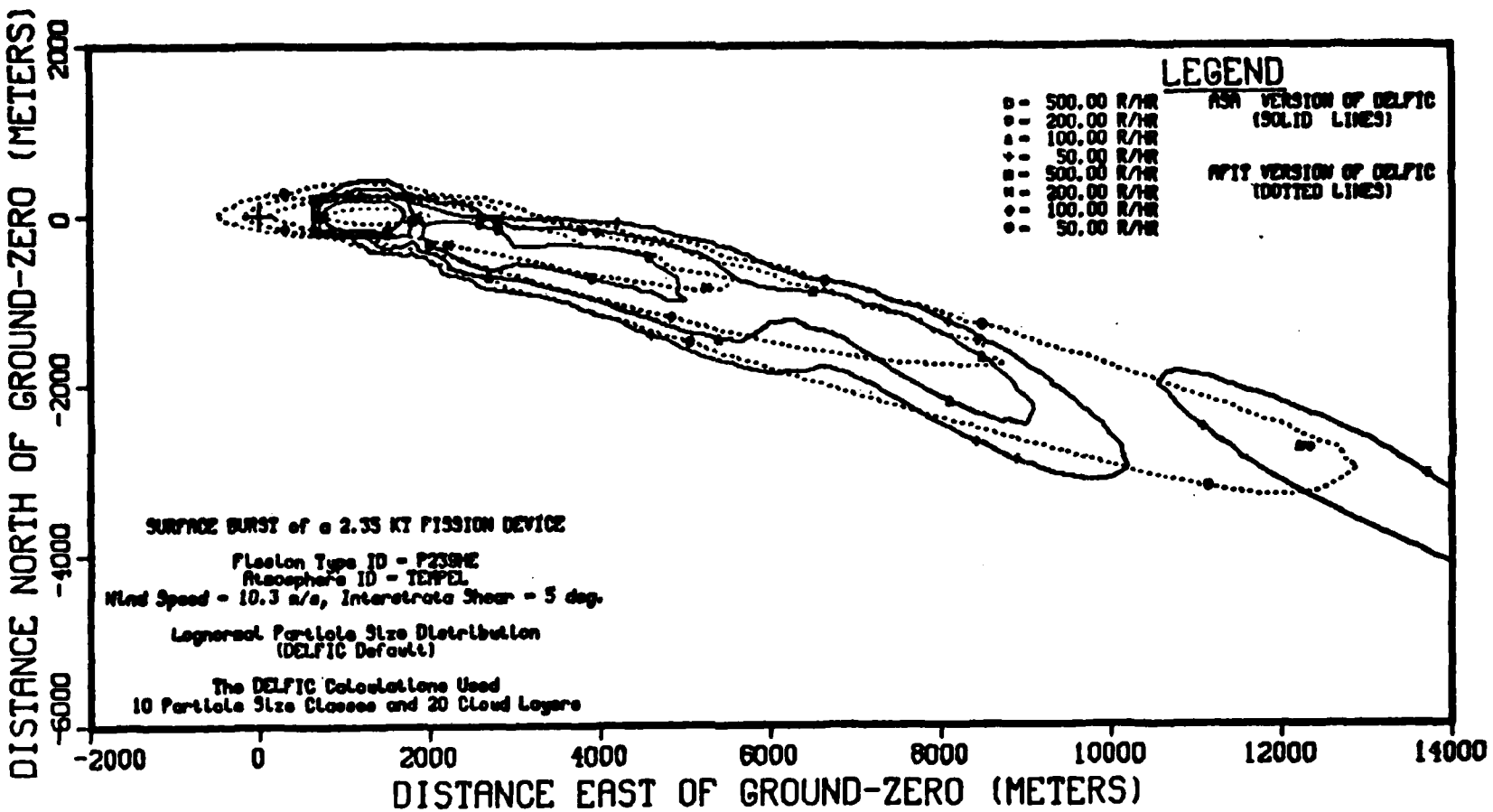

Figure II-3 Fallout Patterns for ASA and AFIT Versions of DELFIC

version of DELFIC are distorted by this paucity of wafers, this example shows that the ASA version has lost all relationship to reality. The structure in the ASA pattern is a modeling artifact produced by discrete lumps of activity deposited downwind of the burst point. The disjoint segment of the 50 R/hr contour even has the precise elliptical shape dictated by the wafer deposition algorithm. These calculations, and other examples not presented here, indicate that the AFIT version of DELFIC agrees with the ASA version when both are used with sufficiently fine quadrature. Yet, the AFIT version contours do not break up, as the ASA contours do, when the quadrature is coarse.

Figures A-1 through A-24 (Appendix A) present fallout contour pattern predictions of the AFIT version of DELFIC for a variety of particle size-frequency distributions for yields from 1 to 1000 KT. See Table II-1 for details of the distribution parameters. Figure II-4 shows DELFIC's activity assignments for the indicated size-frequency distribution parameters. All DELFIC activity calculations assumed fission of ^{239}Pu by 14 MeV neutrons. Table II-2 presents the wind profile used. The fallout patterns are identified by a code label associated with the chosen wind profile, yield, and size distribution. The wind information indicates date and location; "03W" means October 3, 1968, at Washington, DC. Yields are indicated in kilotons, with a trailing "S" for surface burst. The DELFIC default size distribution is "DEF"; the WSEG-10, SIDAC, or RAND is "WSEG"; the others are identified on the basis of the particle size-frequency median, for example, "22P7" for 22.7 μm. Thus, the identifier, "03W1000S22P7", refers to a 1000 KT surface burst calculated using winds observed on

Table II-1 Particle Size Distributions

Distribution Identifier	Size Median	Surface Median	Volume Median	Geometric Deviation	Description
DEF	0.407 μm	19 μm	130 μm	4.0	DELFIC default
LYSTND	0.314	15	100	4.0	Low yield standard
HYSTND	22.7	74	135	2.16	High yield standard
WSEG	24.0	63	101	2.0	SIDAC, WSEG-10, or RAND
NRDLC61	0.0849	24	412	5.376	NRDL C-61, coral sand
NRDLN61	0.00556	14	709	7.24	NRDL N-61, Nevada Test Site

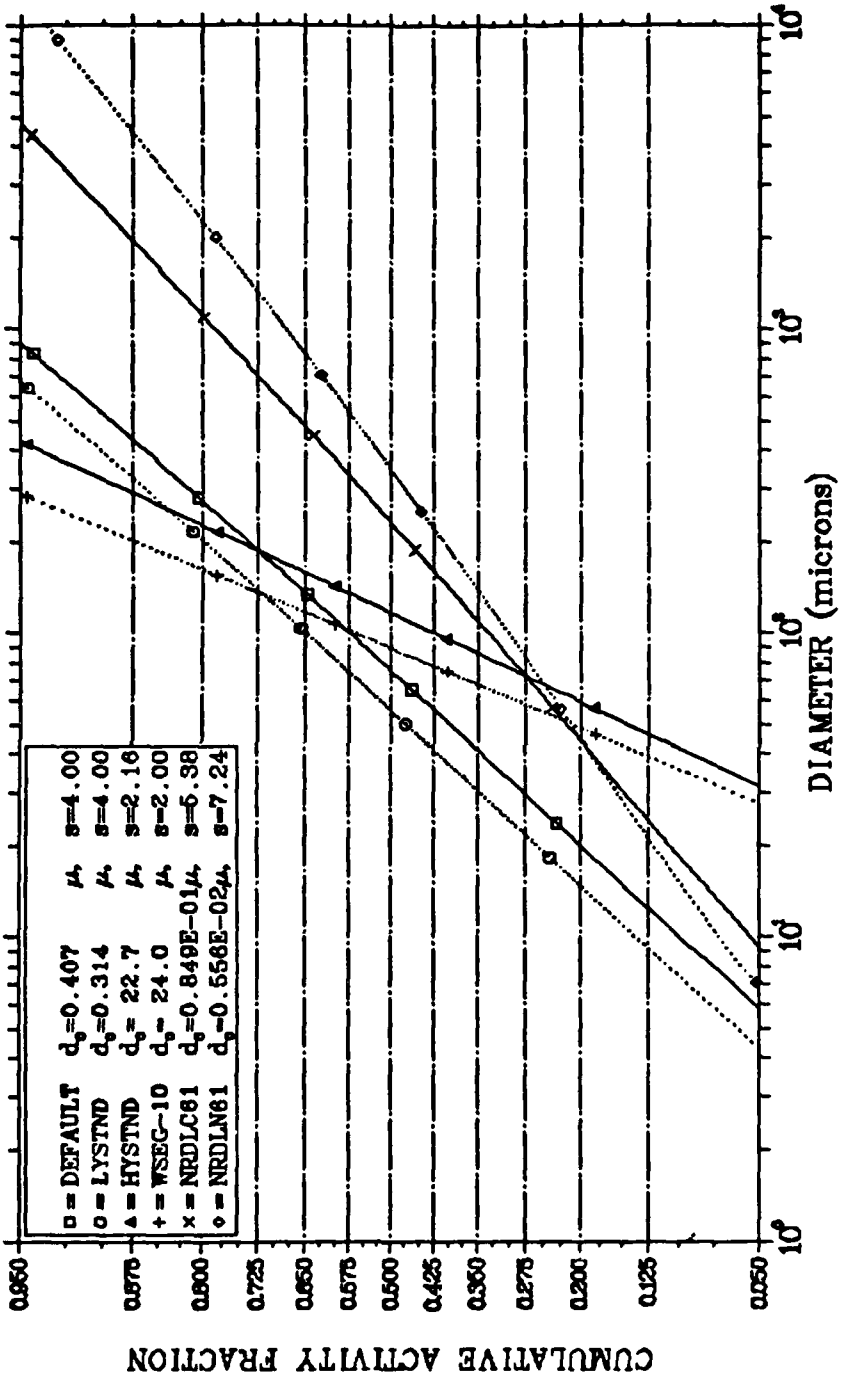

Figure II-4 Size-Activity Distributions for DELFIC

Table II-2 Wash, DC Winds for 3 Oct 1968

Altitude (m)	Direction (deg)	Speed (m/s)
132.	174.	3.
540.	206.	10.
1049.	229.	10.
1536.	235.	11.
2045.	233.	11.
2570.	240.	9.
3142.	258.	11.
3720.	265.	14.
4376.	265.	12.
5030.	255.	10.
5790.	255.	12.
6580.	259.	12.
7456.	275.	15.
8411.	275.	18.
9482.	296.	15.
10698.	291.	24.
12113.	285.	23.
12954.	281.	21.
13920.	272.	17.
15059.	268.	16.
16440.	265.	14.
17822.	266.	9.
18655.	249.	9.
19623.	250.	9.
20776.	234.	9.
22198.	250.	7.
24039.	180.	3.
25226.	258.	3.
26684.	271.	6.

October 3, 1968, at Washington, DC, employing the size distribution having a median of 22.7 μm ("High yield standard"). Four of the size distributions were chosen as representative of a variety of plausible distributions in a previous study by Norment (21:25). Although Norment's "High yield standard" was intended to represent the RAND (or WSEG-10) size-activity distribution (lognormal with a median of 89.4 μm and geometric standard deviation of 2.0) through the assumption that the RAND data represented the 2.5 moment of an underlying lognormal size-frequency distribution, the distribution identified as "WSEG" in Table II-1 was developed here to yield a DELFIC activity assignment that more closely mimics the RAND result. Norment's "Low yield standard" was chosen to represent the 2.5 moment of a lognormal fit to the extensive particle size-activity data available from the Small Boy test shot. The other two distributions were similarly defined relative to lognormal size-activity distributions in use at the time by the Naval Radiological Defense Laboratory. Relative to the DELFIC default and "standard" distributions, they represent rather extreme distributions, with large size-activity medians, and an enormous range of particle sizes.

While many of the predictions appear quite reasonable, it is apparent that modeling artifacts are being introduced for some size distributions, especially at low yields. Similar artifacts would be expected for lower level contours (not shown), larger downwind ranges, and higher yields. Although the AFIT version of DELFIC is able to better tolerate a coarse quadrature than is the ASA version, it is apparent that neither code can make competent predictions at

arbitrarily large downwind distances. The AFIT version guarantees that there will always be some overlap between wafers which were adjacent in the stabilized cloud and stem; but whenever there are only a few instead of many overlapped wafers, the resulting contour pattern will reflect more the assumptions about the horizontal distribution of activity in individual wafers than it will a realistically expected ground dose rate. The AFIT version can eliminate the voids at large downwind distances, but the artificial lumps and resultant structure in contour patterns will remain. Although the range of competence of any disc tosser is somewhat dependent on yield, wind structure, atmospheric properties, and assumed particle size distribution, that range is finite. The competence of any disc tosser fallout code depends to an extent on the overlap of many cloud wafers at any point of interest in the fallout field. At distances so large that it is impractical to provide a sufficient number of wafers, some other algorithm must be used to predict the deposition of fallout.

III. Smearing the Debris Cloud Over the Fallout Field

Abandon Disc Tossing for Smearing

DELFIC and all other disc tosser fallout codes are limited in ability to competently model far field fallout deposition by the requirement that many or, at least several, cloud wafers overlap at the point or points of interest. The ever finer particle size filing produced by minute differences in particle settling rates over long downwind transit distances forces ever finer particle size and cloud level quadrature on the disc tosser, if multiple wafer overlap is to be insured. The stronger the wind, the more severe is the overlap problem. Dose rate calculations at more than a few representative points far downwind, let alone any attempt to produce contour maps, become expensive in terms of computer time, and in the case of operational type studies requiring many thousands of calculations, impractical. Smearing of discrete, contiguous cloud wafers, as is done in the AFIT version of DELFIC, is at best a partial solution to the problem.

The prohibitively fine particle size and cloud layer mesh called for by the far field fallout problem suggests, as a limit, that one really needs to smear the entire debris cloud, with its total particle burden, in some continuous manner over the downwind field -- rather than smearing individual wafers. Although the idea for a "smearing" fallout prediction model is not new, the only such model still in

widespread use today is WSEG-10 (4). First developed more than 20 years ago, it survives in slightly modified form as the fallout generator used by the National Military Command System Support Center in the operational analysis code, SIDAC (Single Integrated Damage Analysis Capability) (5), and as the fallout module for the Texas Instruments TI-59 programmable calculator nuclear weapons effects programs published by the Defense Nuclear Agency (6).

WSEG-10 probably owes its longevity more to simplicity and calculational speed than it does to modeling accuracy. As a non-numeric model based on empirical fits to old nuclear test data, WSEG-10 is very fast and requires few inputs. Unfortunately, even in the absence of highly sheared or complex wind fields, WSEG-10 does not agree all that well with DELFIC (7). DELFIC, on the other hand, has been shown to be capable of producing good agreement with most of the nuclear test shots for which sufficient data exists to provide the required model inputs. Over the years, WSEG-10 has received a well-deserved share of criticism by Russell (8:209), Polan (9:31), Norment (3:103), and others, as summarized by Bridgman and Bigelow (10). What follows is not a repair of the WSEG-10 model; rather, it is a derivation of a new fallout model based on first principles: a model capable of answering the major criticisms of WSEG-10, and which agrees with DELFIC to the extent permitted by modeling assumptions.

Smearing Model Details

The ground distribution of fallout activity per unit area at time

t, A(x,y,t), can be expressed as that part of the cloud activity distribution which is deposited at (x,y) from time t=0 to time t. If $A_t(t)$ is the total activity in the cloud at time t, then

$$A(x,y,t) = A_t(t) \int_0^t f(x,y,t')g(t')dt' \quad (1)$$

where $f(x,y,t')$ is the normalized horizontal spatial distribution of activity in the cloud, and $g(t')$ is the fractional arrival rate of activity on the ground. Equation (1) has been called the smearing equation. It is the heart of any fallout smearing calculation. If the fractional arrival rate, $g(t')$, of all cloud activity over all ground area can be found, and if the horizontal spatial distribution of arriving cloud activity per unit area, $f(x,y,t')$, is known, then the activity, A(x,y,t), "smeared" on the ground at location (x,y), through time, t, is the integral of the product of these two functions. By way of contrast, a conventional disc tosser calculation never explicitly uses g(t), but rather performs a double numerical integration over those particle sizes and initial particle locations which can contribute to A(x,y,t). The g(t) function is the key to any smearing calculation. The WSEG-10 model proposes it is an exponential function as a result of an empirical fit of some early RAND calculations. Here it will be developed directly from physical principles.

Equation (1), the smearing equation, usually is not solved for A(x,y,t); rather, following a series of changes in dependent variable, one solves for an artificial quantity, the "unit time reference dose rate", which is the exposure rate in Roentgens per hour or dose rate in rads per hour experienced at a detector 3 ft above an infinite plane

field of uniformly distributed debris, one hour after detonation (11:391):*

$$\dot{D}_1(x,y) = kYF_f \int_0^{\infty} f(x,y,t')g(t')dt' \qquad (2)$$

where k is known as the "source normalization constant", with units of (exposure/time) per (fission yield/area), Y is the total device yield, and F_f is the fraction of that yield which is due to fission, as opposed to fusion. For Y expressed in kilotons and distances expressed in statute miles, consistent units for k are $(R/hr)/(KT/mi^2)$.

Experimental determination of k on the basis of observed fallout patterns is difficult. The choice of a best value depends not only on physical considerations, but also on modeling assumptions. For the smearing model to be derived below, however, the choice is clear. Since the aim is to reproduce DELFIC results as closely as possible, k is obtained directly from DELFIC. Although k is a weak function of fission fuel (^{235}U, ^{239}Pu, etc.) and of the neutron energy spectrum, a mid-range value of 2350 $(R/hr)/(KT/mi^2)$, corresponding to fission of ^{239}Pu by 14 MeV neutrons, may be inferred by summing the activity contributions from all DELFIC particle size classes.

Consider now the horizontal distribution of activity in the cloud, f(x,y,t), the first function in the integrand of equations (1) and (2).

---

* The upper limit is taken as infinity, not one hour, by convention. Thus, the reference dose rate should be interpreted as the dose rate at one hour, which would be measured if all the activity which would ever be deposited at (x,y) were deposited there by one hour.

Cloud geometry has seen various forms in fallout modeling. DELFIC arrives at a distribution by dynamic modeling of the rise and stabilization of the buoyant, entraining fireball. Most models assume some geometric shape for the cloud and determine dimensions on the basis of empirical relations derived from test shot data. One or two right-circular cylinders were early popular choices. WSEG-10 uses gaussian functions for both horizontal and vertical distributions. The WSEG-10 choices are reasonable in that they are in agreement with what little data is available and can be rationalized on the basis of the inherently stochastic nature of atmospheric transport. For this model, the WSEG-10 functions are adopted to describe cloud geometry (4:49; 12). The horizontal distribution is given by

$$f(x,y,t) = (2\pi)^{-\frac{1}{2}}(\sigma_x\sigma_y)^{-1} \exp\{-\tfrac{1}{2}[((x-Vt)/\sigma_x)^2+(y/\sigma_y)^2]\} \qquad (3)$$

where V is an assumed constant effective wind. The initial vertical distribution is similarly taken as

$$h(z) = (2\pi)^{-\frac{1}{2}}\,\sigma_h^{-1} \exp\{-\tfrac{1}{2}((z-H_c)/\sigma_h)^2\} \qquad (4)$$

The downwind standard deviation, σ_x, is taken to be a yield dependent constant equal to the effective radius of the cloud, σ_o

$$\sigma_o = \exp\{.7 + (\ell nY)/3 - 3.25/[4+(\ell nY+5.4)^2]\} \qquad (5)$$

for Y in megatons and σ_o in statute miles. The crosswind variance is the sum of the downwind variance and two terms which account for diffusive dispersion and shear dispersion:

$$\sigma_y^2 = \sigma_o^2(1+8t/T) + (S_y\sigma_h t)^2 \qquad (6)$$

S_y is the crosswind component of the wind shear. H_c and σ_h (kft), the mode and standard deviation of the initial vertical distribution (equation (4)), and T (hr), are yield dependent parameters given by

$$H_c = 44. + 6.1\ell nY - .205(\ell nY + 2.42)|\ell nY + 2.42| \qquad (7)$$

$$\sigma_h = .18H_c \qquad (8)$$

and

$$T = \left(12H_c/60 - 2.5(H_c/60)^2\right)\left(1 - .5\exp\{-(H_c/25)^2\}\right) \qquad (9)$$

Although he argues with the values of H_c, σ_o, and σ_h calculated by these equations, Norment (3:80), in his comparison of fallout models, concluded that the WSEG-10 treatment of diffusive and shear dispersion was adequate. At any rate, as the simple model being derived here will not be capable of dealing with complex wind patterns as is DELFIC; the current effort will focus on model validation by comparison of fallout ground arrival rates with DELFIC results. In this phase of prediction, this model seeks to be about as good as DELFIC.

As stated, g(t), the second function in the integrand of equation (1) or (2), is the keystone of any smearing model. It is also the source of some of the criticisms of the WSEG-10 model mentioned previously. The WSEG-10 choice for g(t) is a negative exponential in time whose parameters were based on some early RAND data (4:4)

$$g(t) = K\exp\{(-t/T)^{n_o}\} \qquad (10)$$

where T and n_o are yield-dependent empirical constants and K is determined by the normalization requirement that the integral of g(t), taken over all time, be unity. With this form for g(t), the gaussian form for the horizontal distribution of activity in the cloud, and the assumption of a constant effective wind, one conveniently obtains an integrable expression for the fallout "footprint". Unfortunately, the formulation also predicts sizable activity down within moments of zero time. Norment has suggested that the WSEG-10 formulation for g(t) be thoroughly re-evaluated, with particular regard to the parameters n_o and T (3:78). Here g(t) is completely re-derived without recourse to a priori assumptions of functional form, activity distributions, or fall dynamics.

Derivation of g(t) and the AFIT Model

It is conventional in fallout calculations to model the debris particles as rigid spheres falling at terminal velocity in a viscous medium, air. Although the acceleration of gravity is nearly constant over altitudes of interest, the viscosity of the air varies with altitude as the atmospheric density changes. As a result, the particle fall velocity is altitude dependent. Since all the particles may reasonably be assumed to have the same density, the only other variable on which fall rate depends is particle size. Clearly, the altitude and particle size dependencies of the fall velocity are separable. Therefore, the fall velocity, V_z, can be replaced by the derivative, -dz/dt; and the result can be integrated over the trajectory of a

single particle to obtain an expression for the time required for that particle to impact with the ground:

$$V_z = -dz/dt = R(r)Z(z) \tag{11}$$

$$t_a = \frac{1}{R(r)} \int_0^{z_o} \frac{dz}{Z(z)} \tag{12}$$

Thus, the time of arrival, t_a, is uniquely determined by the size dependence of the fall dynamics and by the initial particle altitude. Said another way, for each initial altitude, z_o, the fraction of activity which arrives on the ground within the interval dt about t must equal the fraction of activity at that altitude which is associated with particles whose radii are in a range dr about r, where r and t are related by equation (12). That is, the distribution of activity with particle size is transformed by the fall dynamics prescription into a distribution of activity with time of arrival:

$$|g(t)dt| = |A(r)dr| \tag{13}$$

or, rearranging,

$$g(t) = A(r)|dr/dt| \tag{14}$$

Thus, if A(r), the distribution of activity with particle size is known or assumed, g(t) can be found, provided only that $|dr/dt|$ can be calculated. Equation (12) provides the means to do this. As it stands, this equation is in the form used by conventional disc tosser codes to calculate the grounding times of monosized particle wafers. For use in a smearing code, the result is inverted to produce an

expression for the size of particles landing as a function of their arrival time. Symbolically

$$r = F(t;z_o) \tag{15}$$

Differentiation of equation (15) yields dr/dt. For a vertically distributed debris cloud, equation (14) becomes:

$$g(t) = -\int_{z_B}^{z_T} f(z)\ A(r)\ (dr/dt)\ dz \tag{16}$$

With this result, the activity arrival rate depends explicitly on both the activity distribution and the particle fall dynamics expression, functions which, in the WSEG-10 model, are buried in empirical fits to RAND fallout data.

Evaluation of equation (15) and its derivative requires selection of a mathematical description of particle fall dynamics. The quantity of primary interest in determining the selection is the Reynolds number, R, which is the ratio of the inertial force to the viscous force experienced by a particle moving through a fluid (air):

$$R = 2V_z\rho_a r/\eta \tag{17}$$

where η is the altitude dependent dynamic viscosity of air (kg/m-sec), V_z is the particle fall velocity (m/sec), r is the particle radius (m), and ρ_a is the air density (kg/m^3). When the Reynolds number is small (say, $R < 0.05$), viscous forces dominate, and the drag force on the particle is given by Stokes' law:

$$D = 6\pi\eta r V_z \tag{18}$$

or, in terms of the Reynolds number, from equation (18)

$$D = 3\pi\eta^2 R/\rho_a \tag{19}$$

For a particle falling at terminal velocity (steady state), the drag force is balanced by the gravitational force, so that, for particles of density ρ_f (taken here to be 2600 kg/m^3)

$$6\pi\eta r V_z = (4/3)\pi r^3 g\rho_f \tag{20}$$

where g is the gravitational acceleration (9.8 m/sec^2), and buoyancy is neglected, since $\rho_f >> \rho_a$. An approximate cut-off particle size for which Stokes' law is valid is determined by using equation (19) to express equation (20) in terms of the Reynolds number, and solving for the particle size:

$$r = \left(\frac{9\eta^2 R}{4g\rho_f\rho_a}\right)^{1/3} \tag{21}$$

The cut-off size is about 10 μm with an admittedly pessimistic 0.05 for the Reynolds number, and typical sea level atmospheric properties. As particles ten to a thousand times larger contribute significantly to local fallout, it becomes necessary to consider the regime of larger Reynolds numbers, where dynamic pressure becomes dominant in determining the drag force. For spheres the Stokes expression becomes

$$D = (1/2)\rho_a V_z^2 C_d \pi r^2 \tag{22}$$

where $(1/2)\rho_a V_z^2 C_d$ is the dynamic pressure exerted on the projection of the particle area in the direction of motion and C_d is the drag coefficient. In terms of R

$$D = \pi\eta^2 C_d R^2/(8\rho_a) \tag{23}$$

The large Reynolds number analog of equation (20) becomes

$$(1/2)\rho_a V_z^2 C_d \pi r^2 = (4/3)\pi r^3 g\rho_f \tag{24}$$

or, using equation (23) in lieu of (22), and solving for the dimensionless $R^2 C_d$

$$R^2 C_d = 32 g\rho_a \rho_f r^3/(3\eta^2) \tag{25}$$

DELFIC calculates V_z on the basis of equations (17) and (25) by a method due to McDonald (13) and Davies (14). $R^2 C_d$ is calculated from equation (25). The Reynolds number is then obtained from a polynomial expansion in $R^2 C_d$ suggested by Davies. Finally, the fall rate is obtained from equation (17). In the interest of preserving maximum equivalence between the AFIT smearing model and DELFIC, the same approach is taken here. The difficulty with this method is that it does not permit an analytic solution to equation (15). Thus, in order to better illuminate the process, and to indicate the small particle limit which the more exact solution must approach, it is instructive to consider first the solution for particles which obey Stokes' law, equation (20).

When V_z is replaced by -dz/dt in equation (20) and the result is integrated over the trajectory of a single particle, the following

expression relating r and t is obtained:

$$r^2 = \frac{9 \int_0^z \eta(z')dz'}{2g\rho_f t} \tag{26}$$

Differentiation with respect to time at constant altitude yields immediately

$$dr/dt = -r/(2t) \tag{27}$$

which can be expressed in terms of t alone by means of equation (26). Of course, equation (26) can also be used to express the activity distribution, A(r), as a function of t in lieu of r. Both of these "t for r" substitutions will be made later in calculating g(t) with use of the McDonald-Davies method.

Outside of the small particle Stokes' law regime, equation (24) cannot simply be integrated, as was equation (20), to obtain a high Reynolds number analog of equations (26) and (27). This is because the drag coefficient is itself a velocity dependent variable. The method of McDonald and Davies, however, provides a means to calculate fall velocities indirectly through the Reynolds number, R. The quantity R^2C_d is obtained from equation (25) and used to obtain R by use of Davies' polynomials:

$$\begin{aligned} R &= R^2C_d/24 - 2.3363\times10^{-4}(R^2C_d)^2 + 2.0154\times10^{-6}(R^2C_d)^3 \\ &\quad - 6.9105\times10^{-9}(R^2C_d)^4 \qquad \text{for } R < 4 \text{ and } R^2C_d < 140 \\ \log R &= -1.29536 + 0.9861\log(R^2C_d) - 0.046677(\log(R^2C_d))^2 \\ &\quad + 0.0011235(\log(R^2C_d))^3 \qquad \text{for } 3 < R < 10^4 \end{aligned} \tag{28}$$

Note that in the small R^2C_d limit, this formulation approaches $R = 24/C_d$, which reduces the Newtonian drag expression, equation (23), to Stokes' law, equation (19). The Reynolds number thus obtained is used in equation (17) to obtain the particle fall rate. McDonald originally suggested this algorithm with reference to a graphical representation of R^2C_d, and observed that the formulation for R^2C_d given by equation (25) could be readily exploited to calculate altitude dependent fall velocities, since in it, R^2C_d depends only on material properties of the particle and of the atmosphere. DELFIC's authors adopted the Davies' polynomials in lieu of the graphs. The fall rates, V_z, thus calculated are corrected for high altitude drag slip by multiplying them by the same factor as is used in DELFIC (15:6):

$$C_f = 1 + 1.165 \times 10^{-7}/(\rho_a r) \tag{29}$$

for r and ρ_a in MKS units. The fall velocities calculated in this way for each particle size can be used to numerically integrate equation (24) over the particle trajectory, leading to a numeric expression of equation (15), which is analogous to the Stokes' law expression, equation (26).

Since there is no reason to repeat the above procedure for each fallout prediction, data satisfying equation (15), and which span the parameter space, are generated once. The resulting $r = F(t;z_o)$ curves are then fit to a Laurent series in time. Since the Stokes results above show that in the small particle size limit (long fall time), r is proportional to $t^{-1/2}$ and dr/dt is proportional to $t^{-3/2}$,

correct behavior in this limit is guaranteed by using

$$r = \sum_{i=1}^{6} C_i(z)t^{i-6} + C_7(z)t^{-\frac{1}{2}} \qquad (30)$$

The derivative, dr/dt, is found trivially by a term-by-term differentiation of the series. The complete table of coefficients, spanning the 0 to 50 km altitude range in intervals of 200 m is presented in Table B-1 (Appendix B). An identical set of coefficients was previously reported by Colarco (16:67).

The calculation of A(r)dr/dt in the integrand of equation (16) proceeds as follows for each altitude required:

1. Interpolate in the table of coefficients for the Laurent series expansion of $r = F(t;z_o)$ to obtain coefficients for the current altitude, z_o.

2. Evaluate the series expansions for r and dr/dt at time t.

3. Use the calculated value of r to evaluate A(r).

The limits of integration for equation (16) are established as $\pm 3\sigma_h$ about the cloud center height, H_c, as given by equation (7). The vertical distribution of activity is a gaussian, with standard deviation, $\sigma_h = 0.18H_c$ (equation (8)).

Figure III-1, which presents g(t) for a 1000 KT yield, compares the forms of g(t) predicted by WSEG's negative exponential, a RAND model calculation reported in RM-2460 (17), the AFIT smearing model developed above (all three using the same RAND lognormal size-activity distribution). In addition, a DELFIC calculation is presented, which uses an approximation to the RAND activity distribution (introduced in

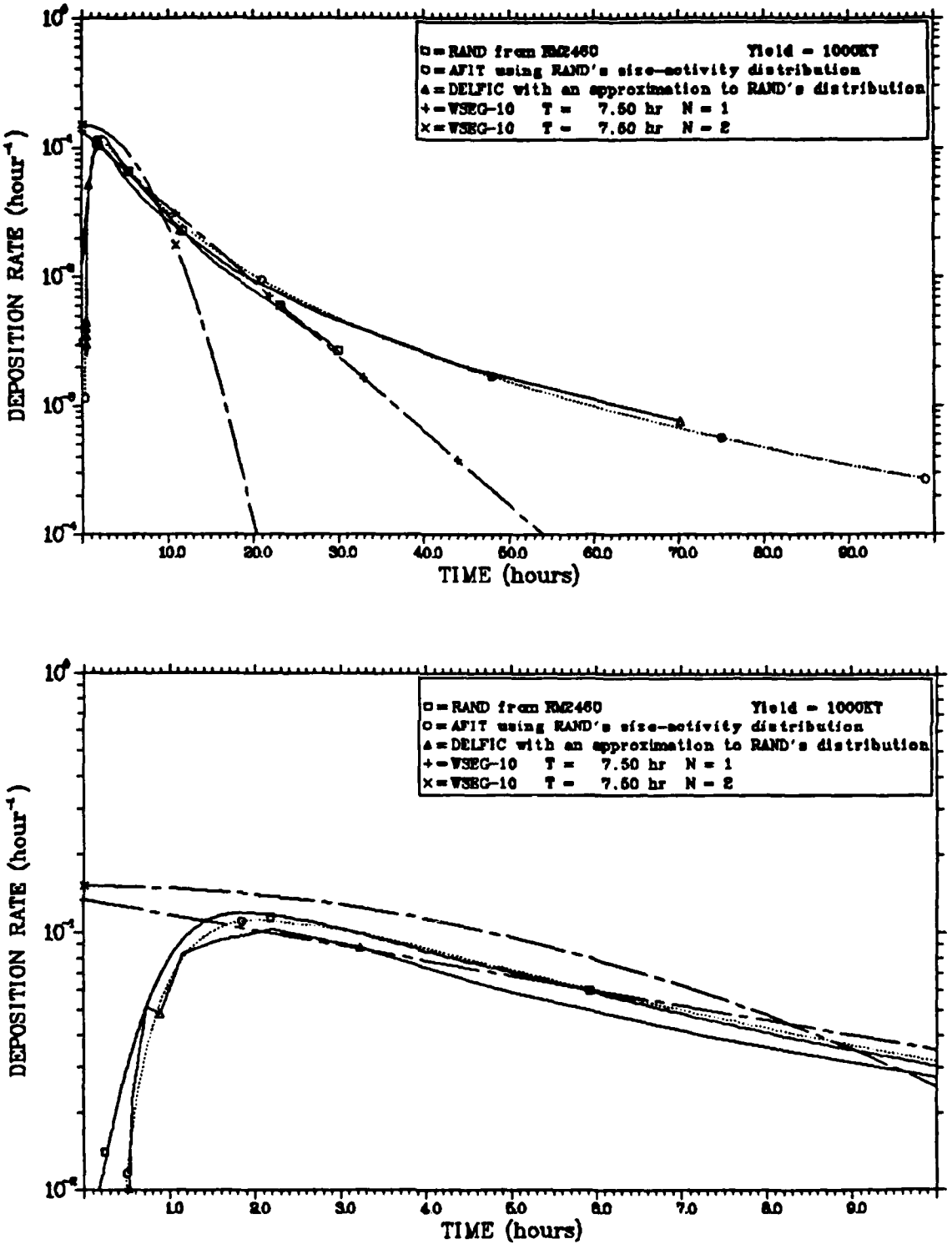

Figure III-1 Deposition Rates for RAND's Activity Distribution

the previous chapter). The WSEG and AFIT models used the same cloud model; RAND's cloud was a right circular cylinder. Although there are minor differences in magnitudes, the RAND, DELFIC, and AFIT models all predict the same general behavior for the g(t) function. The two WSEG calculations are notably different, both at early and late times. Both WSEG calculations used a decay time of 7.5 hours for the activity deposition rate, as determined by the SIDAC prescription (5:14). The n_o values of 1 and 2 bracket the range of possible values for all yields. WSEG's choice of a functional form for its g(t) fit leads to the prediction of sizable activity down within moments of zero time. This early over-prediction is compensated for by a too rapid decay in the activity grounding rate at later times. Since the size-activity distributions and cloud geometries were the same for both WSEG and AFIT models, the AFIT model apparently offers an improvement over WSEG in modeling fallout arrival rate.

Although most fallout models use a lognormal function to depict the distribution of <u>activity</u> with particle size, as was done for the comparison above, there is no need for such a restriction with the AFIT model. Part of DELFIC's flexibility derives from its avoidance of such an a priori selection. Rather, on default of input to the contrary, DELFIC specifies a lognormal <u>frequency</u> distribution of particle size, in accord with Freiling's extensive observations of fallout particle sizes (18:6):

$$dN(r) = \frac{dr}{\sqrt{2\pi}\, r\, \ell ns} \exp\{-\tfrac{1}{2}\left(\frac{\ell nr - \ell nr_g}{\ell ns}\right)^2\} \qquad (31)$$

where r_o is the median radius and s is the geometric standard deviation (dimensionless). This form is especially convenient because of the simple relationships which exist between the various moments of a lognormal distribution (19:12). Specifically, the n-th moment is also lognormal, with the same geometric deviation and with a median given by

$$r_n = \exp\{\ell nr_o + n(\ell ns)^2\} \tag{32}$$

Thus, surface area is lognormally distributed with $\ell nr_2 = \ell nr_o + 2(\ell ns)^2$, and volume is distributed with $\ell nr_3 = \ell nr_o + 3(\ell ns)^2$. DELFIC then models the assignment of activity to the particle distribution according to a modification of Freiling's radial power distribution law, which assumes that the nuclides of each fission product mass chain are distributed according to some non-integer moment of the size-frequency distribution, some of each chain being mixed homogeneously throughout the carrier soil particle (the "refractory" fraction), the remainder being plated out on the surface. Fractionation is the term generally used to describe this process. The aggregate size-activity distribution is just the sum over all mass chains.

In this model, DELFIC's use of a particle size-frequency distribution, is retained, but the individual mass chain detail is omitted. Even so, the following simple assumption permits inclusion of a first order accounting for fractionation which is based on DELFIC results. A fraction, f_r, of the total cloud activity is assumed to be distributed homogeneously throughout the carrier soil particles, or according to the third moment of the size frequency distribution. The

remaining fraction, $(1-f_r)$, is assumed to be plated out on the surface of the carrier soil; and, hence, it is distributed according to the second moment. The total activity distribution is then the sum of volumetric and surface components:

$$dA(r) = \frac{dr}{\sqrt{2\pi}r\ \ell ns}\left(f_r \exp\{-\tfrac{1}{2}\left(\frac{\ell nr - \ell nr_3}{\ell ns}\right)^2\}\right.$$
$$\left. + (1 - f_r) \exp\{-\tfrac{1}{2}\left(\frac{\ell nr - \ell nr_2}{\ell ns}\right)^2\}\right) \qquad (33)$$

DELFIC's assignments of activity to particle size groups provide a means to estimate f_r. Equation (34) is integrated to produce an expression for f_r in terms of the cumulative size-activity distribution, $A_c(r)$, and the cumulative surface and volumetric components, $A_{vc}(r)$, and $A_{sc}(r)$, respectively:

$$f_r = \left(A_c(r) - A_{sc}(r)\right) / \left(A_{vc}(r) - A_{sc}(r)\right) \qquad (34)$$

where corresponding values of $A_c(r)$ and r are obtained from DELFIC. Since, as noted above, DELFIC does not use a simple two-component distribution, values of f_r calculated in this way are weakly dependent on the choice of $A_c(r)$ and r. Selection of the median radius of the DELFIC size-activity distribution, the size for which $A_c(r) = 0.5$, yields a two-component distribution which closely follows DELFIC over the entire particle size range. Resulting f_r values (see Figure III-2) were found to be essentially independent of yield over a 1 KT to 1000 KT yield range, and only weakly dependent on choice of particle size-frequency distribution. Figures III-3 through III-8 display the two-component distributions derived in this manner for each of the

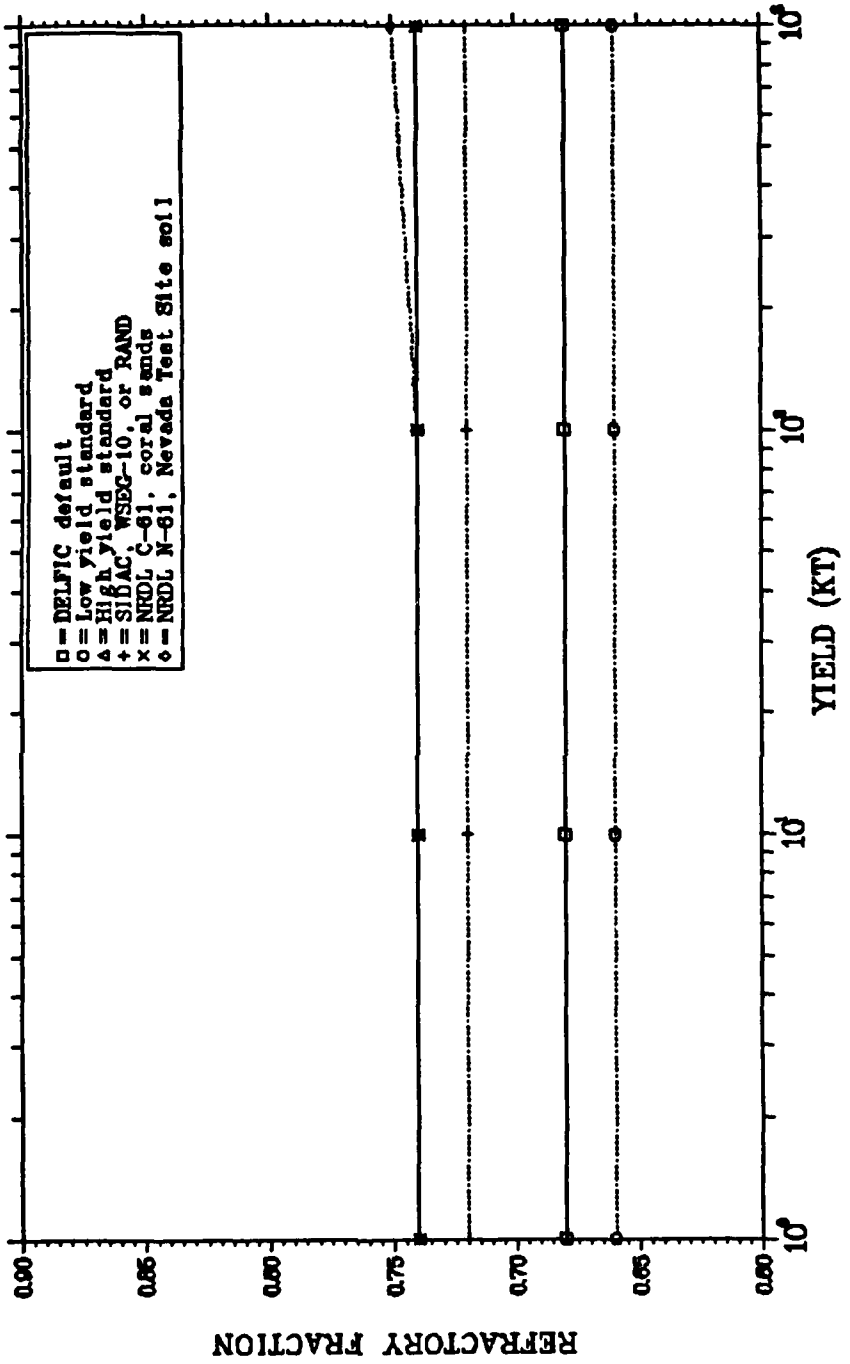

Figure III-2 Refractory Activity Fractions

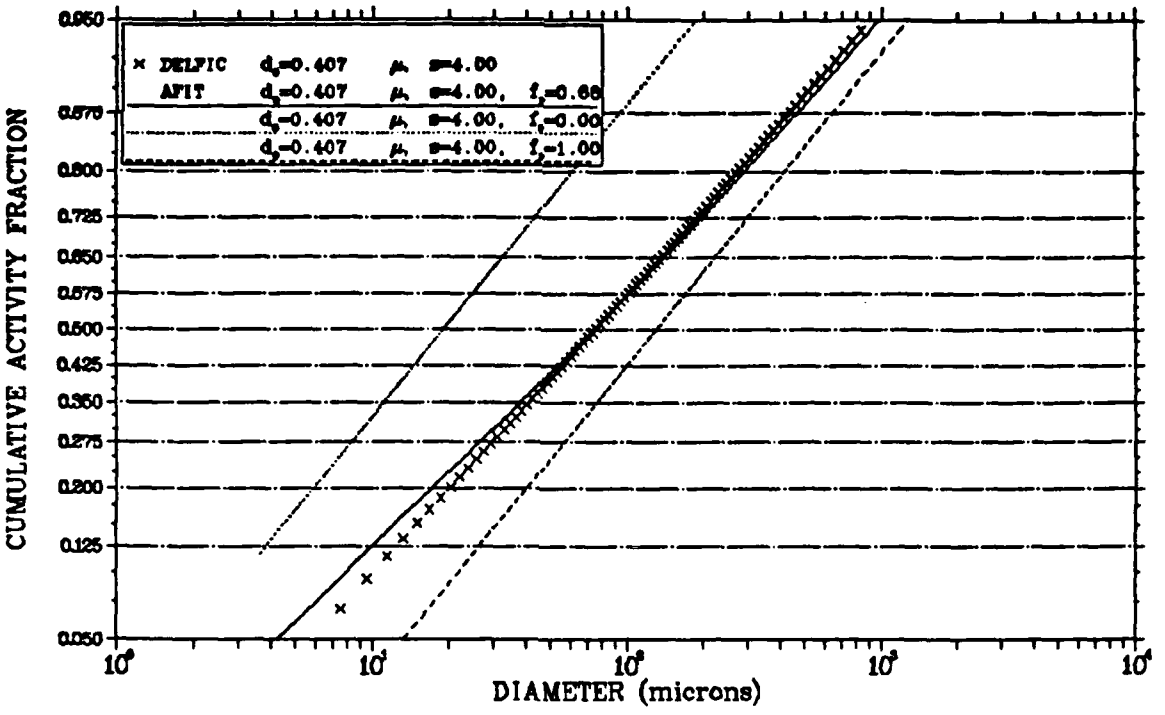

Figure III-3 DEFAULT Size-Activity Distribution

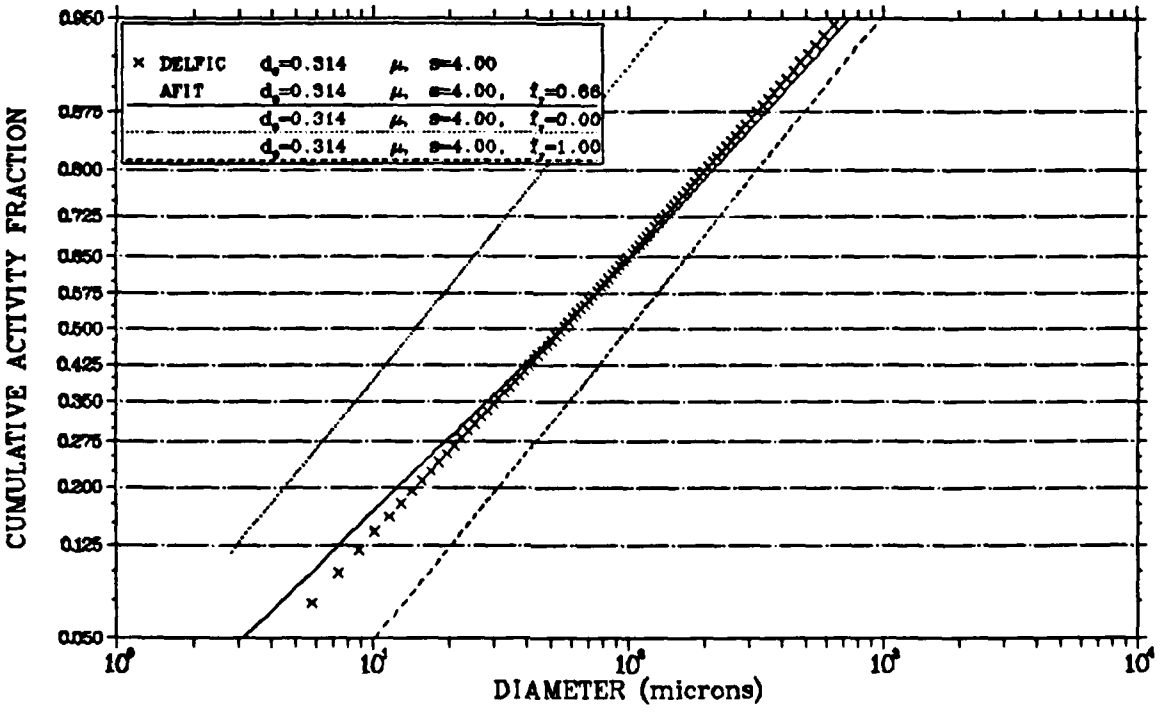

Figure III-4 LYSTND Size-Activity Distribution

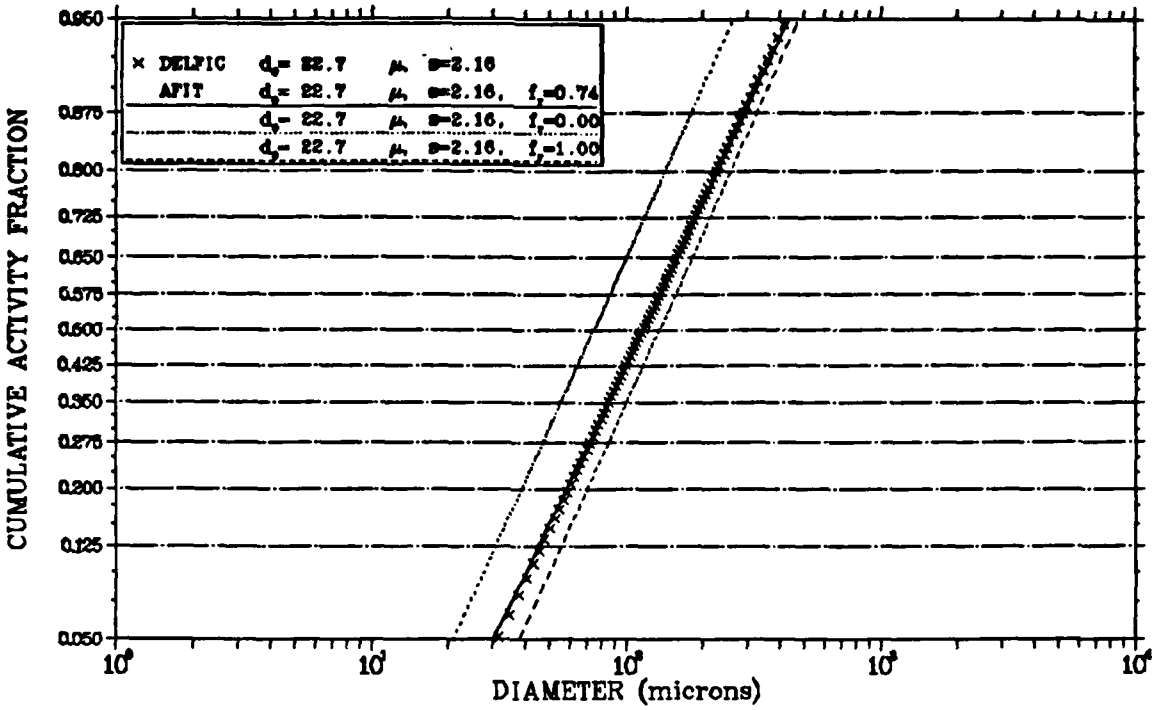

Figure III-5 HYSTND Size-Activity Distribution

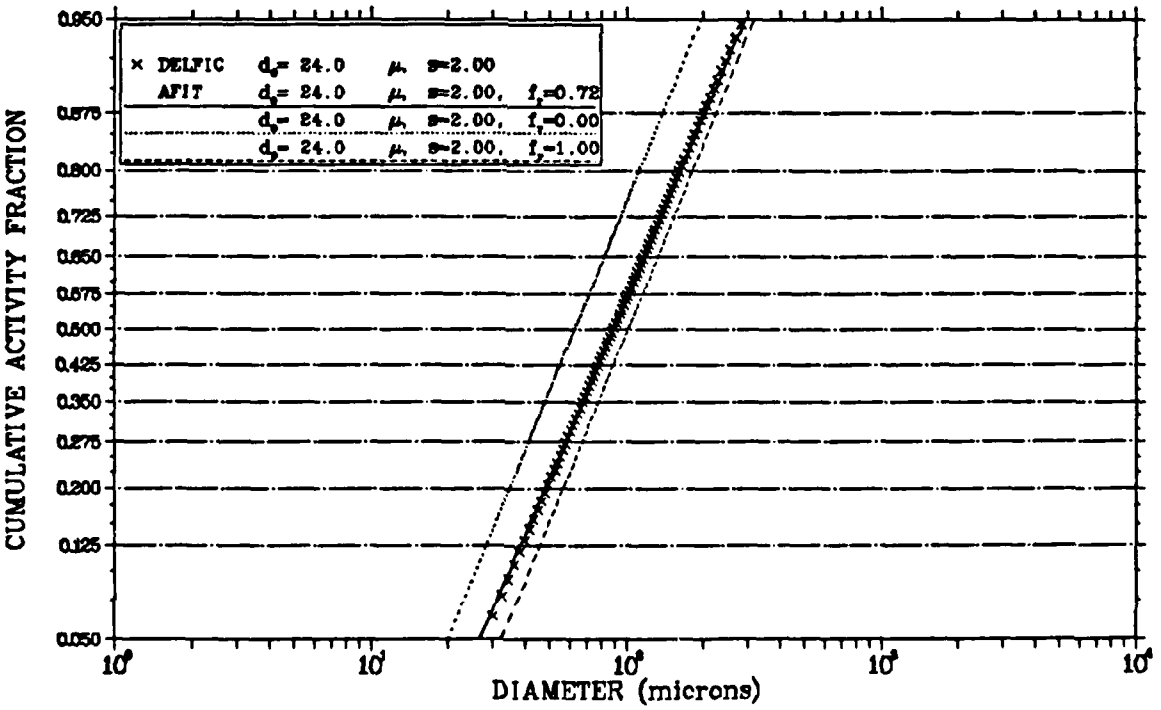

Figure III-6 WSEG-10 or RAND Size-Activity Distribution

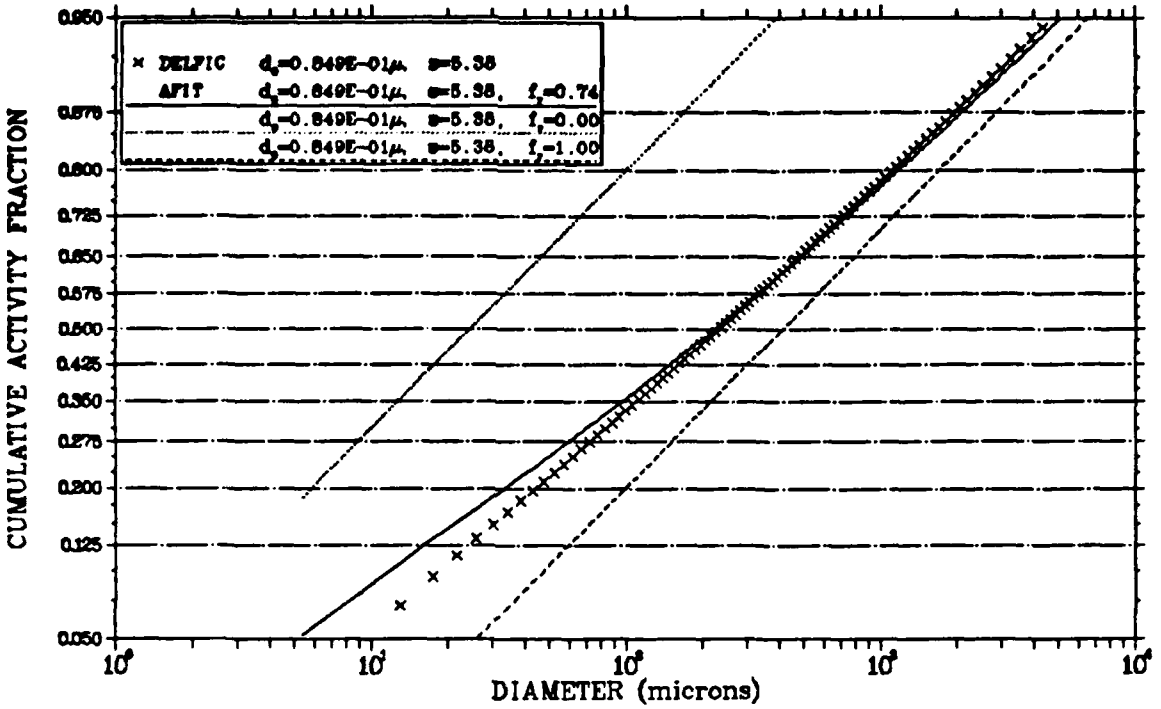

Figure III-7 NRDLC61 Size-Activity Distribution

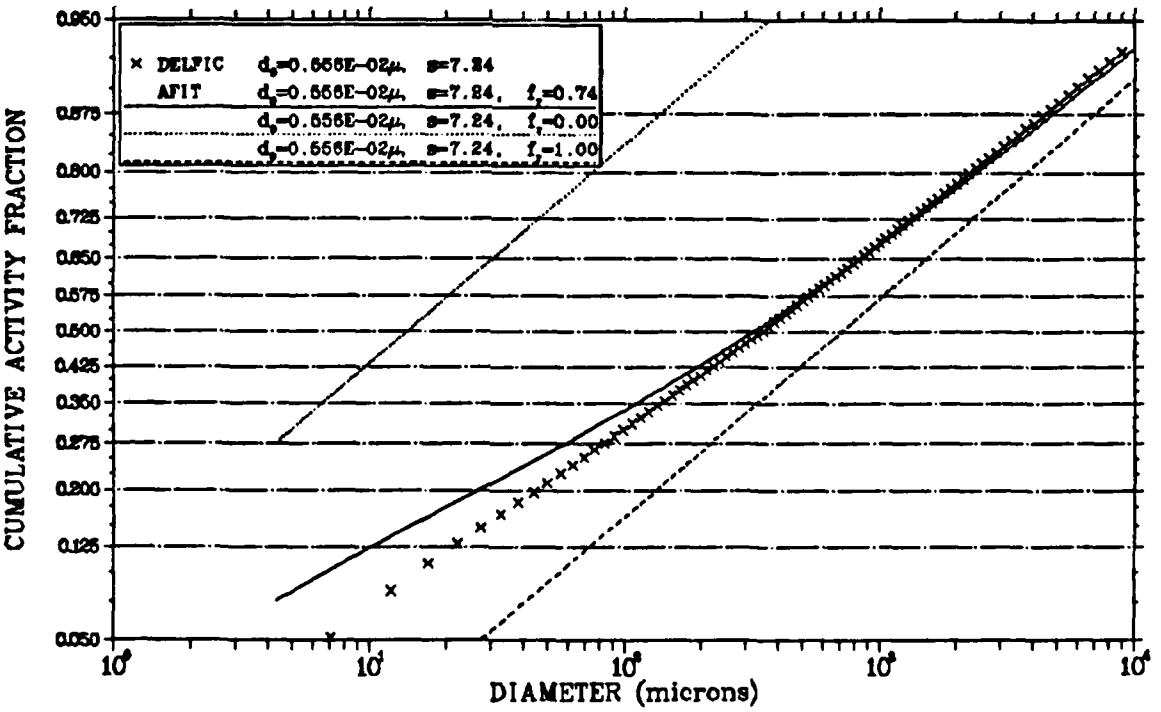

Figure III-8 NRDLN61 Size-Activity Distribution

size-frequency distributions introduced in Chapter II. Also shown are the contributing surface and volumetric distributions and the DELFIC data on which the calculations of f_r for the two-component distribution were based.

Approximations to the Basic AFIT Model

In the preceeding derivation of the AFIT model, g(t) is expressed as an integral over the vertical cloud distribution. Unfortunately, this integral can only be evaluated numerically. The model may be further simplified, however, by a suitable approximation of the integration over the vertical cloud extent.

If the vertical cloud distribution is replaced by a Dirac function at H_c, the cloud degenerates into an infinitesimal wafer at the center height, and the integration becomes a simple matter of evaluating the integrand at H_c. The activity arrival rate, g(t), is then given by equation (14), where both A(r) and dr/dt are evaluated as described above, with $z = H_c$. Figure III-9 compares AFIT model g(t) calculations which used both this "pancake" and vertically distributed gaussian clouds for 1, 10, 100, and 1000 KT yields and the DELFIC default size-frequency distribution. Colarco (16:87) presented similar results for lognormal size-activity distributions and other yields ranging from 1 to 20000 KT. In all cases, there are negligible differences between "pancake" cloud and distributed cloud model results. This occurs because the integrand in equation (16) is nearly symmetric between the integration limits about H_c. It should be

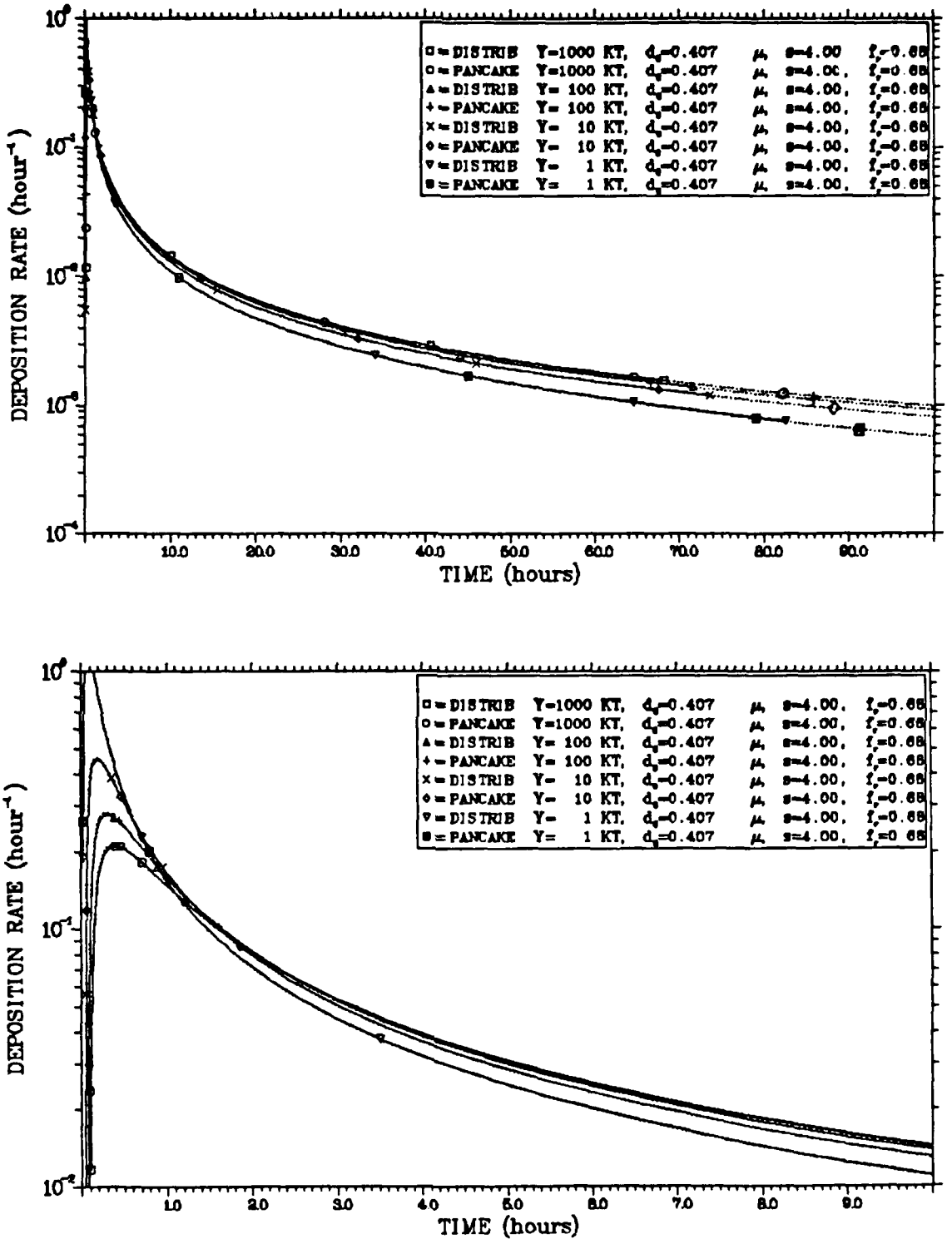

Figure III-9 Distributed and Pancake Cloud Deposition Rates

remembered, however, that any prediction based on a stabilized cloud cap model such as AFIT or WSEG, can be expected to give unrealistic predictions close to ground zero for a low yield explosion, because of neglect of stem fallout. It is also important to note that the "pancake" approximation is used only with respect to evaluation of the integral over altitude in the g(t) expression. Fallout footprint or dose calculations that might be based on g(t) calculated in this manner would still use a distributed cloud in modeling the effects of horizontal wind shear; specifically, the vertical standard deviation of the cloud would still taken as $0.18H_c$. In the following chapter, this "pancake" approximation is used in validating the AFIT model predictions for g(t) against DELFIC's results.

Regardless of the method used to obtain g(t), whether by numerical integration or by use of the "pancake" approximation, equation (2) for the unit time reference dose rate, in which g(t) is used to smear the cloud distribution over the ground, involves an integration of g(t). A suitable analytic approximation for this integration is obtained by expansion of g(t) in a Taylor's series about the downwind time of arrival, t_a, of the cloud center at location x. Retention of only the first two terms yields

$$g(t) \simeq g(t_a) + (t-t_a)g'(t)\Big|_{t=t_a} \tag{35}$$

When this approximation is used in equation (2), and the change of variable, $u = -(x-Vt)/\sigma_x$, is made, the integral in that equation becomes

$$\int_{-x/\sigma_x}^{\infty} du\ (\sigma_x/V)\ f(u)\ f(y,t_a)\ \left[g(t_a) + (u\sigma_x/V)g'(t)\Big|_{t=t_a}\right] \qquad (36)$$

where $f(u)$ and $f(y,t_a)$ represent, respectively, the downwind and crosswind components of $f(x,y,t)$. Now, in the domain $x = Vt_a > 3\sigma_x$, cloud passage begins after zero time, and virtually no error is introduced by extending the lower limit of the above integral to negative infinity (the lower limit already spans a $3\sigma_x$ domain of the leading edge of the cloud). The integral is then one over symmetric limits, and the terms involving $g'(t)$ vanish. Thus, with this approximation, the expression for the unit time reference dose rate becomes

$$\dot{D}_1(x,y) = kYF_f f(y,t_a)g(t_a)/V \qquad (37)$$

which the preceeding derivation shows is accurate to within a linear (not constant) approximation for $g(t)$.

IV. Validation of the AFIT Model Activity Deposition Rate

Obtaining g(t) from DELFIC Data

A major advantage of the smearing model described above is that calculation of fallout pattern dose rate contours is based on independent functions describing cloud geometry and wind. Thus, in verifying the mathematics of the smearing model, one need not be concerned with its ability to reproduce either observed fallout patterns or patterns calculated by some comparison standard like DELFIC. Since the current formulation of the AFIT model does not allow for variable winds, good agreement with actual or DELFIC calculated patterns could be expected only for actual winds that matched the effective wind conditions permitted by the model. Thus, in validating the AFIT model, only the calculated rate of arrival of activity on the ground, g(t), will be compared with the prediction of a reliable standard. DELFIC's prediction of g(t) is chosen as that standard.

Given a well formulated g(t), the model's ability to make reasonable predictions of far field fallout will rest in its treatment of winds. While the current formulation is limited to a wind treatment neither more nor less restrictive than that of WSEG, unlike WSEG, the AFIT model does have a potential for incorporation of variable wind effects. Such an extension of the model, which is capable of producing a curved "hotline", has been reported by Hopkins (20).

Although DELFIC was not originally written to provide a

calculation of g(t), the required data, in the form of cloud wafer grounding statistics and particle activity assignments, are available from the output of the transport and particle activity modules. The general procedure is to calculate the integral of g(t) from zero time (t=0) to arrival time ($t=t_a$), by summing the contributions of individual cloud wafers. The integral curve is then differentiated numerically to obtain g(t).

Comparison of AFIT Model and DELFIC g(t) Results

The AFIT smearing model is validated here by comparison of its predictions for the ground arrival rate of fallout, g(t), with those of the AFIT version of DELFIC (the g(t) calculation was never incorporated into the original ASA version of the code). The DELFIC calculations assumed ^{239}Pu fuel fissioned by high-energy (14 MeV) neutrons; the atmosphere was the U.S. Standard Atmosphere for mid-latitudes, spring or fall. Four yields: 1, 10, 100, and 1000 KT, and six different lognormal particle size frequency distributions were selected; 100 particle size classes were defined by DELFIC for each case. In addition to the DELFIC default particle size distribution, the selected distributions include the five distributions introduced in Chapter II: the four previously used in a DELFIC study by Norment (21:25), and one developed for this study to reproduce the RAND (WSEG-10) size-activity distribution. Figure IV-1 displays the two-component size-activity distributions calculated for the AFIT model and summarizes the size-frequency distribution parameters used both in the AFIT

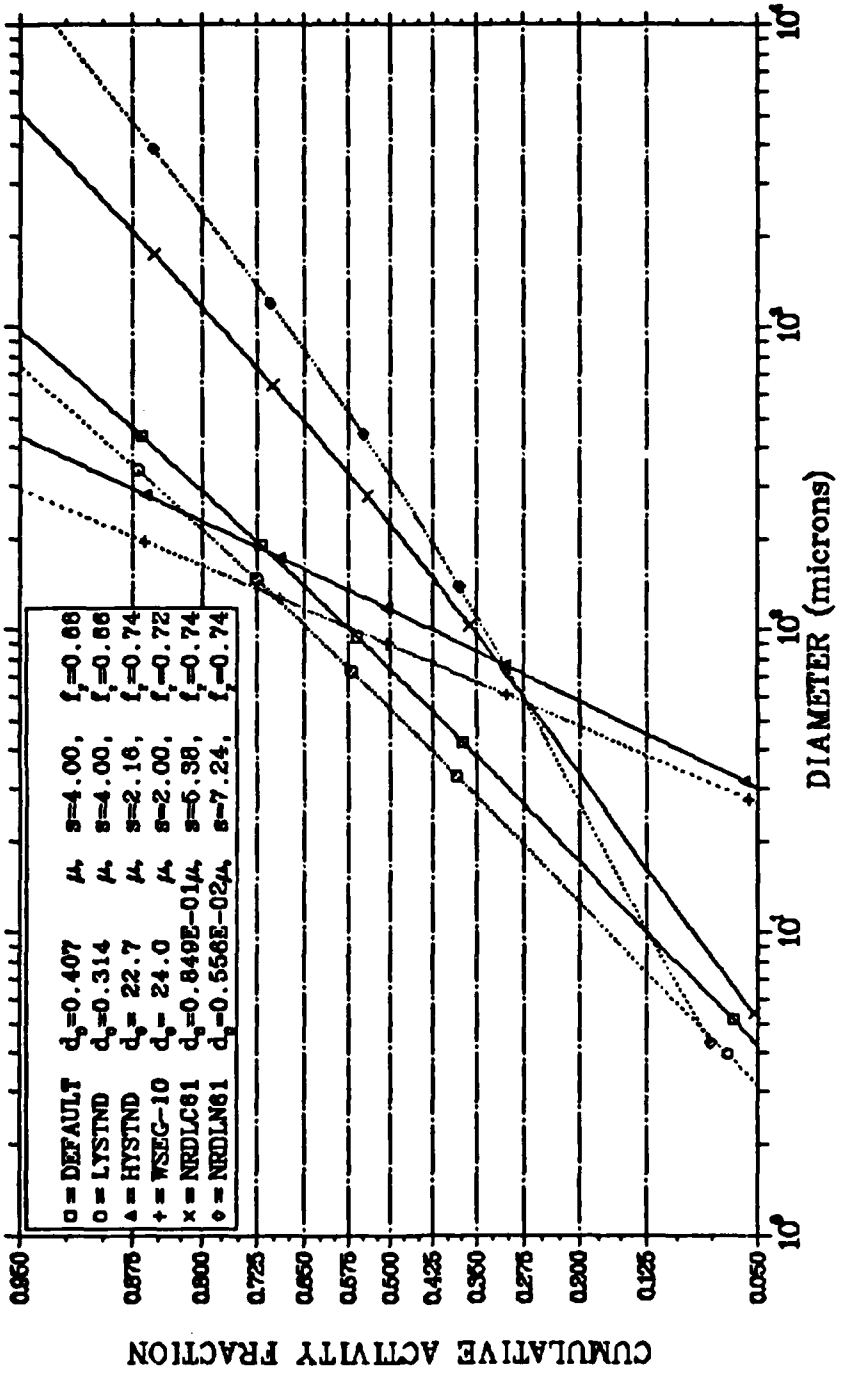

Figure IV-1 Size-Activity Distributions for the AFIT Model

calculation and by DELFIC. Figures III-3 through III-8 previously compared the AFIT and DELFIC distributions.

Figures IV-2 (presented here) and C-1 through C-23 (Appendix C) present comparisons of the DELFIC results for the activity arrival rate with results of the "pancake" cloud version of the AFIT smearing model. Figures IV-2 and C-1 through C-5 are 1000 KT cases; Figures C-6 through C-11 are 100 KT cases; Figures C-12 through C-17 are 10 KT cases; and Figures C-18 through C-23 are 1 KT cases. Several features of these comparison figures are immediately evident. First, and perhaps most significant, unlike the WSEG model calculation presented in Figure III-1, the AFIT smearing model closely parallels the behavior predicted by DELFIC for g(t) for every size-activity distribution at every yield; the agreement is particularly good for the DELFIC Default and Low Yield Standard cases. The trend is for better agreement for higher yields and later times. This is what one might expect in view of the AFIT model's initial condition of a stabilized cloud over ground zero. At higher yields, the stem, which the AFIT model lacks, is a less significant source of activity; and at later times, one is concerned, in both models, with the relatively small particles which began their fall from the cloud cap. The trend of the AFIT model to predict slightly higher late time deposition rates than DELFIC is explained by the AFIT model's assignment of a somewhat larger fraction of activity to the smallest particles.

The relative significance of the stem depends on the size-activity distribution, as well as on the yield. The worst agreement between DELFIC and the AFIT smearing model occurs for the extreme NRDL

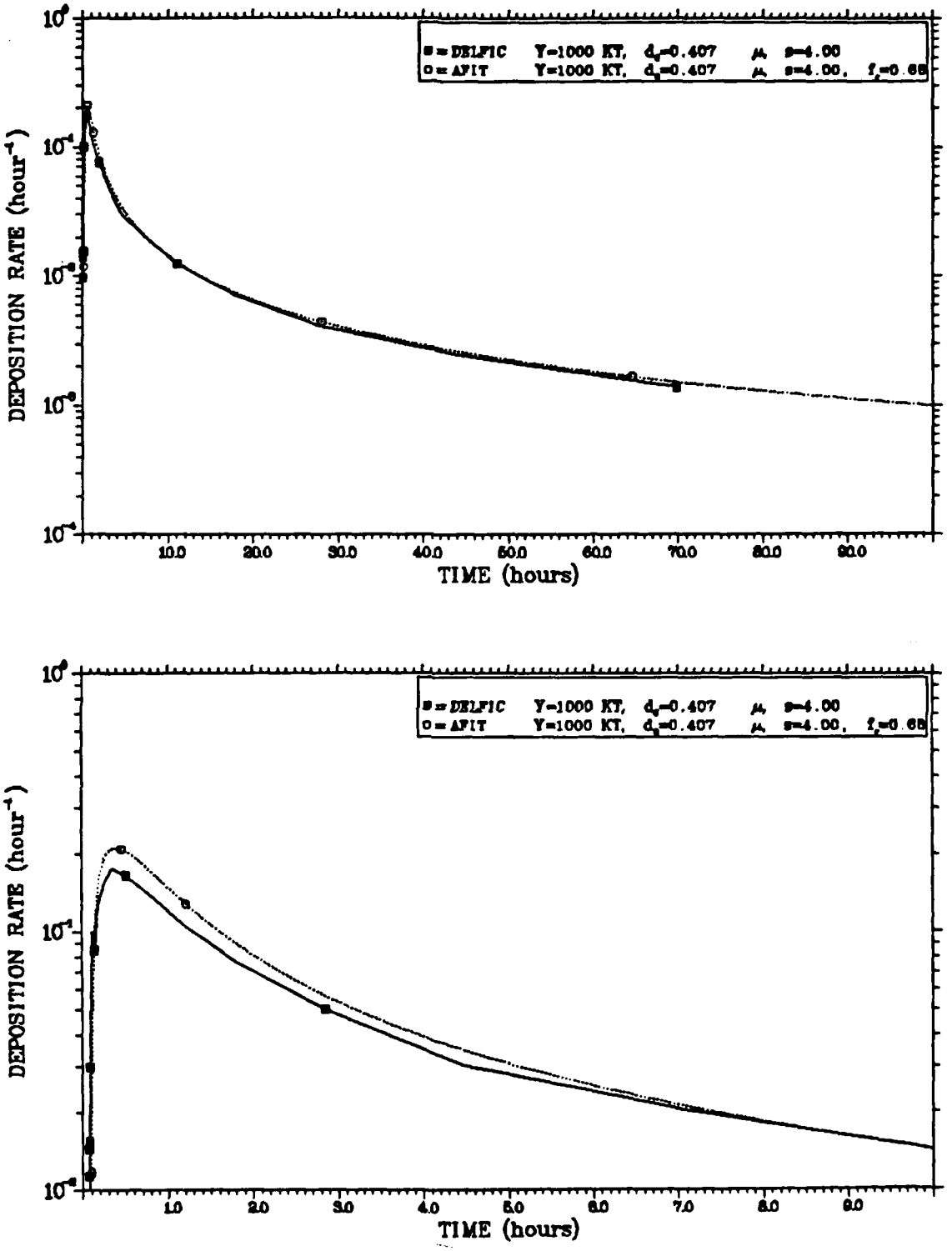

Figure IV-2 Deposition Rates for the DEFAULT Distribution

distributions, N61 and C61. Since these two distributions have rather large geometric deviations (large logarithmic slopes), they include a relative abundance of very large particles. In the DELFIC simulation, such particles reside primarily in the stem, from which they are deposited earlier than they can be from the AFIT model's stabilized cloud. The net effect is that the peak in the AFIT g(t) is generally higher and occurs later than does the peak in the DELFIC g(t) for these distributions.

At early times (less than about 5 hours) and especially at low yields, the DELFIC curves display slope discontinuities which are not present in the curves for the AFIT model. This structure arises from the numerical differentiation of DELFIC's histogram for the fraction of total activity down as a function of time. The histogram cannot be smooth because of the cloud wafer quadrature. This quadrature also places a limit on the ability of the differentiation to resolve the peak in the arrival rate function. DELFIC's quadrature is similarly responsible for the occasional late-time discontinuities in the arrival rate slope.

The truncation of the DELFIC curves at about 70 hours, or earlier in the case of the WSEG or HYSTND distributions, is an artifact caused by the numerical differentiation. Since the arrival rate at each time was taken to be the slope of the deposited activity fraction between that time and the next interval, and only points which fell within the zero to 100 hour plotting interval were considered, the slope was never calculated beyond 70 hours. The WSEG and the HYSTND cases terminate earlier because the deposition rate for the succeeding time point was

zero.

The impact of the differences in activity grounding rates on the total fraction of activity deposited is illustrated by Figures IV-3, IV-4, and IV-5, for a 1 KT yield, with the DEFAULT, WSEG-10, and NRDLN61 distributions. These figures demonstrate that the most significant differences occur prior to about 2 hours; after that, the AFIT and DELFIC deposition fraction curves are nearly parallel or slightly convergent. For higher yields the agreement is better; results for the other distributions are similar.

To the extent indicated by the comparison with DELFIC results, the AFIT model's formulation for the ground arrival rate of activity, g(t), now stands validated. Although its impact on g(t) appears to be minor, the data presented above suggest that a significant area for improvement in the g(t) determination is in the modeling of cloud geometry.

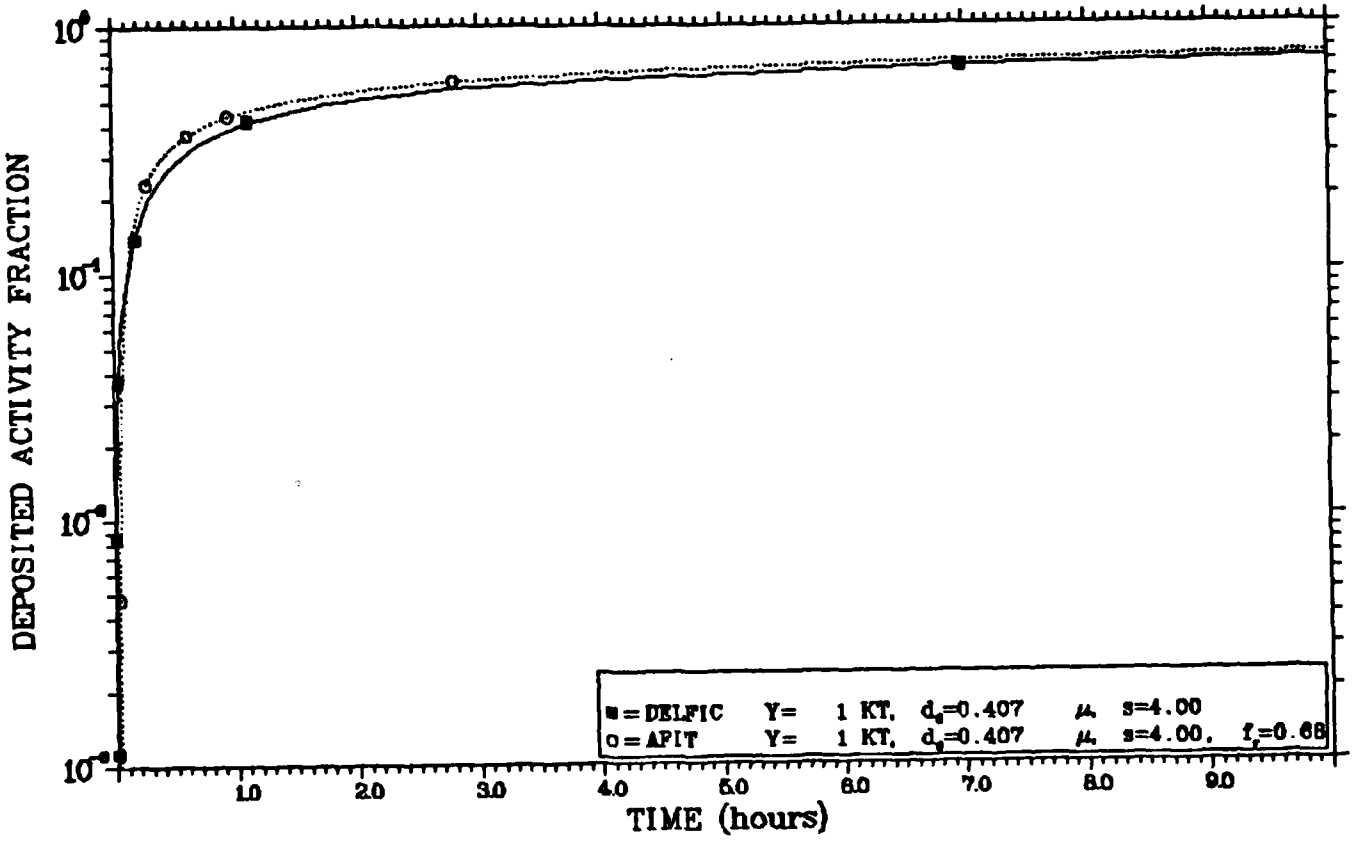

Figure IV-3 Activity Deposition for the DEFAULT Distribution

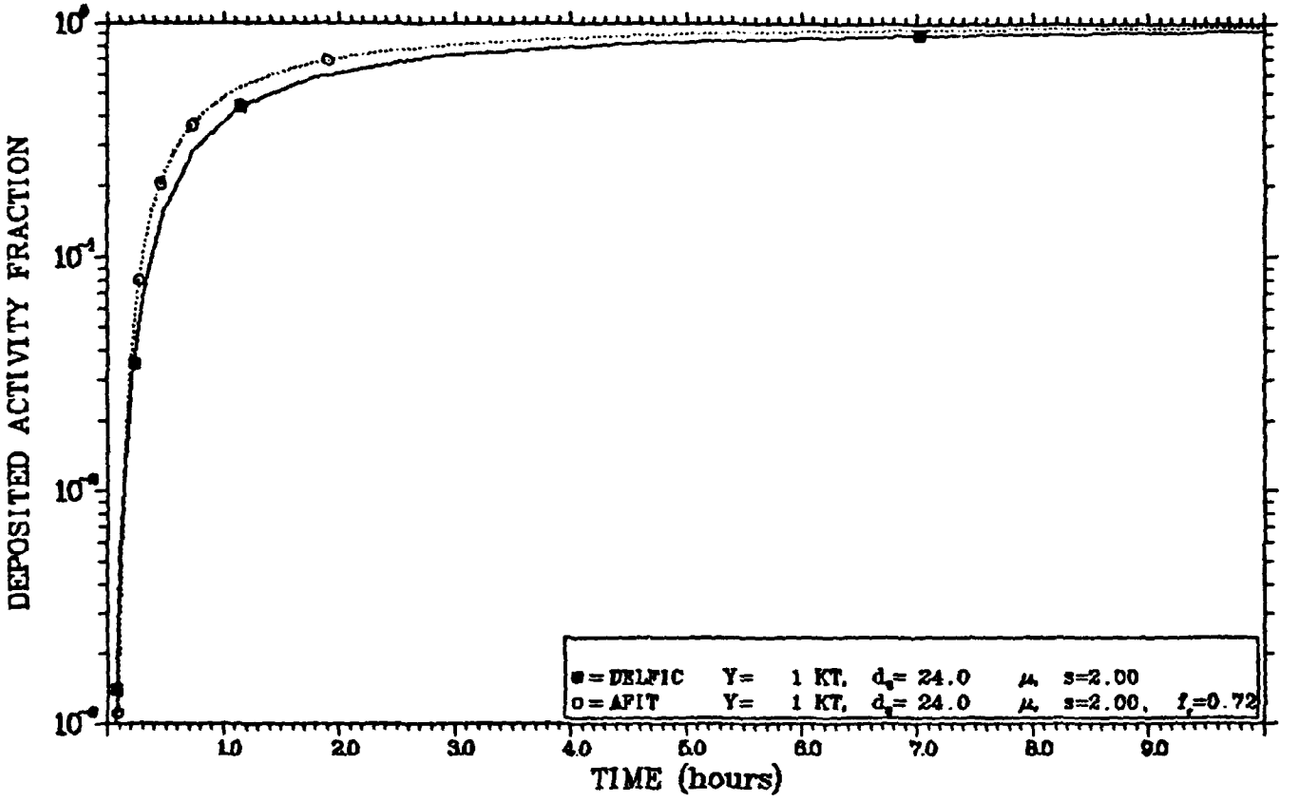

Figure IV-4 Activity Deposition for the WSEG-10 Distribution

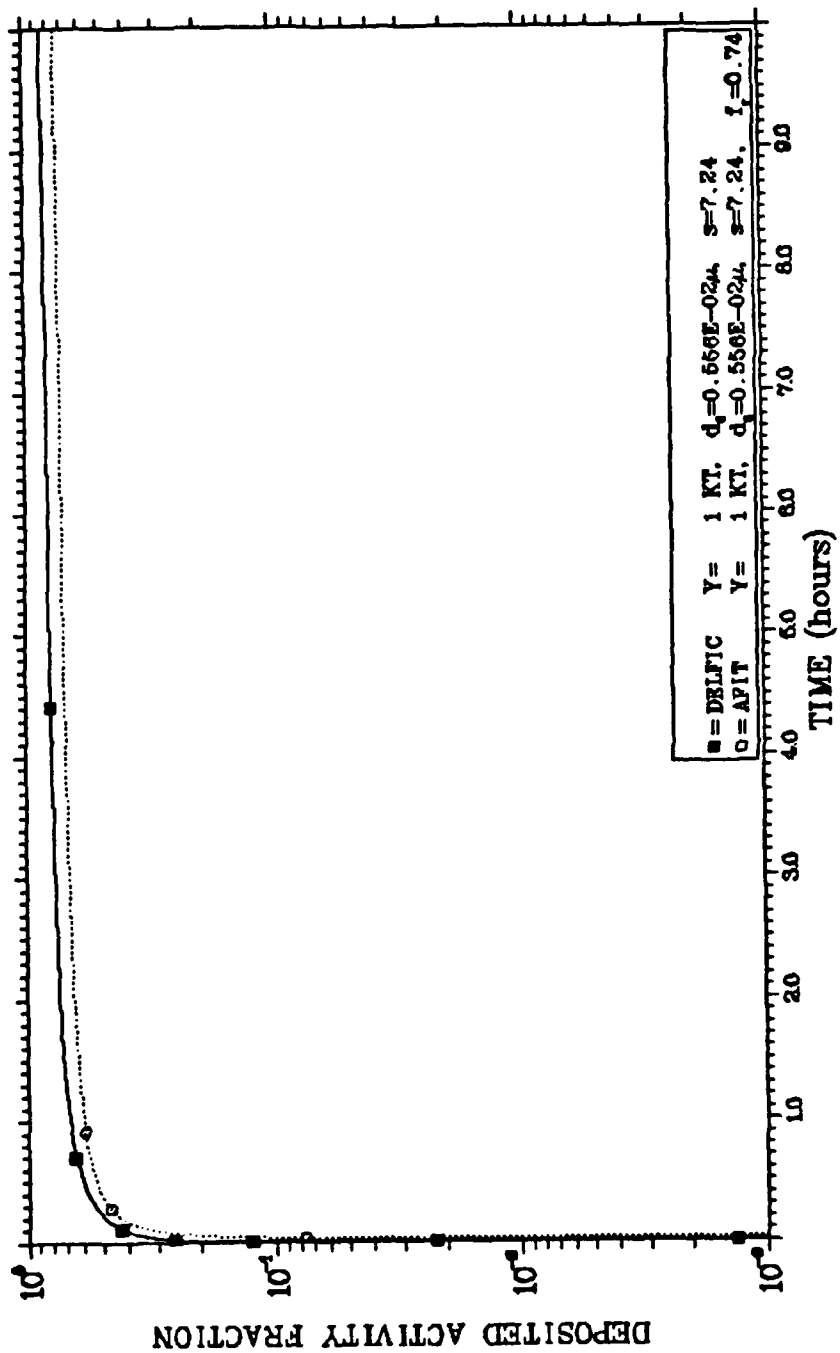

Figure IV-5 Activity Deposition for the NRDLN61 Distribution

V. Sensitivity of the AFIT Model to Parameters of the Particle Size-Activity Distribution

A key feature of the cloud smearing approach to fallout modeling is the use of independent functions to describe the rate of arrival of cloud activity on the ground and the horizontal spatial distribution of that activity in the cloud. Together, these functions produce the fallout footprint. By itself, the horizontal cloud distribution function reflects the effects of wind, wind shear, and turbulence on the advective transport of the debris cloud as it drifts downwind from the detonation site. On the other hand, the activity arrival rate function, g(t), expresses the vertical processes involved in fallout. It reflects the combined relationship between the initial vertical distribution of activity, h(z), the particle size distribution of activity, A(r), and the physical laws describing the gravity settling rates of fallout particles. In the smearing model, gravity settling is expressed as dr/dt: the initial altitude and time-dependent rate of change in the size of arriving particles. Thus the smearing model separates the horizontal process of advective transport of fallout from the vertical process of particle settling. This feature permits the activity arrival function to be used as a measure of the sensitivity of the model, without the the need to consider the complicating effects of horizontal transport under the influence of prevailing winds.

Among the three factors determining the activity arrival function, attention is focused here on sensitivity to the parameters defining the

particle size-activity distribution. The following observations are offered in partial justification of this focus. Since the particle fall dynamics incorporated in the AFIT model's evaluation of dr/dt, or minor modifications thereof (1:25), are considered to represent the state-of-the-art in modeling the free-fall of spheres in a viscous medium, there is little incentive for considering older approximations. Norment (21:32) has previously examined the impact of the assumption that fallout particles are spherical, rather than some less regular shape, and found at most minor impact on fallout prediction. With regard to the vertical distribution of activity, it was observed previously in Figure III-9 that the details of a symmetric distribution of activity about the cloud center height have a negligible effect on the ground arrival rate of activity, g(t). The average cloud height, on the other hand, is a direct measure of the yield. For a given size-activity distribution, it determines, through the dr/dt relation, the nature of the arrival rate curve. The figure just cited shows that the fractional arrival rate of activity is moderately sensitive to yield. While the yield varies over three orders of magnitude, the fractional arrival rate varies by less than one order of magnitude. Increasing the yield decreases the magnitude of the peak in the g(t) curve, shifting the peak to slightly later times. In compensation, the late time arrival rates are higher for higher yields.

Although the distribution of activity with fallout particle size is of prime significance in the calculation of g(t), determination of an appropriate distribution is uncertain. Experimental support for distributions such as the DELFIC default particle size-frequency

distribution is generally meager and potentially biased by sampling techniques. The DELFIC default distribution is based on Nevada test site debris. Its applicability to predicting fallout resulting from a detonation on hard rock or in a large city is dubious. In short, one of the most important factors in the prediction of fallout is largely unknowable. Thus, it is important to understand the impact of the uncertainties in distribution of activity with particle size on fallout prediction. This is impossible with the current mainstay of operational type studies, WSEG-10, because in WSEG the activity distribution and fall rates have been pre-combined. With the AFIT smearing model, however, the impact of varying the individual parameters is directly observable.

The sensitivity of the AFIT smearing model to the distribution of activity with particle size was examined by observing the effects on activity grounding times of varying the distribution parameters. The extreme sensitivity of the model to such variations is readily apparent from an examination of the deposition rate data presented in Figures IV-2 and C-1 through C-23 as a part of the model validation. Here, with the DELFIC default size-frequency distribution as a baseline, each of the three parameters that define the AFIT model's two-component size-activity distribution are varied: the refractory activity fraction, that is, the fraction of activity distributed volumetrically, f_r, the particle size-frequency median diameter, d_o, and the factor defining the dispersion of particle sizes about that median, the geometric standard deviation, s.

Figure III-2 showed that values of the refractory activity

fraction, f_r, calculated on the basis of DELFIC's particle activity assignment data, were insensitive to yield and only slightly dependent on choice of particle size distribution. Although the observed range of f_r was only from 0.66 to 0.74, the DELFIC calculations all assumed fission of ^{239}Pu fuel by 14 MeV neutrons. Different fuels, different neutron energy spectra, or the presence of significant induced activity species could significantly alter the fractionation behavior of the debris. Here the entire range of possible values for the refractory activity fraction is considered. Figure V-1 displays the effects on the size-activity distribution of varying the fractionation parameter, f_r, from 0.0, corresponding to a totally surface distribution of activity, to 1.0, corresponding to a totally volumetric (refractory) distribution. Although this leads to a variation in the size-activity medians spanning the range from surface to mass distribution median, the dispersion about those medians is similar to that of the size-frequency distribution itself. Increasing the refractory activity fraction has the effect of increasing the median of the size-activity distribution. Figures V-2 through V-5 show the effects of these variations on the fractional arrival rate of activity for yields ranging from 1 to 1000 KT. For each yield, the variations in the refractory activity fraction produce a family of curves lying within an envelope bounded by the surface and volume distribution results. At early times, the more refractory distributions lead to higher peak deposition rates; at late times they lead to lower deposition rates. The spread in peak rates is about one order of magnitude. The cross-over from "early" to "late", the nodal point in the envelope,

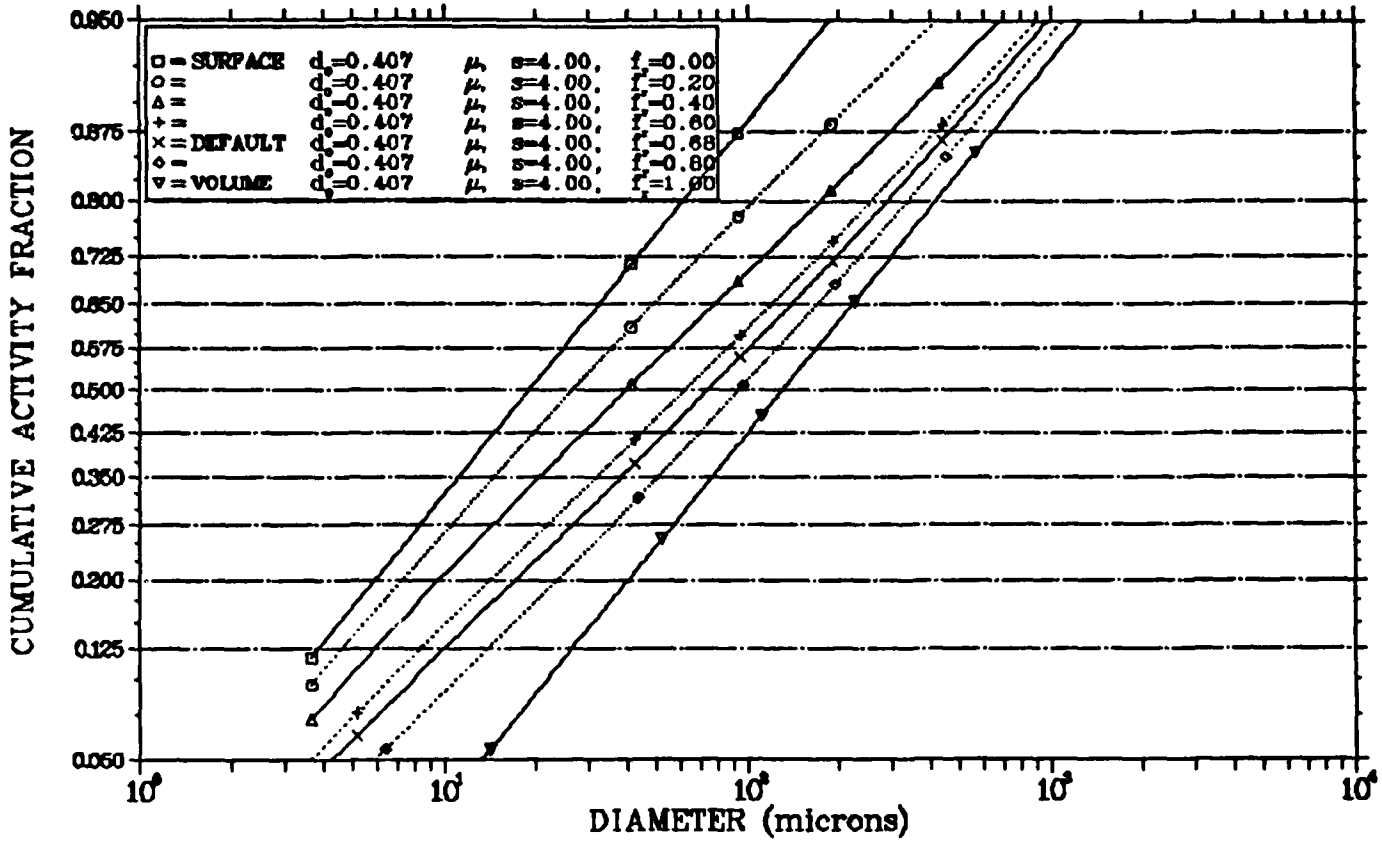

Figure V-1 Activity Distribution Sensitivity to Fractionation

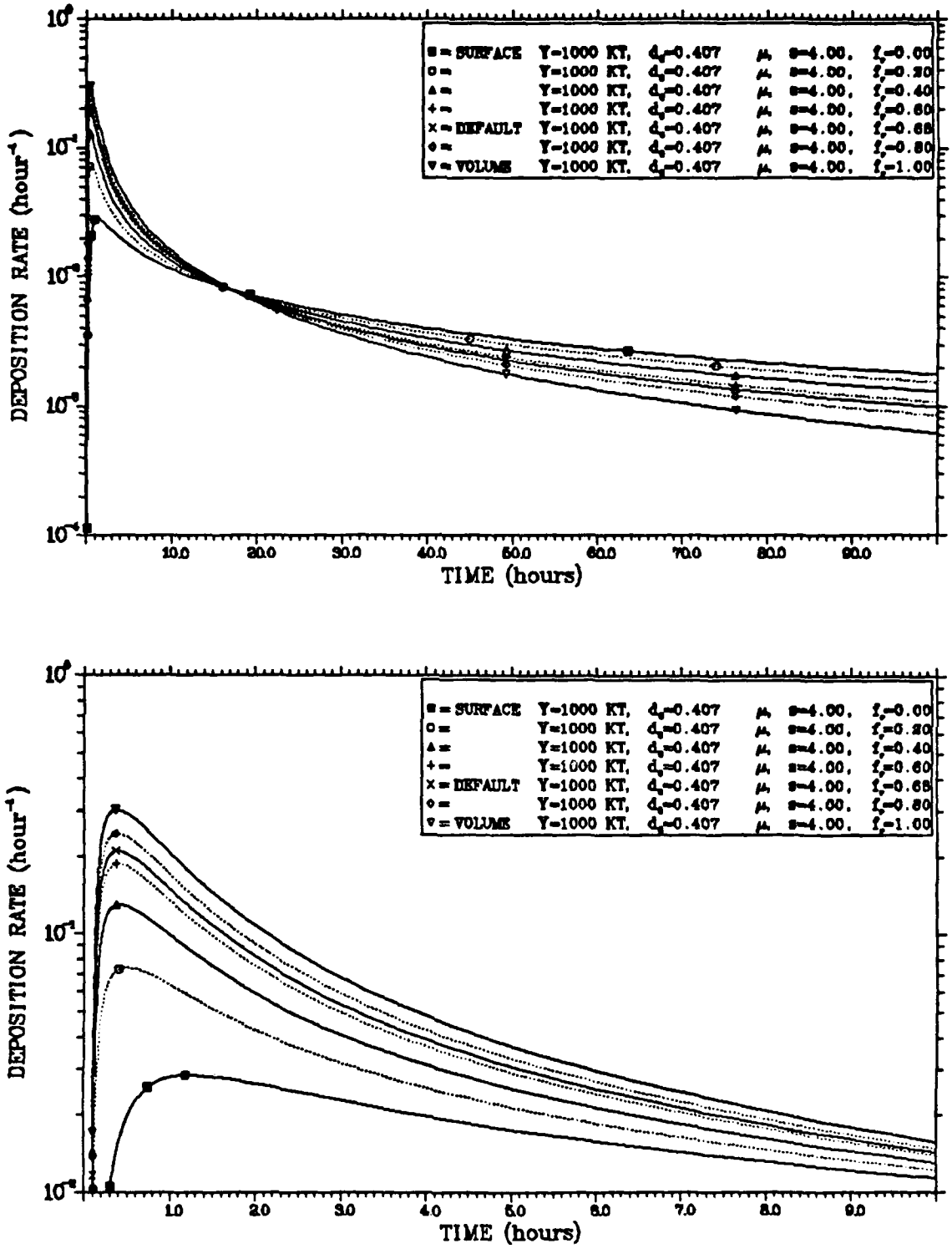

Figure V-2 Deposition Rate Sensitivity to Fractionation

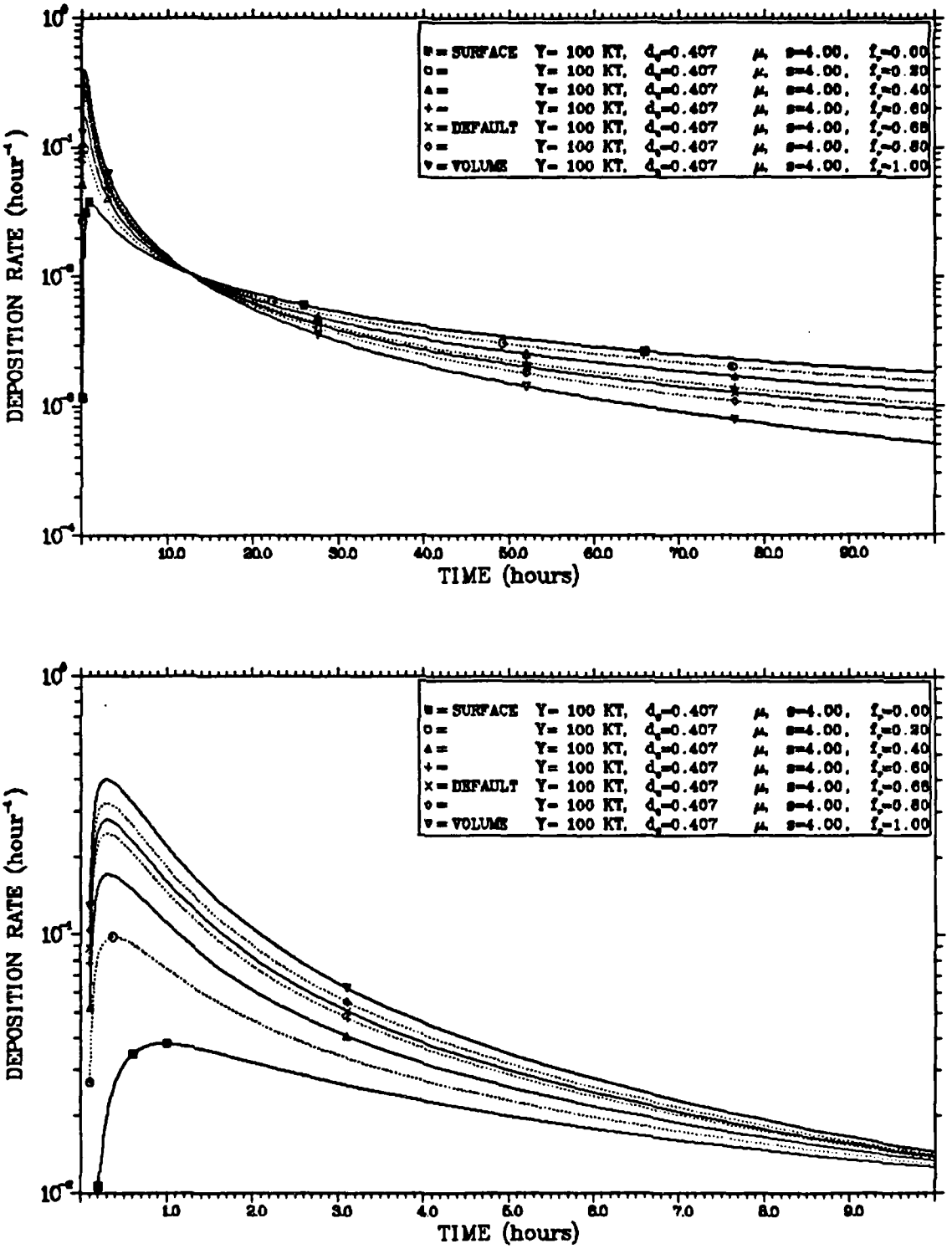

Figure V-3 Deposition Rate Sensitivity to Fractionation

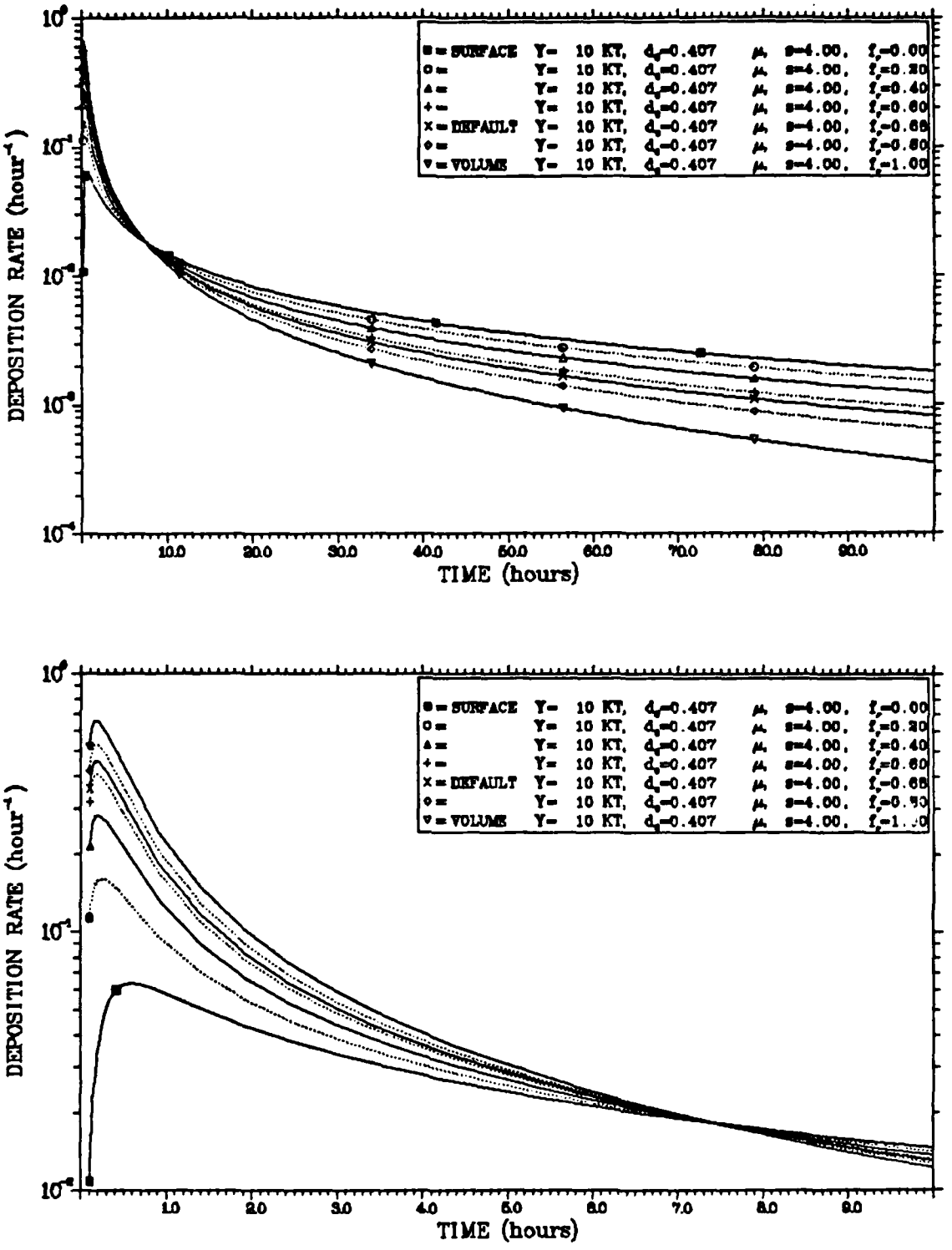

Figure V-4 Deposition Rate Sensitivity to Fractionation

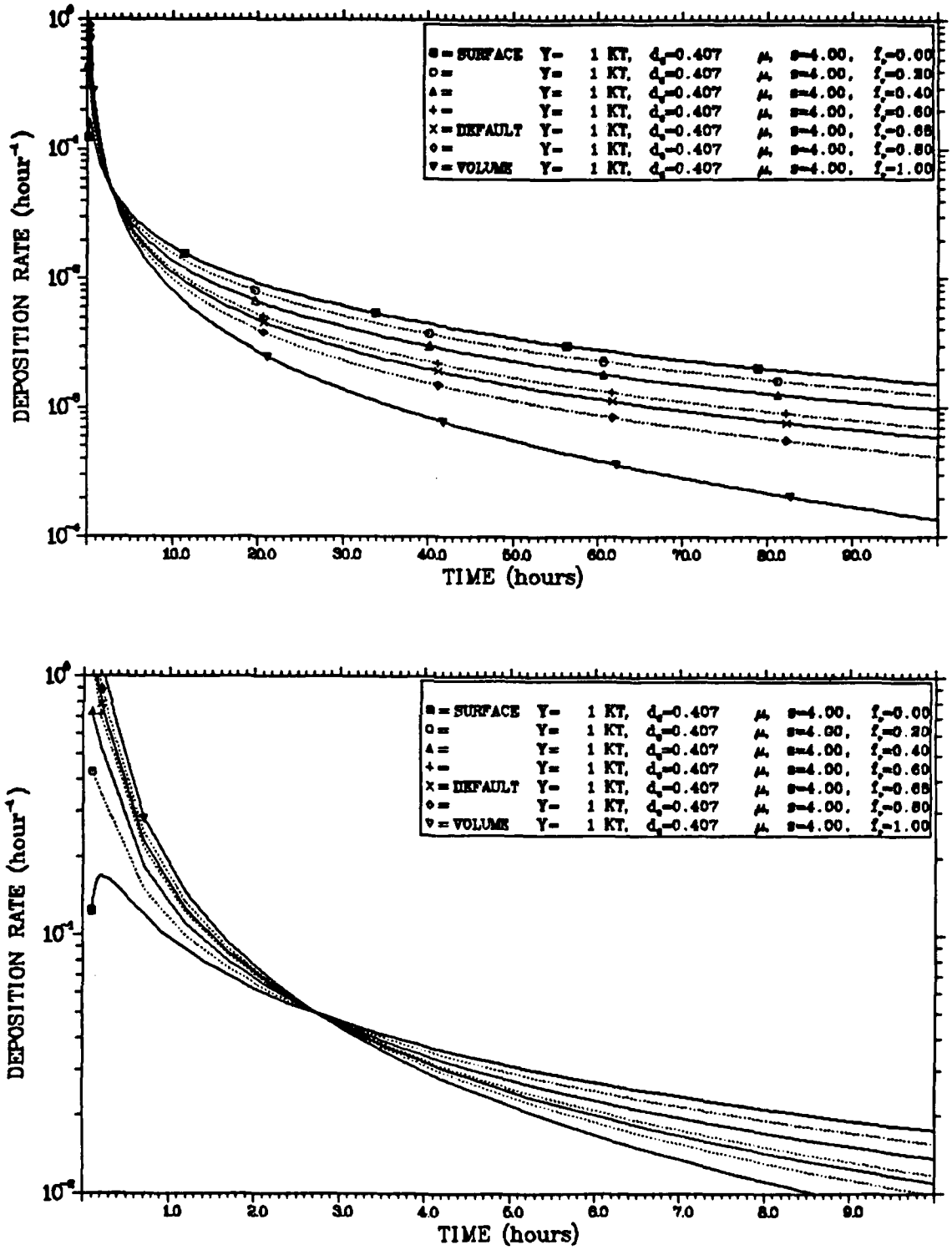

Figure V-5 Deposition Rate Sensitivity to Fractionation

occurs at the time corresponding to deposition of particles whose size is the geometric mean of the surface and volume distribution medians, the median of the 2.5th moment of the size-frequency distribution. To either side of the nodal time, the variation of g(t) with f_r is monotonic. The node itself shifts to later times as yield increases and the time required for any fixed size particle to be deposited increases. Thus, the magnitude and timing of the peak, as well as the late time slope of the activity arrival rate function are all influenced by the choice of the refractory activity fraction.

Figure V-6 displays the effects on the size-activity distribution of variations in the size-frequency median diameter, d_o, from one tenth to ten times the DELFIC default value of 0.407 μm. This leads to a comparable two order of magnitude span between the medians of the corresponding size-activity distributions. Again, the dispersion of activity about the size-activity medians is similar to that of particle sizes about the size-frequency median. Since the impact of these variations is a more extreme example of the same effects as those produced by fractionation variations, but without the surface and volume distribution bounds, only the deposition rate results for the 1000 KT example are presented (Figure V-7). As with the previous fractionation variations, there is approximately a one-to-one relationship between peak arrival rate differences and size-activity median variations. The peak in the activity arrival rate curve for the distribution with the largest median occurs earlier and is higher and steeper than the peaks for the other distributions. Since this distribution has relatively little activity associated with the smaller

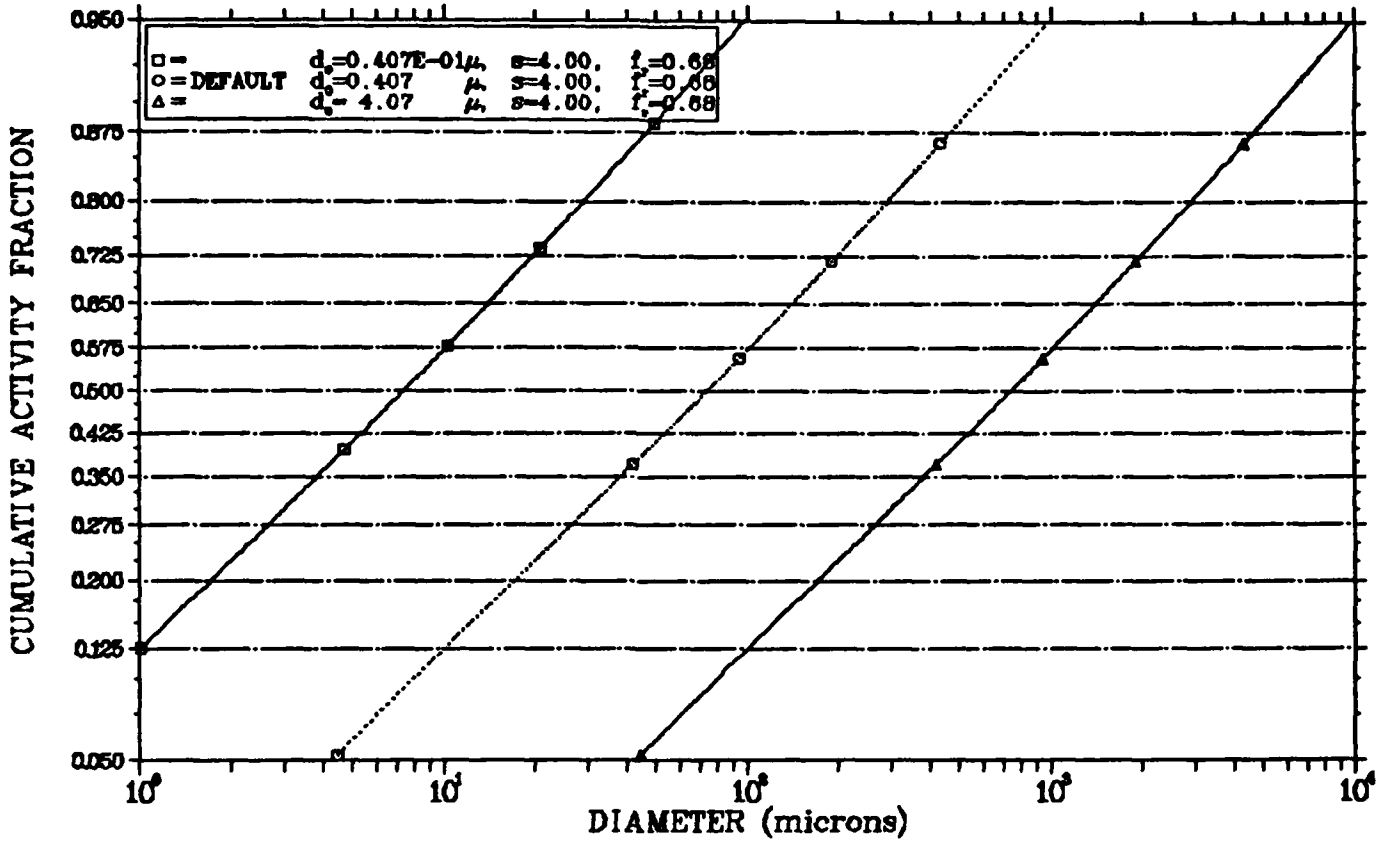

Figure V-6 Activity Distribution Sensitivity to Size Median

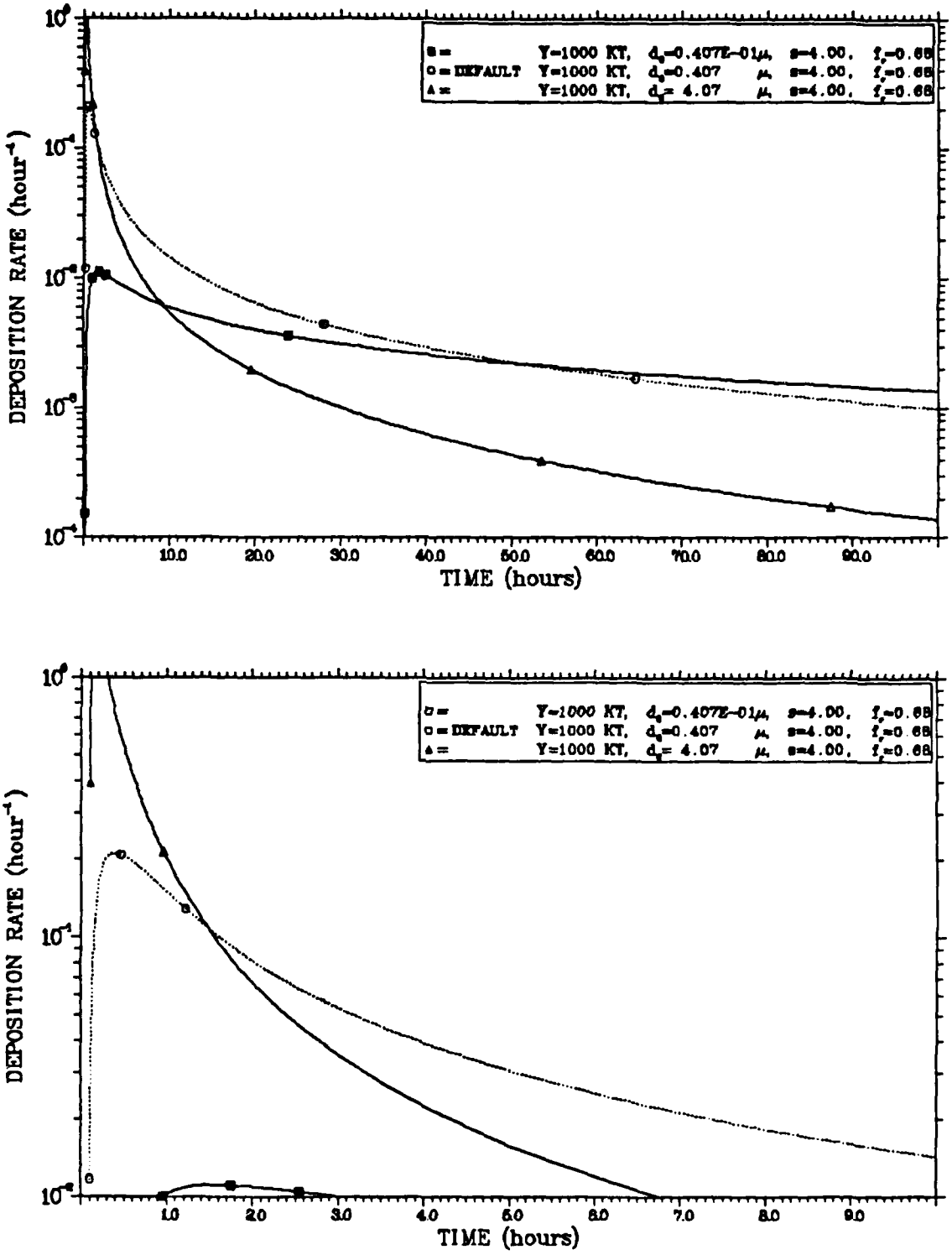

Figure V-7 Deposition Rate Sensitivity to Size Median

particles, its activity arrival rate declines more rapidly at times beyond the peak than does the rate for the other distributions. On the other hand, the arrival rate curve for the distribution with the smallest median rises to a broad maximum. Since this distribution contains an abundance of activity on small particles with long fall times, the activity arrival rate decreases slowly with time.

Figure V-8 displays the effects on the size-activity distribution of variations in the dispersion of particle sizes about the median, as measured by the geometric standard deviation of the distribution, s. Here, s has been allowed to vary by one unit above and below the standard value of 4.0 for the DELFIC default distribution. In appreciating the effect (nearly an order of magnitude) that this small variation in the geometric standard deviation has on the size-activity median, it is helpful to recall the expression for the medians of the various moment distributions of the size-frequency distribution, equation (32). Although the AFIT model's two-component size-activity distribution is not lognormal, but rather the sum of two lognormal distributions, with a refractory fraction of 0.68, its median will lie between that of the 2.5th and third moment distributions. Since the median diameter of the size-frequency distribution is 0.407, even the median of the surface distribution is dominated by the second term in equation (32) involving the geometric standard deviation. In fact, the size-activity distribution with the small dispersion of particle sizes (s=3) has a median smaller than that of the distribution of surface area for the baseline distribution, and the distribution with the large dispersion of particle sizes (s=5) has a median larger than that of the

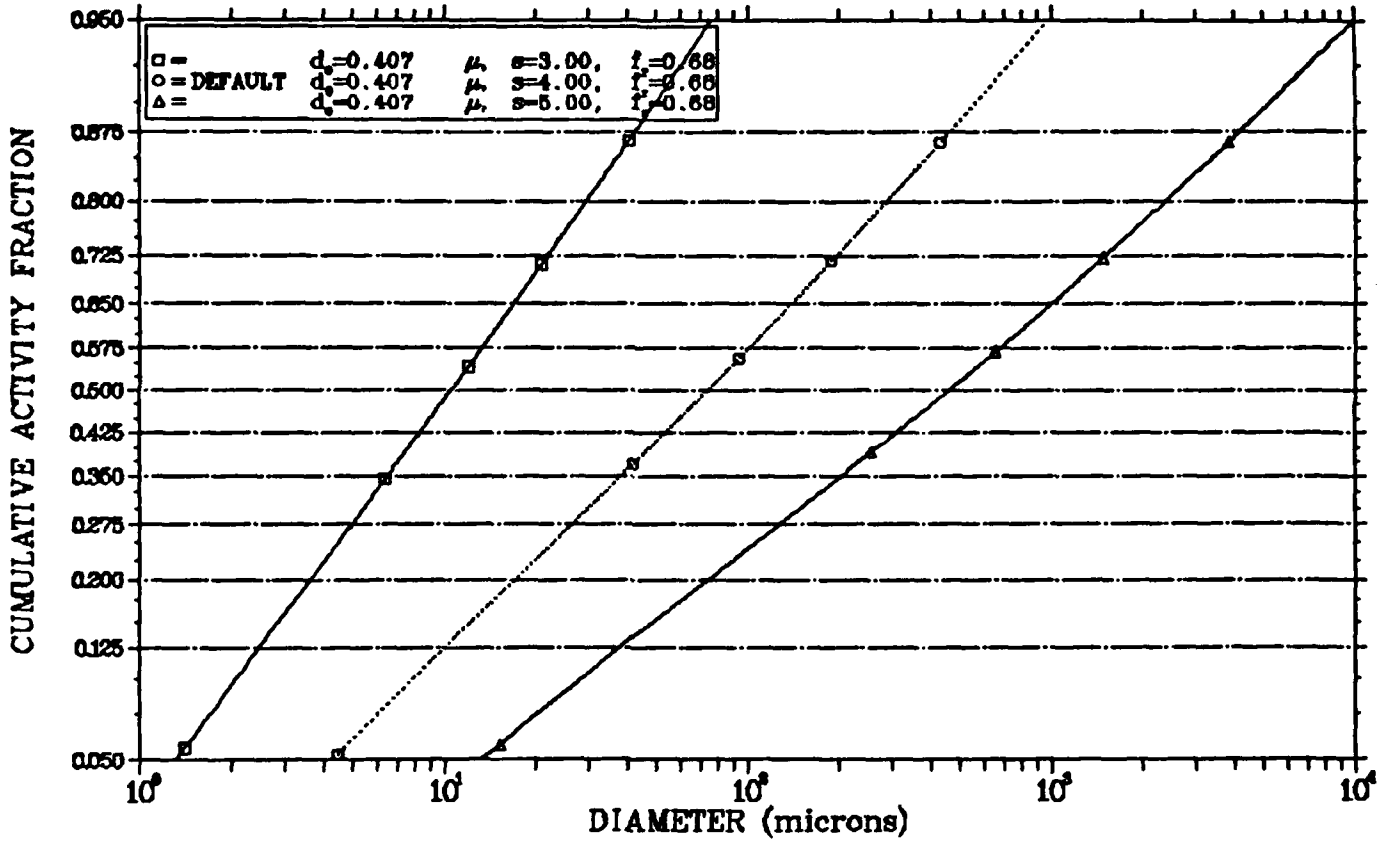

Figure V-8 Activity Distribution Sensitivity to Size Dispersion

distribution of volume for the baseline. As a result, Figure V-9 shows that the small and large deviation deposition rate curves bracket the results presented previously in Figure V-2, which considered fractionation variations.

This analysis has shown that the choice of the particle size-frequency distribution and the partition of activity between volume and surface modes of distribution are of paramount significance to fallout model predictions.

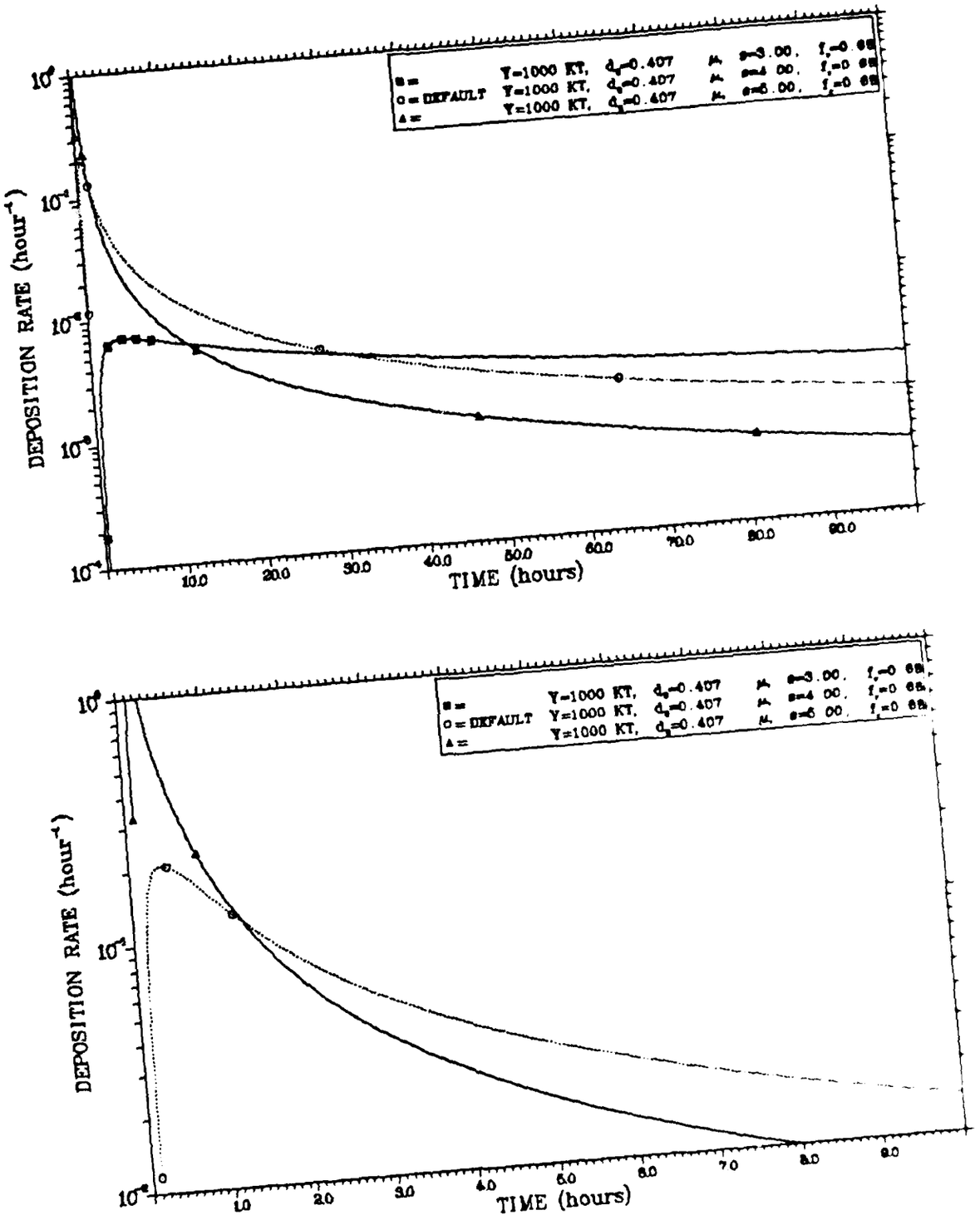

Figure V-9 Deposition Rate Sensitivity to Size Dispersion

VI. Conclusion

This investigation has pursued two methods for improving far field fallout prediction capability, identified above as cloud wafer smoothing and whole cloud smearing. In the former approach, the advection-plus-settling transport algorithm in the state-of-the-art disc tosser code, DELFIC, as received from Atmospheric Sciences Associates, was upgraded to improve overlap of grounded cloud wafers by spreading their contents over a ground area that more accurately represented the true dispersal of the wafer contents. By maintaining the contiguous nature of cloud wafer boundaries from cloud rise through ground deposition, it was possible to guarantee that no voids would exist in downwind fallout patterns, regardless of the distance from the burst location. The approach is only partially successful, however, in that realism in far field predictions by a disc tosser requires the overlap at each ground point of several cloud wafers. Otherwise, the far downwind dose rate contour shapes are determined primarily by the assumed horizontal distribution of activity in each wafer of the stabilized cloud.

In the second method of fallout modeling, cloud wafer smoothing is carried to the limit by treating the whole cloud as a single wafer composed of activity distributed in a continuous manner over the carrier soil particle distribution. A technique was developed to smear the cloud contents continuously over the ground. Although the smearing

model retains the potential for incorporation of a vertical wind profile, within the scope of this investigation, that capability was sacrificed, with attention focused on calculation of the fractional arrival rate of activity on the ground, g(t), by a method not restricted as disc tossers are, to regions relatively close to ground zero. The method of calculating g(t) described here and dubbed the AFIT smearing model has been shown to produce g(t) values which agree well with DELFIC predictions.

By providing an accounting for fractionation and a means to perform sensitivity analyses, the AFIT model introduces capabilities not included in earlier smearing models. The model achieves a distinct advantage by decoupling the effects of the various input parameters. The fractional ground arrival rate of activity, g(t), is determined by the initial l distribution of activity, by the size-frequency distributior ained soil particles, by fractionation of activity between volum id surface distributions, and by particle settling rates. In contrast, g(t) is completely independent of the horizontal distribution of activity in the cloud, of horizontal turbulent growth of the cloud, and of wind speed and shear. As a result, since the parameters which influence g(t) are directly and individually accessible, the AFIT model becomes a useful tool in surveying the sensitivity of predictions to variations in those parameters.

The sensitivities of the AFIT smearing model to variations in yield (vertical distributio of activity) and distribution of activity with particle size (including fractionation effects) were implicitly

demonstrated by the various comparisons with DELFIC results during the validation phase; sensitivity was explicitly considered in Chapter V, through variation of the parameters of the two-component size-activity distribution: the fractionation parameter, the size-frequency median, and the size-frequency geometric standard deviation. The peak time and maximum value, as well as the late time slope of the fractional activity arrival rate curve were found to be extremely sensitive to the geometric standard deviation of the size-frequency distribution. This parameter directly affects both the median and dispersion of the size-activity distribution. When the size-frequency median alone or the refractory activity fraction are varied, the median of the resulting activity distribution is altered proportionately, while the dispersion of the activity distribution remains similar to the dispersion of the frequency distribution. As the refractory activity fraction varies between zero and one, the size-activity median and the peak magnitude of the fractional arrival rate vary by an order of magnitude or more. Thus, the AFIT model is extremely sensitive to the particle size-frequency spectrum and to the partition of activity between volume and surface modes of distribution.

The validation of the AFIT model prediction for g(t) by comparison to DELFIC results demonstrates the model's competence as a method for predicting the ground arrival rate of activity. Since it is capable of treating fallout transport without resort to numerical quadrature, it can suffer none of the artificial structure problems inherent in disc tosser codes. In its treatment of winds, however, it is neither more

nor less competent than its predecessor, WSEG. This is a productive area for further model improvement. In view of the strong sensitivity to the fractionation parameter, a direct, first-principles calculation of f_r would also be a welcome addition to the model.

Appendix A

Fallout Patterns Produced by the AFIT Version of DELFIC

Appendix A

Fallout Patterns Produced by the AFIT Version of DELFIC

The following figures (A-1 through A-24) present fallout contour pattern predictions generated by the AFIT version of DELFIC. The particle size-frequency distribution parameters were presented in Table II-1. Figure II-4 showed the corresponding DELFIC activity assignments. The activity calculations assumed fission of ^{239}Pu by 14 MeV neutrons (Fission ID = P239HE), and a soil particle melting point of 2200°K. The quantities "D(MED)" and "S(GEO)" are parameters of a lognormal least squares fit to the resulting DELFIC size-activity assignments. The atmospheric properties used were those of the U. S. Standard Atmosphere for spring or fall at mid-latitudes (Atmosphere ID = MIDLSF). The winds used were those measured at Washington, DC, on October 3, 1968 (Table II-2). Each figure is identified by a code derived from the wind profile, yield, and size distribution. The wind information shows date and location; "03W" means October 3, 1968, at Washington, DC. Yields are indicated in kilotons, with a trailing "S" for surface burst. The DELFIC default size distribution is "DEF"; the WSEG-10, SIDAC, or RAND is "WSEG"; the others are identified on the basis of the particle size-frequency median, for example, "22P7" for 22.7 μm. Thus, "03W1000S22P7", indicates a 1000 KT surface burst calculation, using winds observed on October 3, 1968, at Washington, DC, and employing the size distribution having a median of 22.7 μm.

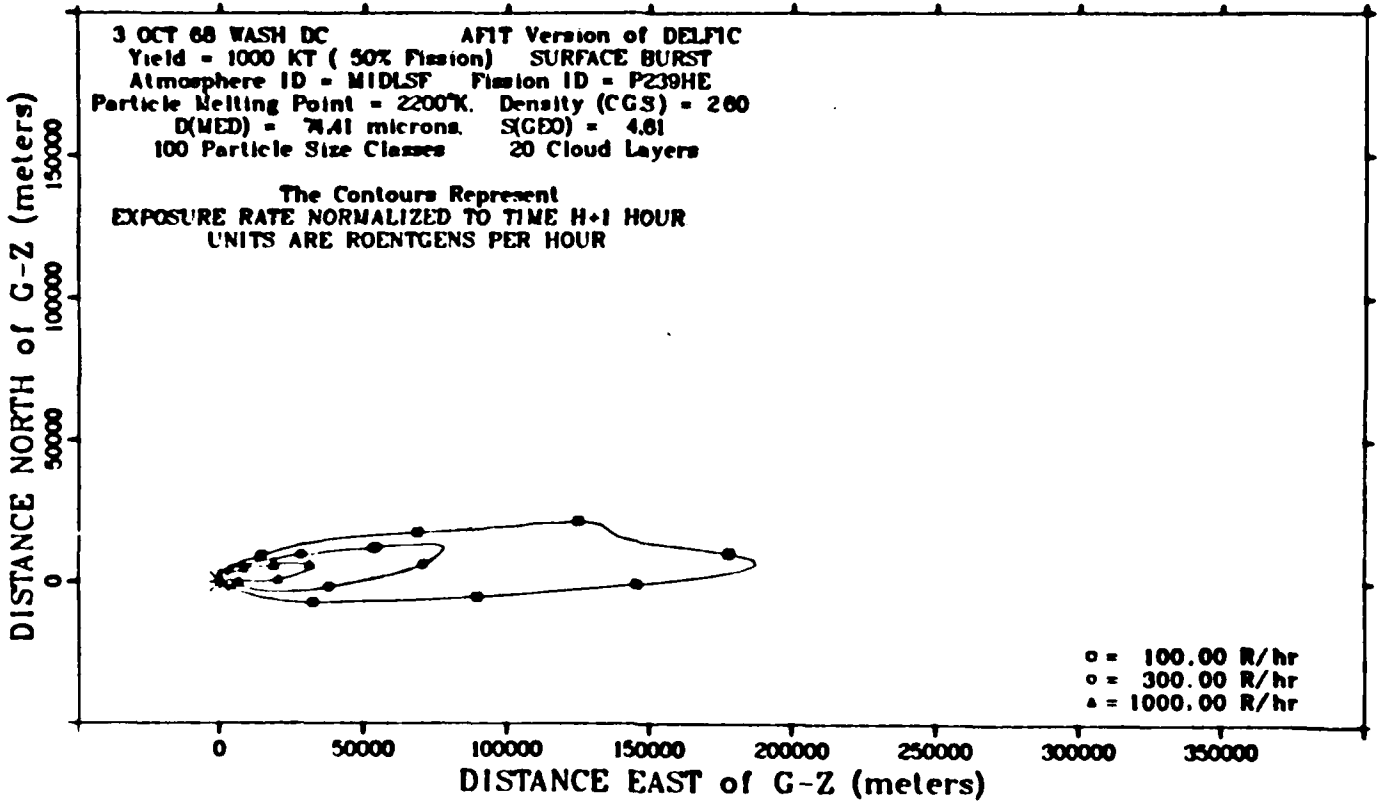

Figure A-1 Fallout Contours for 03W1000SDEF

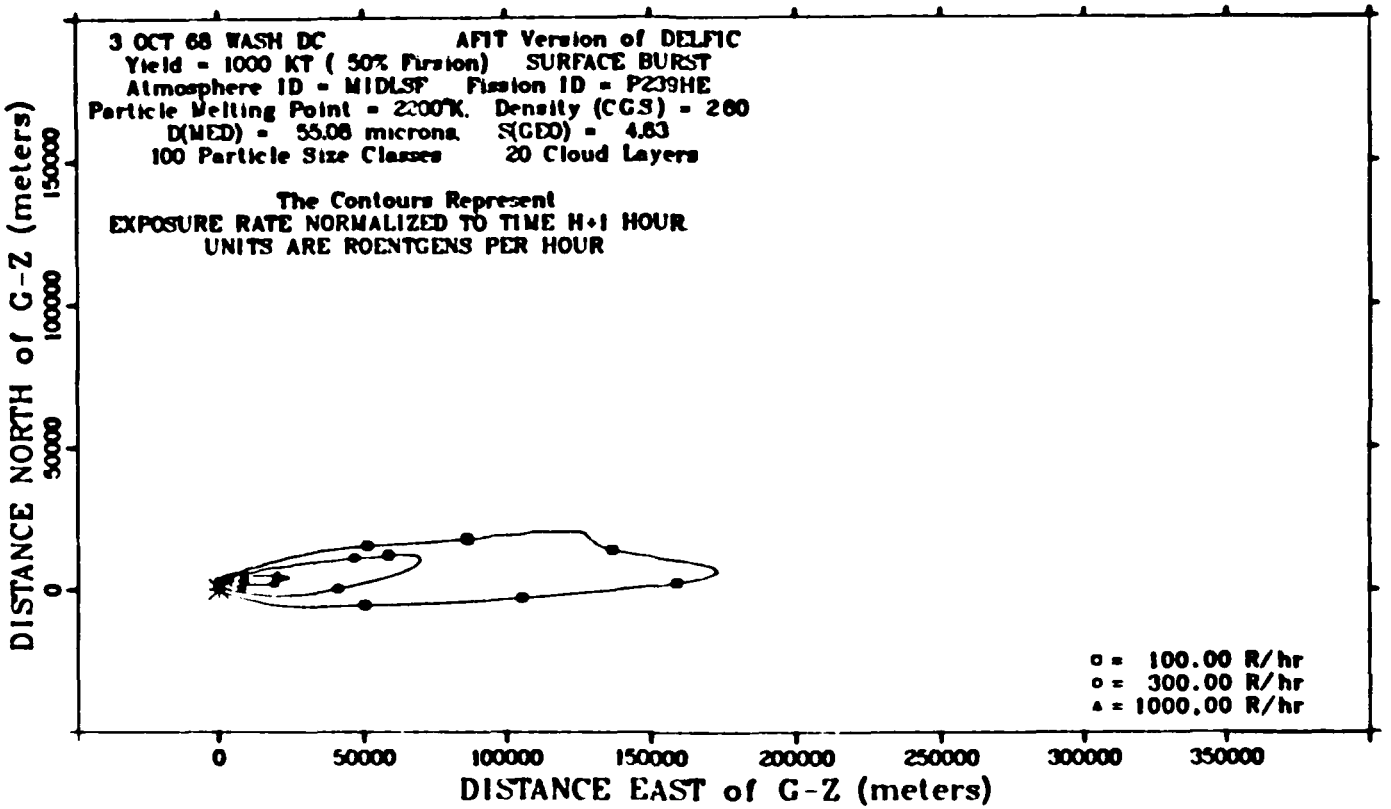

Figure A-2 Fallout Contours for 03W1000SP314

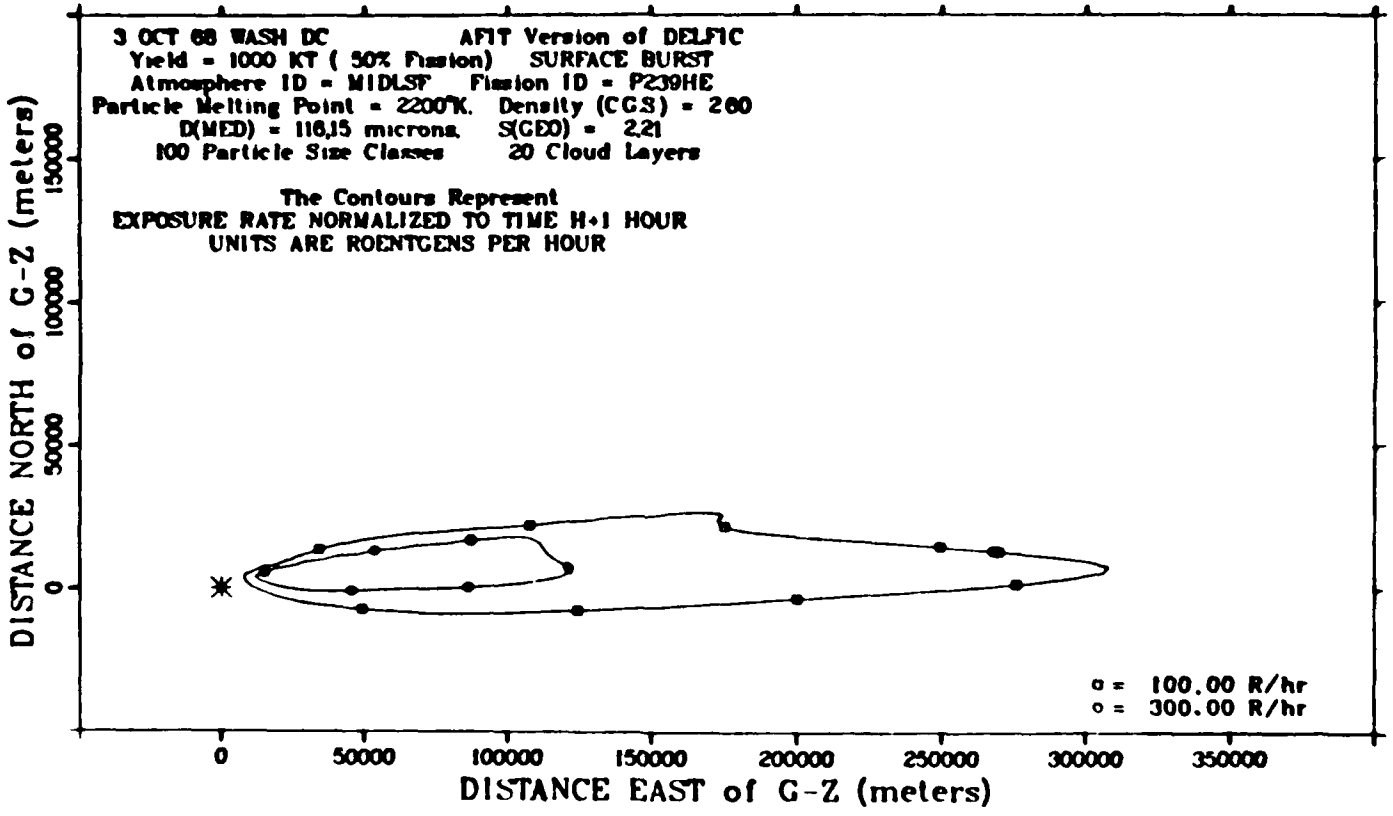

Figure A-3 Fallout Contours for 03W1000S22P7

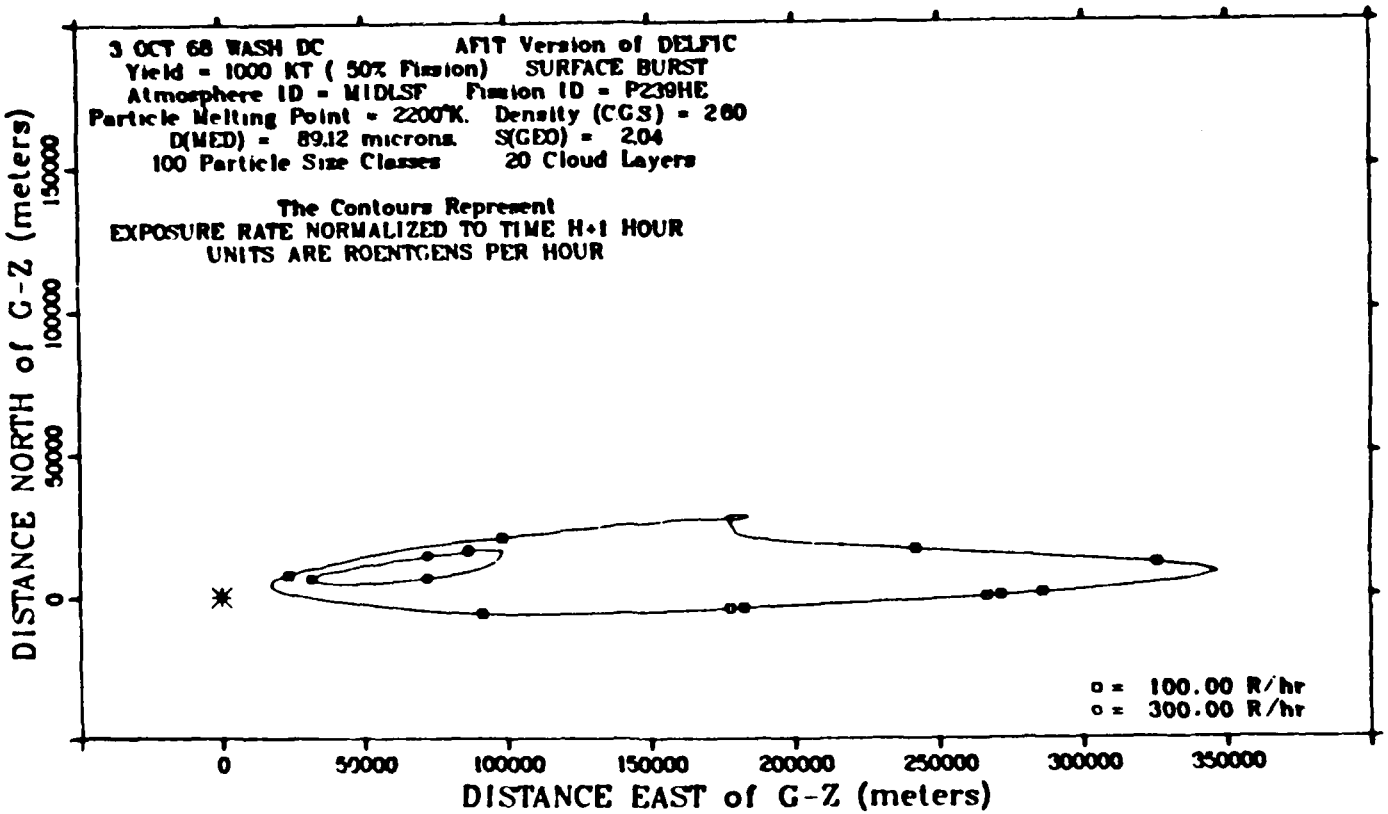

Figure A-4 Fallout Contours for 03W1000SWSEG

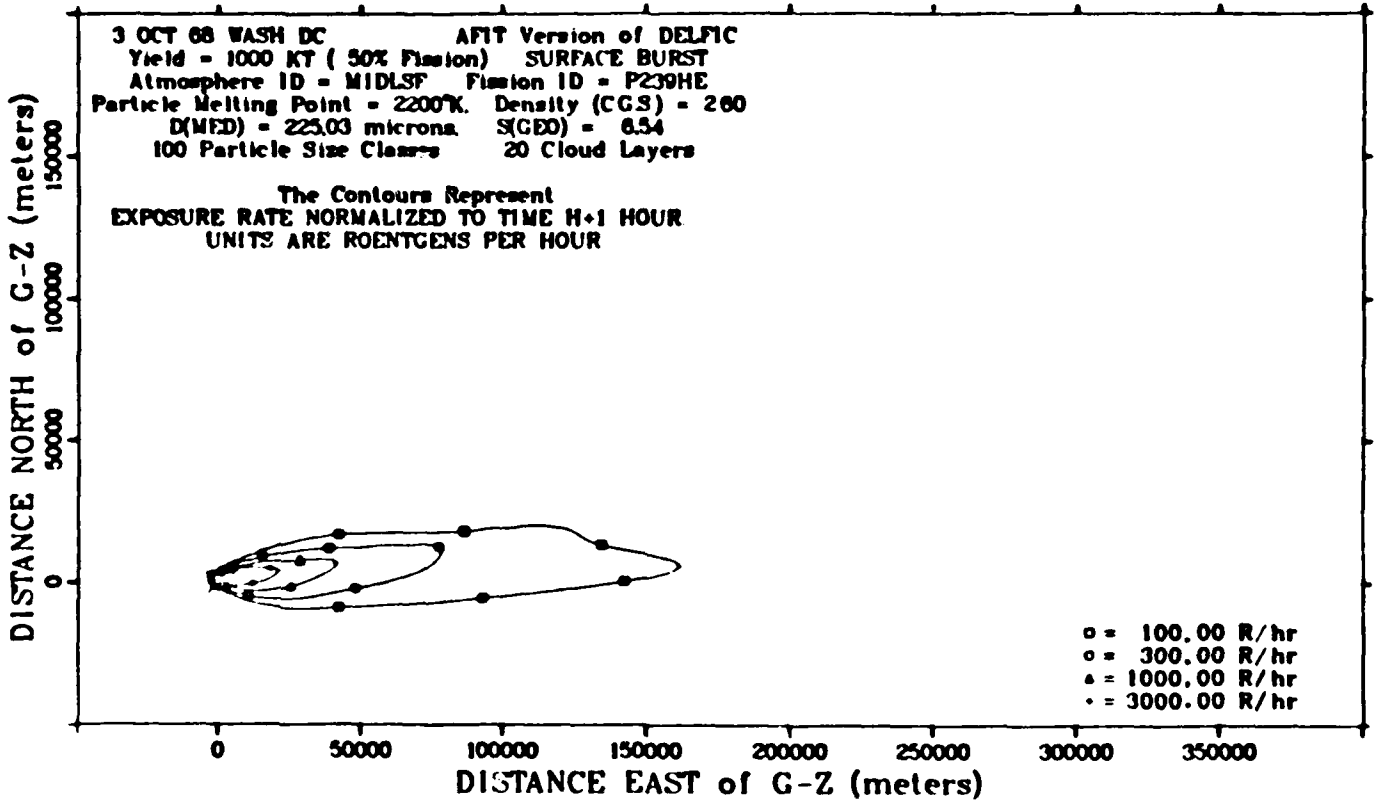

Figure A-5 Fallout Contours for 03W1000SP0849

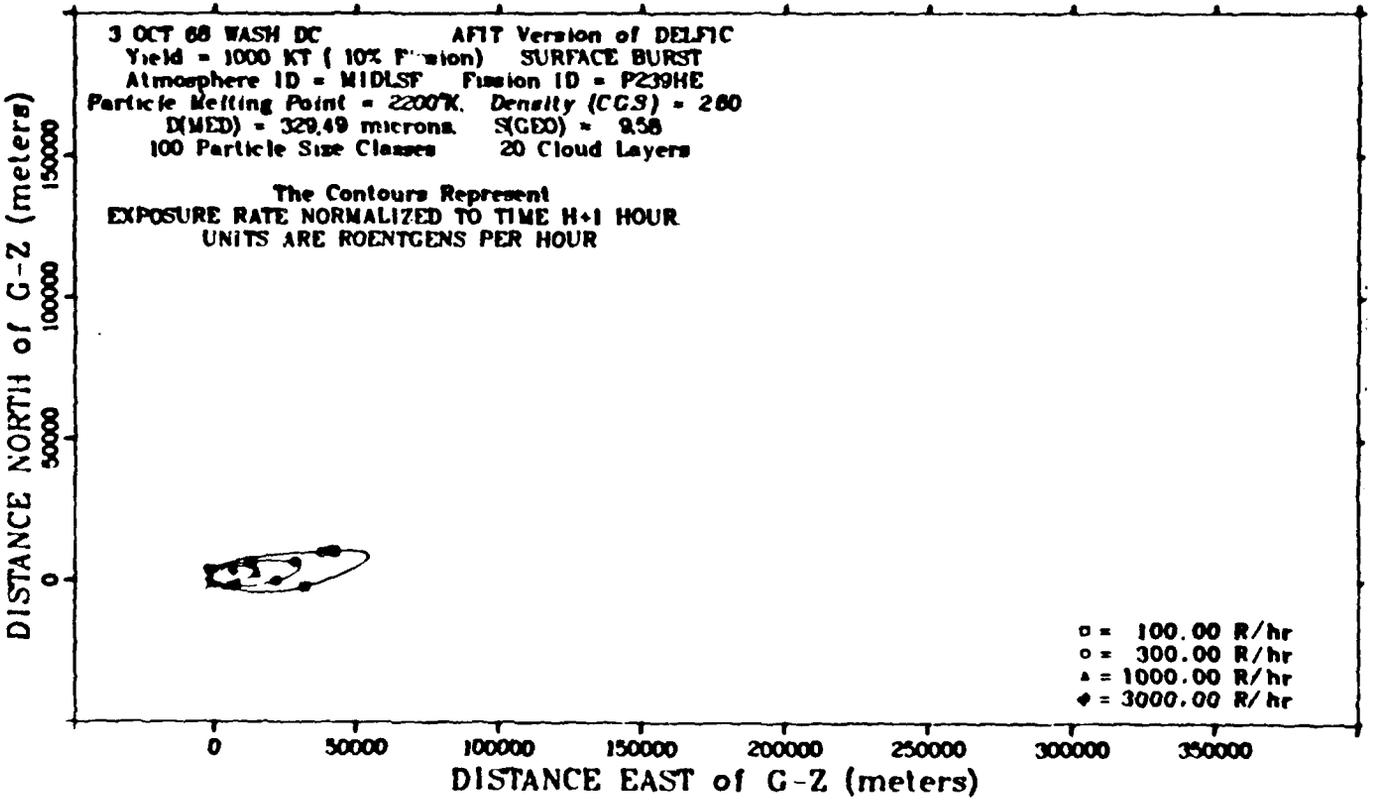

Figure A-6 Fallout Contours for 03W1000SP00556

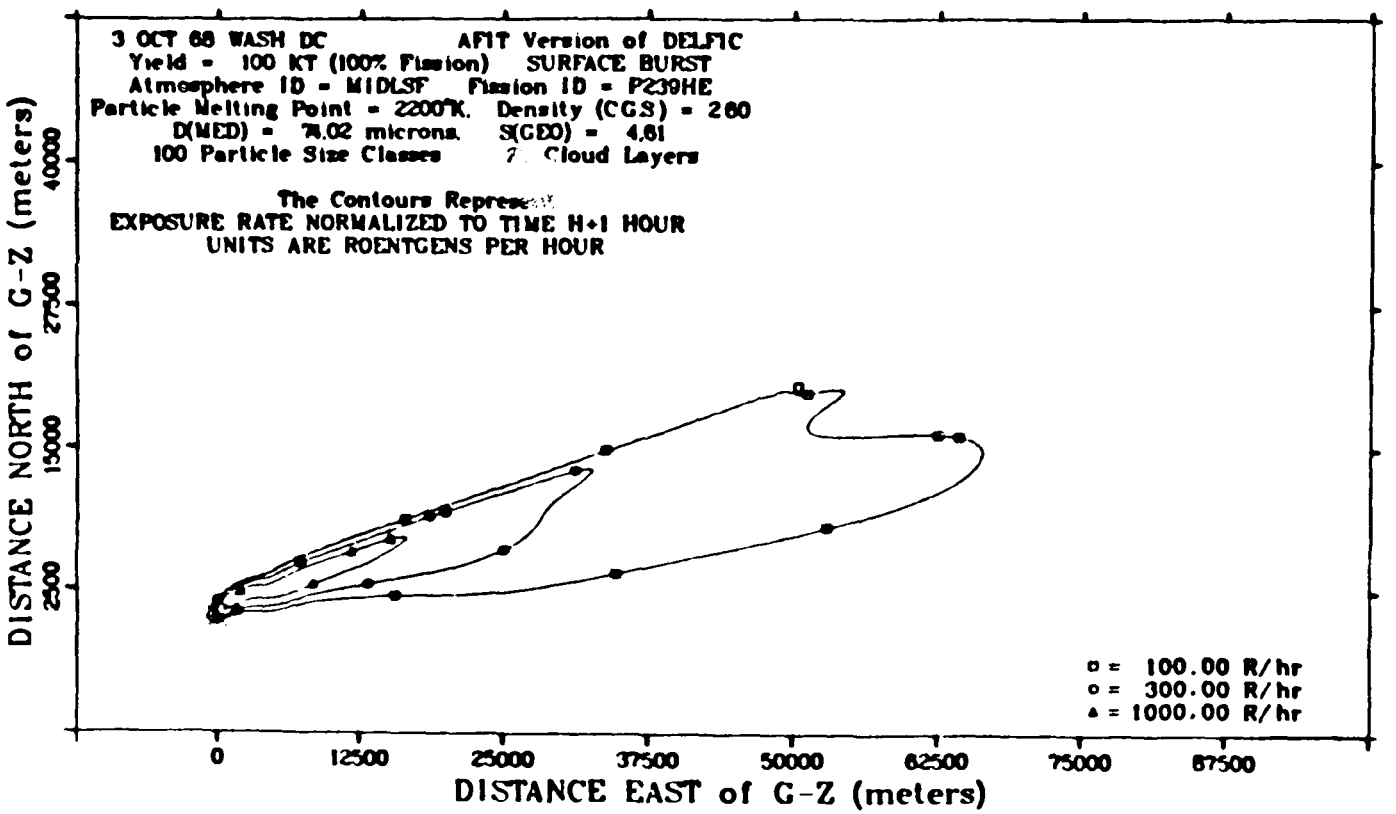

Figure A-7 Fallout Contours for 03W100SDEF

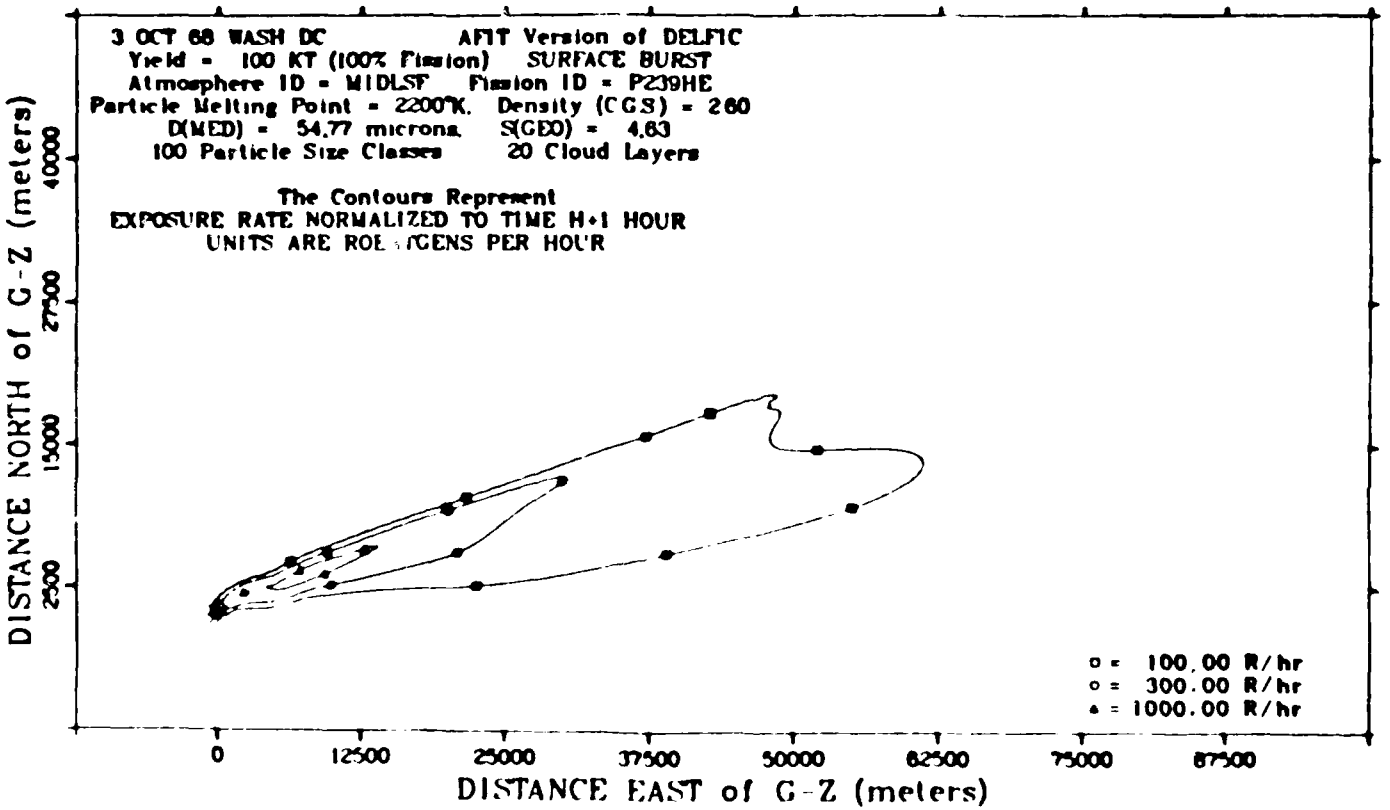

Figure A-8 Fallout Contours for 03W100SP314

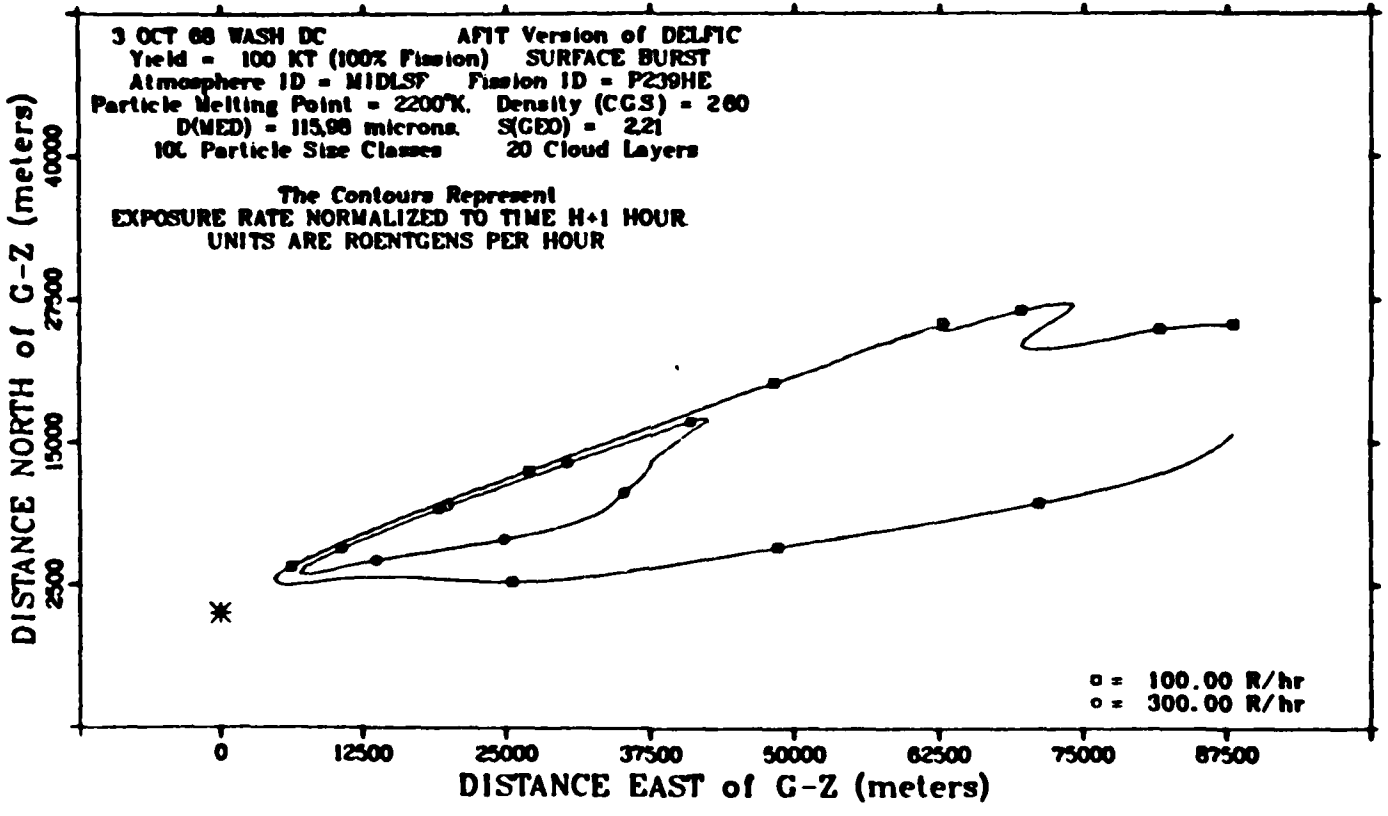

Figure A-9 Fallout Contours for 03W100S22P7

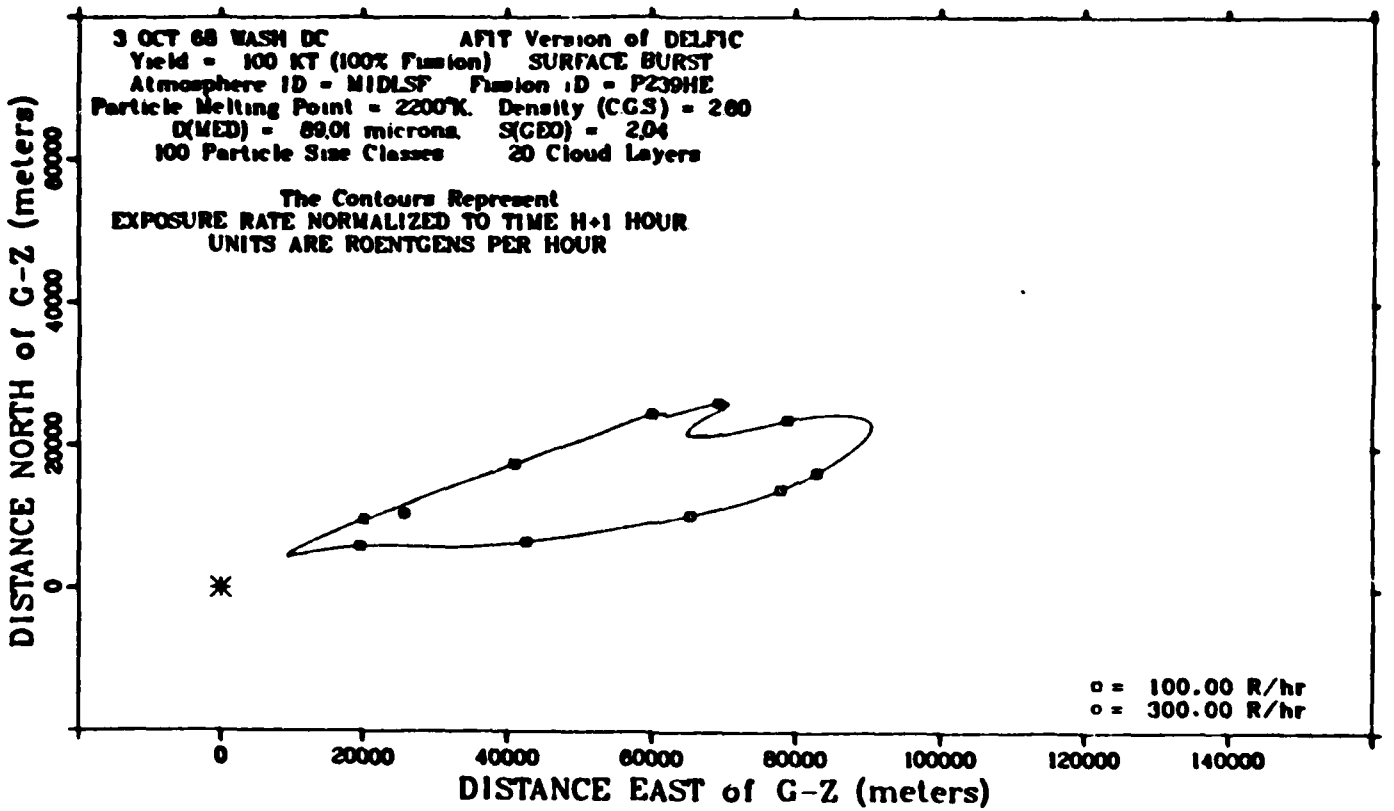

Figure A-10 Fallout Contours for 03W100SWSEG

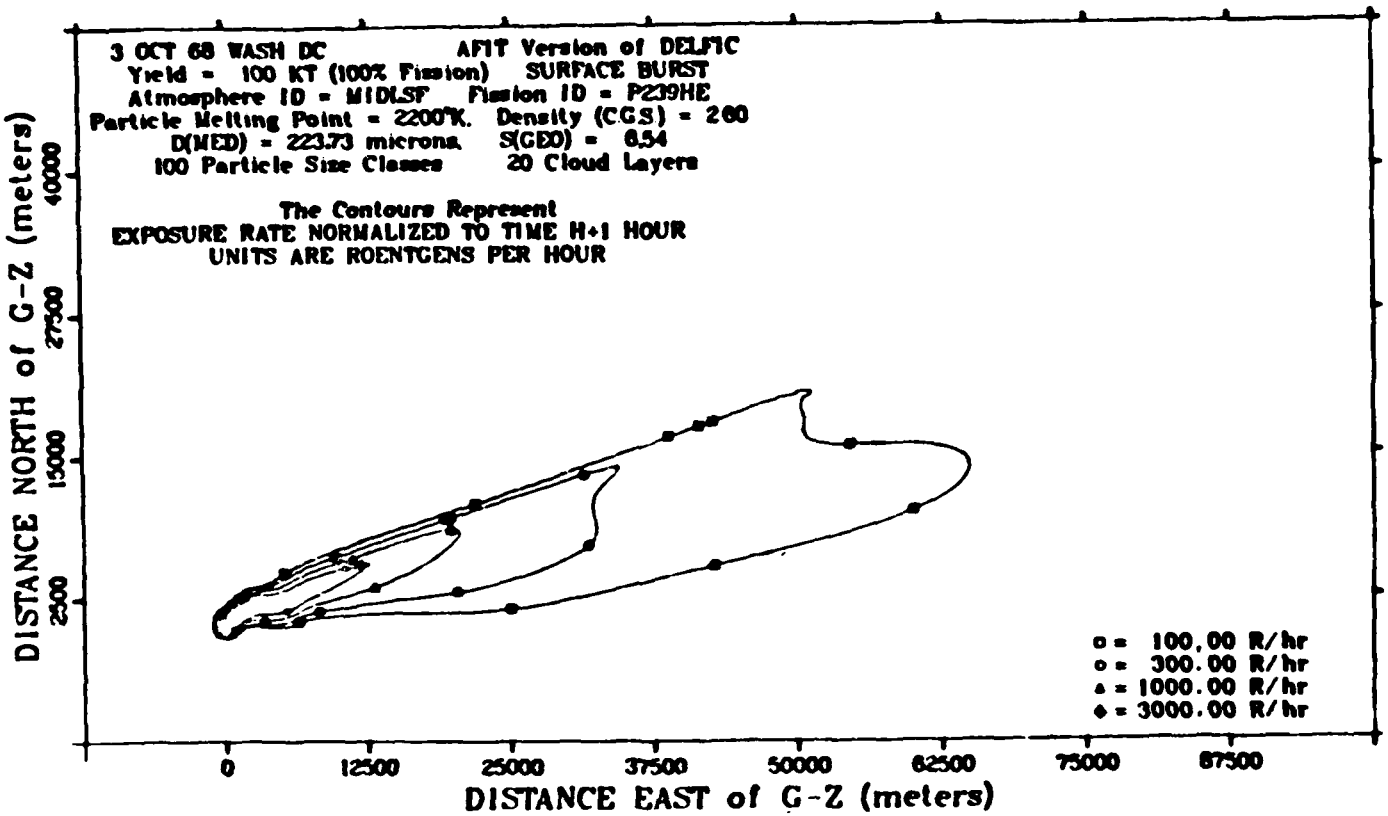

Figure A-11 Fallout Contours for 03W100SP0849

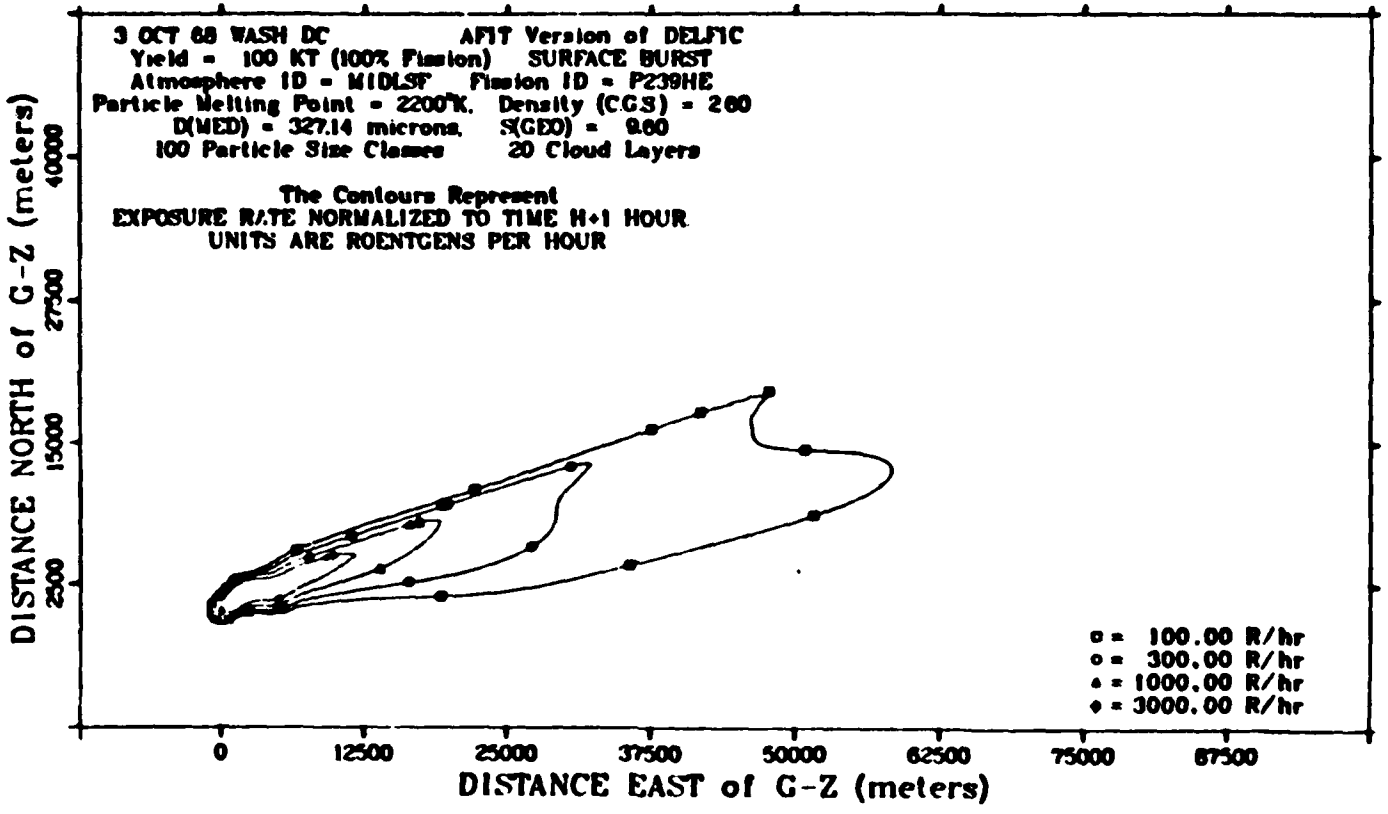

Figure A-12 Fallout Contours for 03W100SP00556

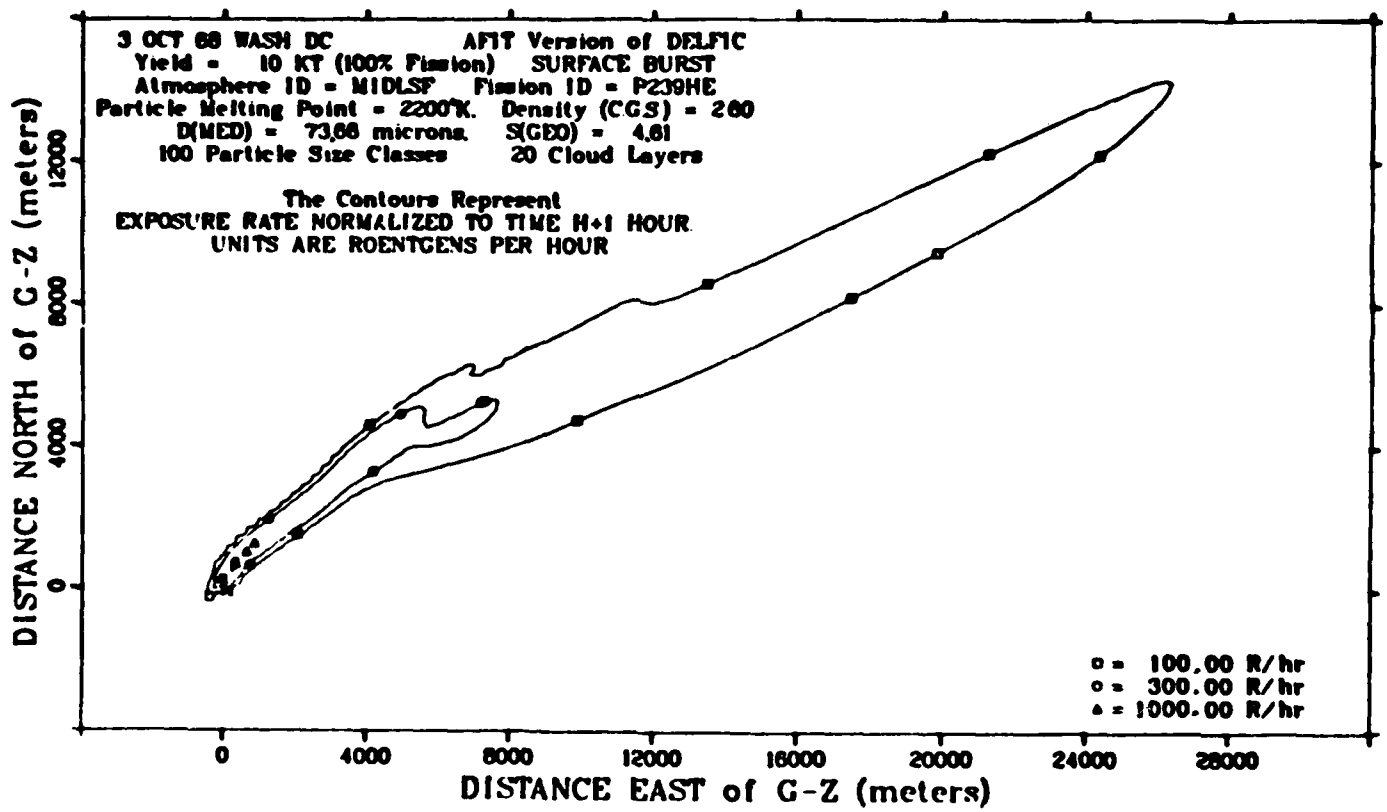

Figure A-13 Fallout Contours for 03W10SDEF

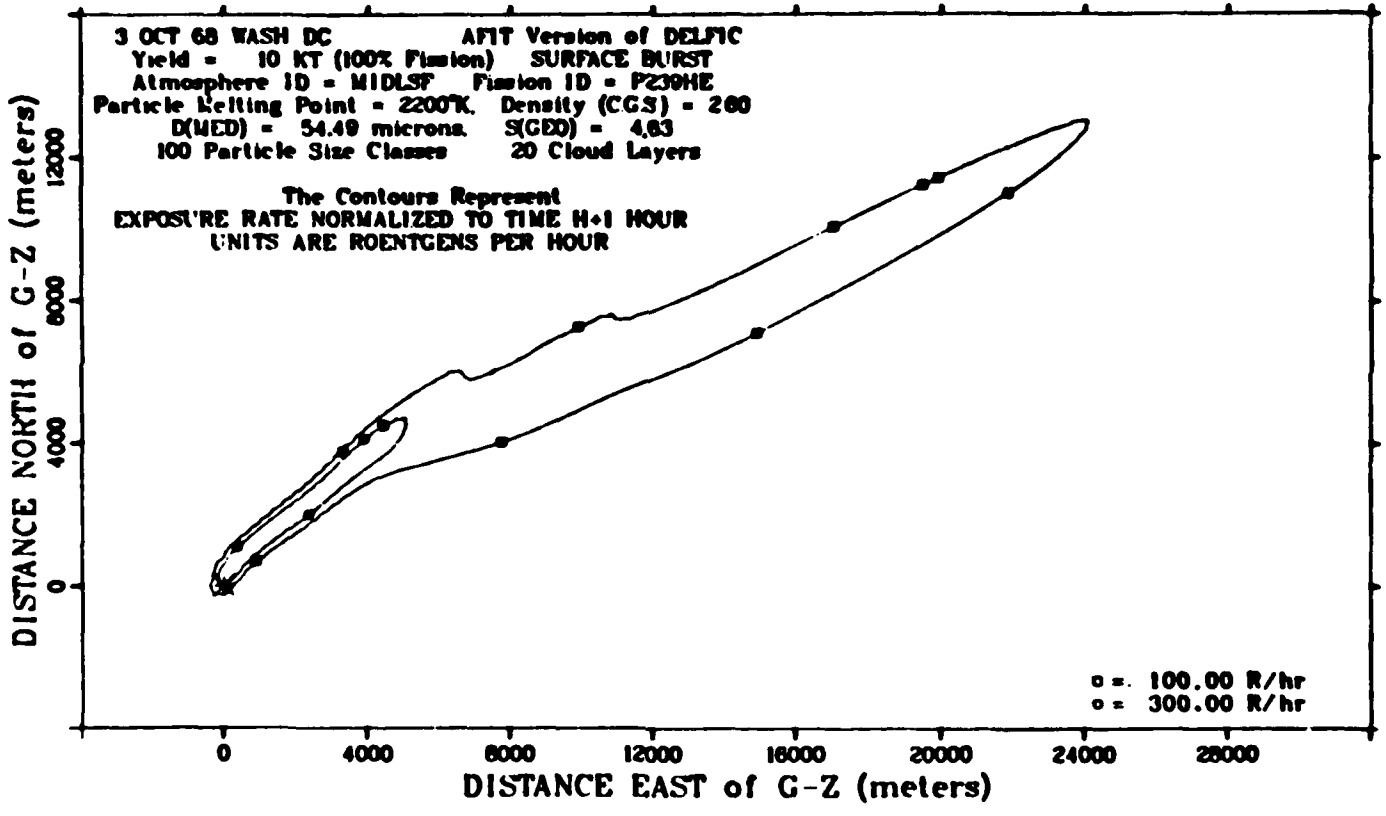

Figure A-14 Fallout Contours for 03W10SP314

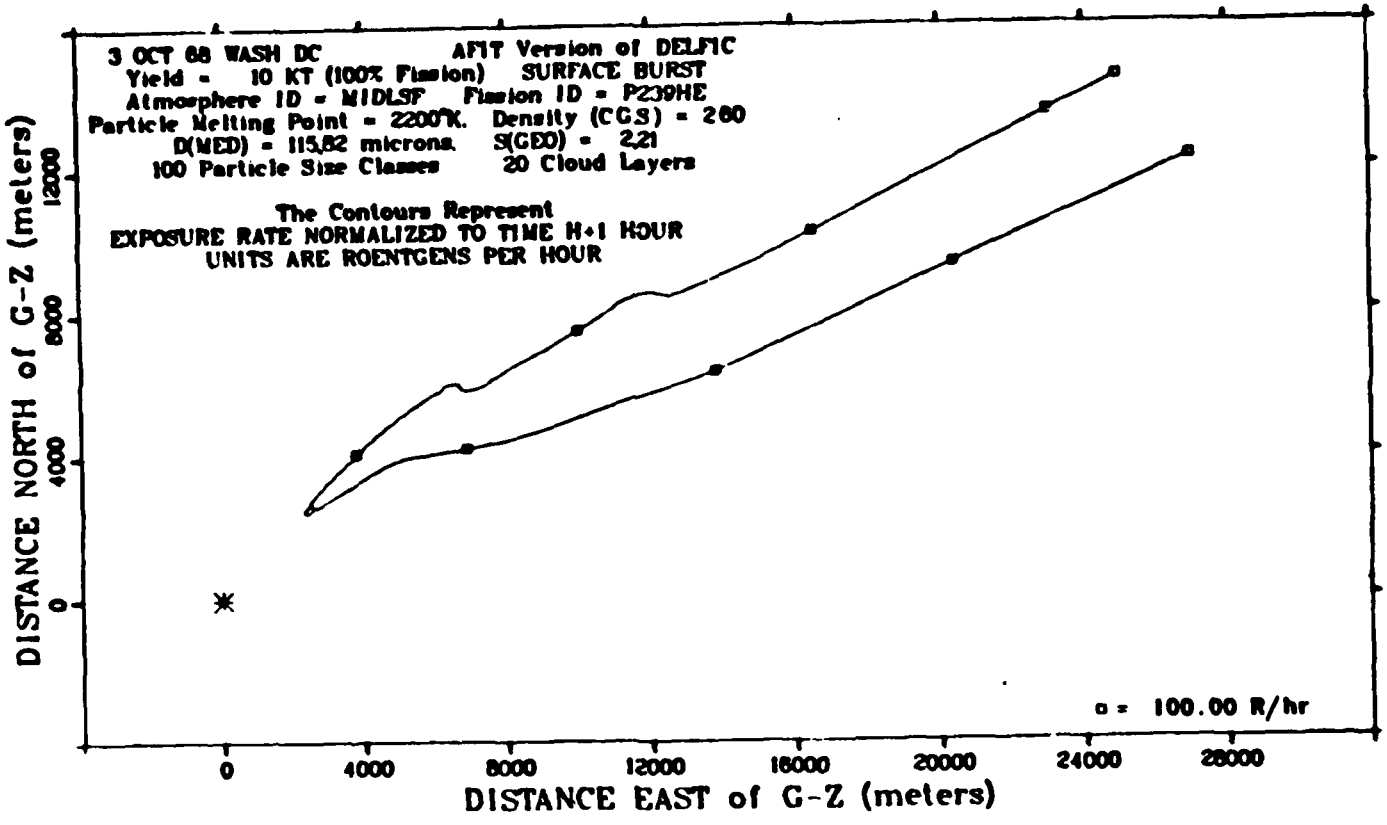

Figure A-15 Fallout Contours for 03W10S22P7

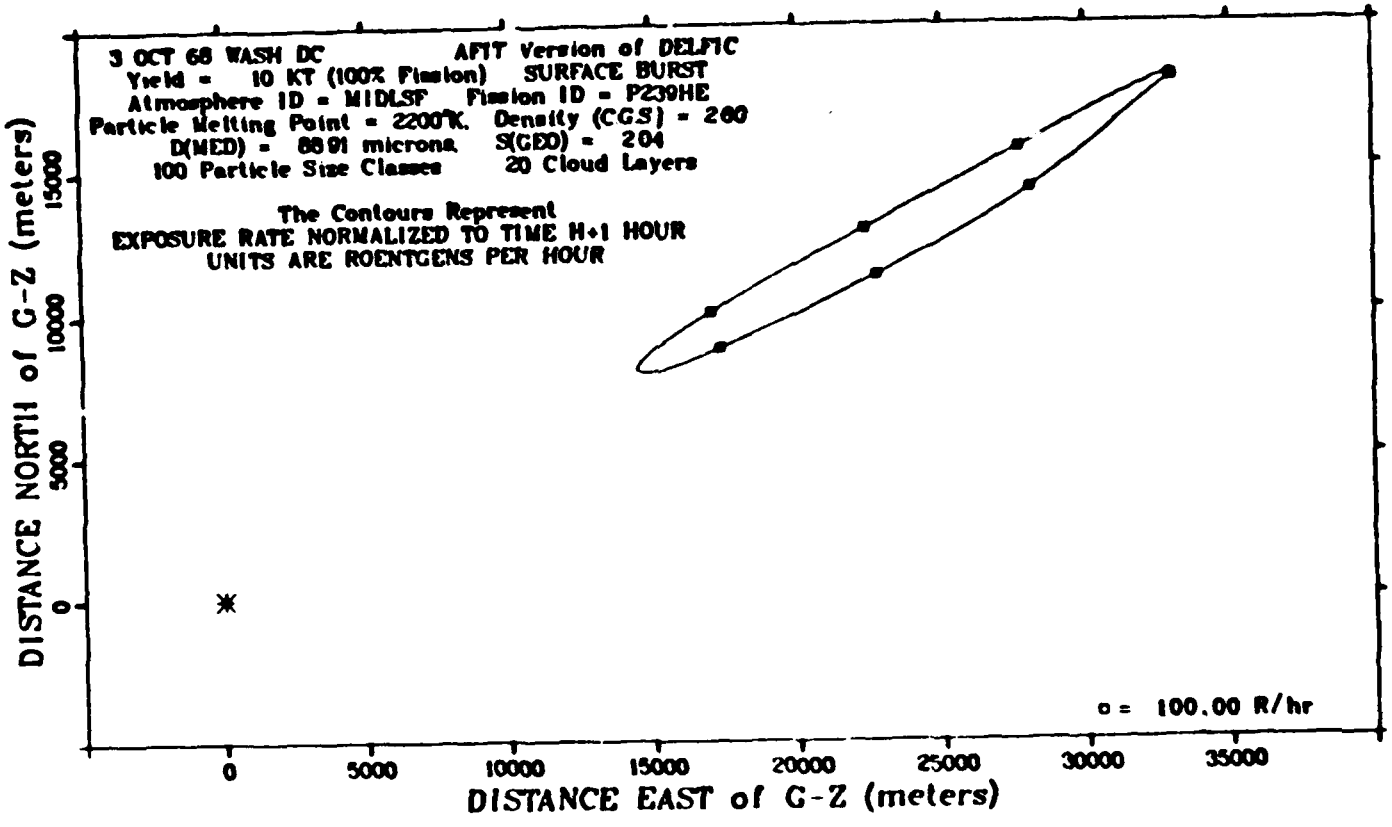

Figure A-16 Fallout Contours for 03W10SWSEG

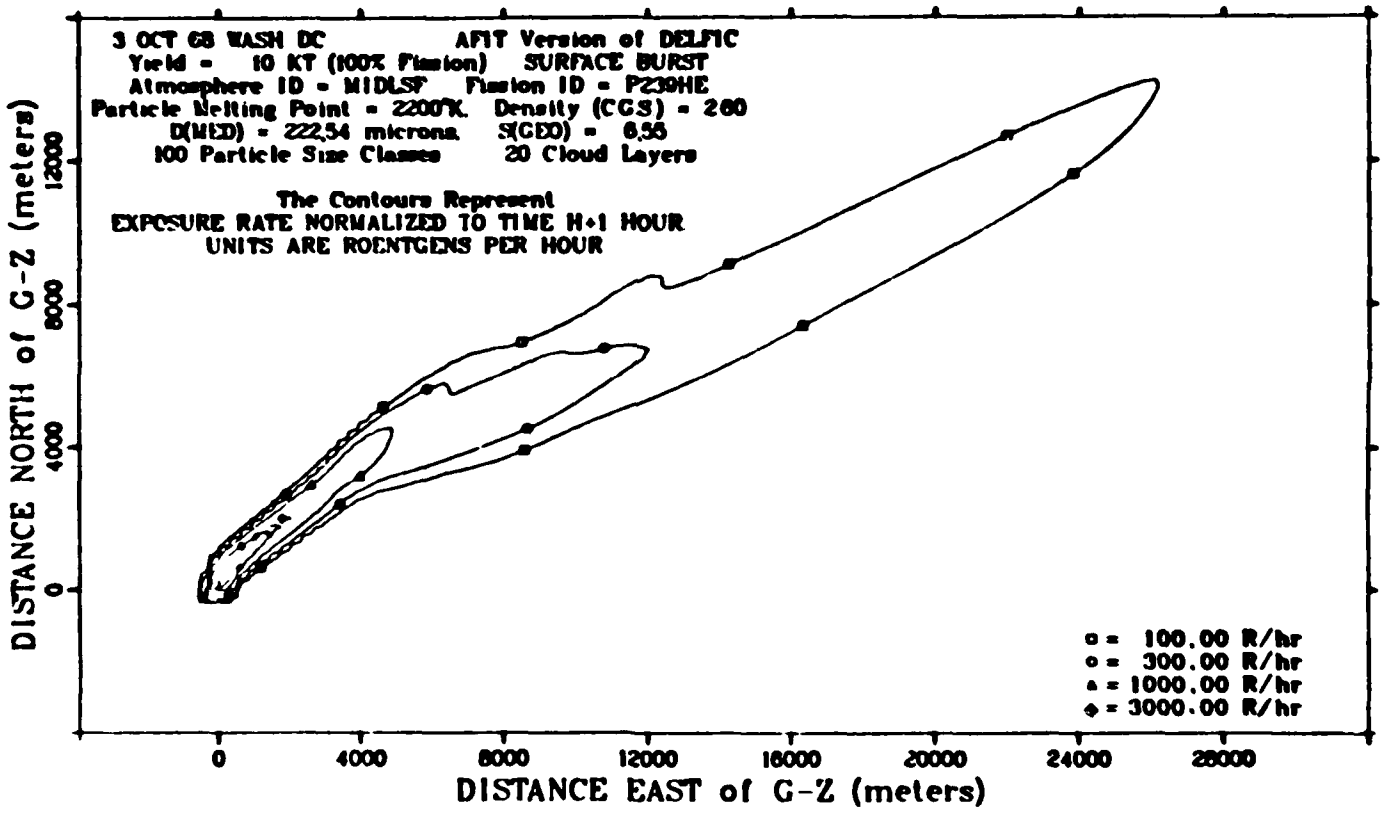

Figure A-17 Fallout Contours for 03W10SP0849

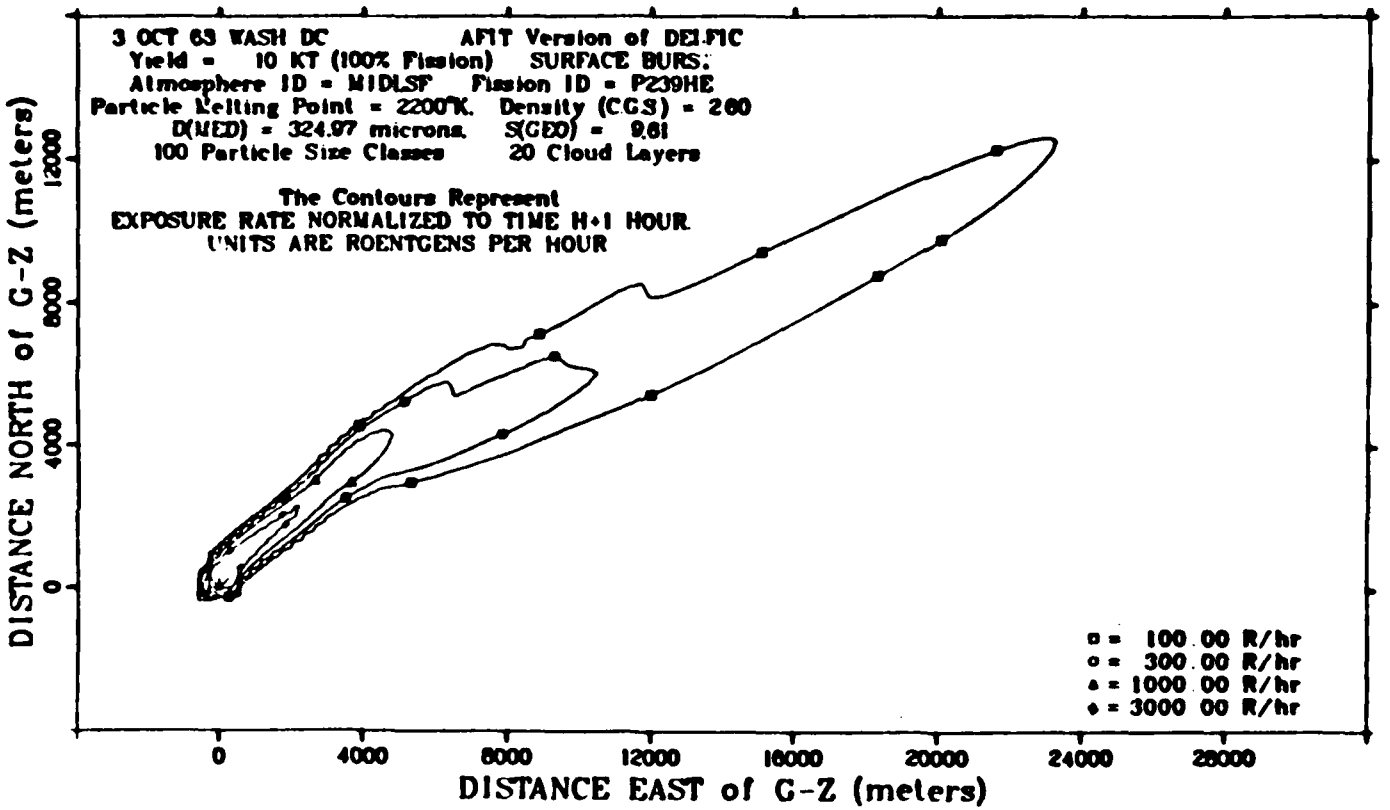

Figure A-18 Fallout Contours for 03W10SP00556

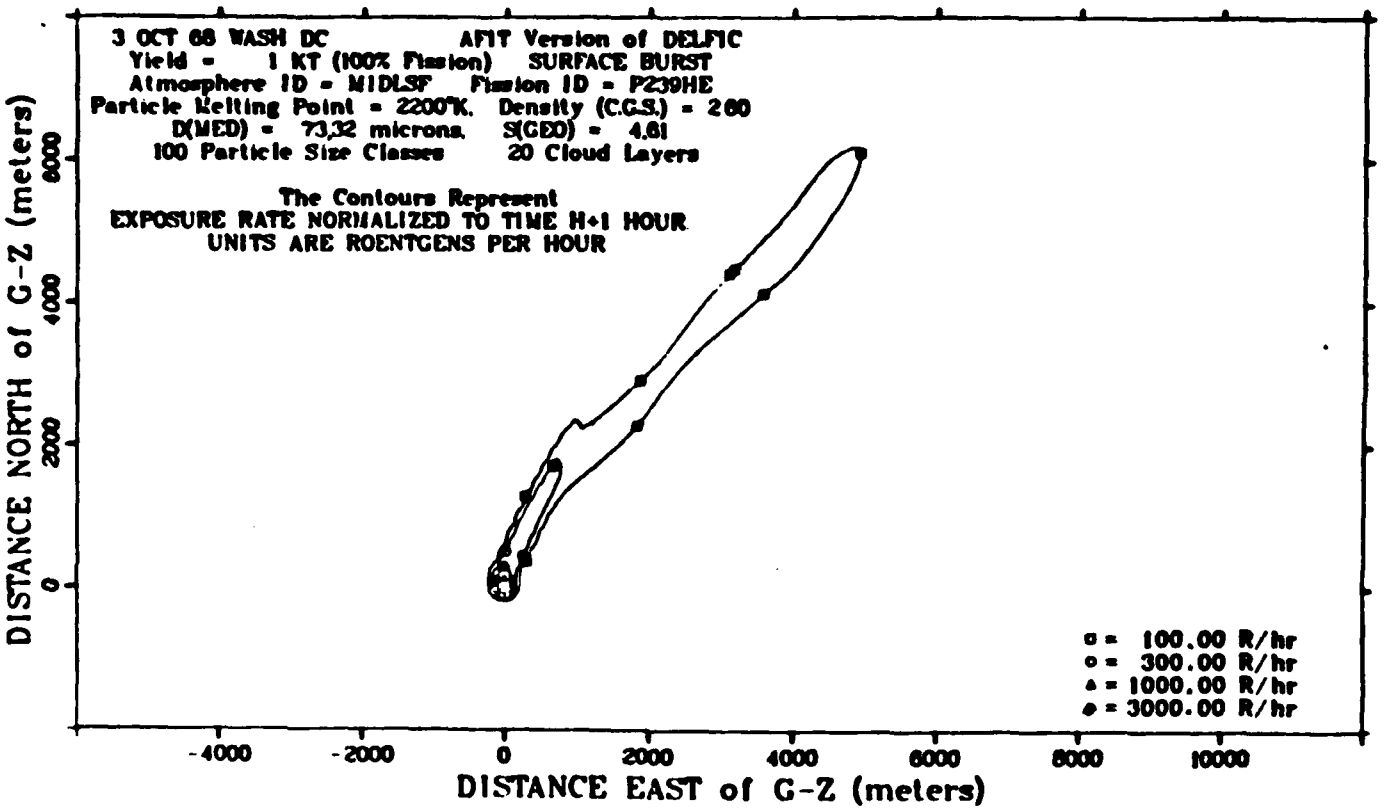

Figure A-19 Fallout Contours for 03WISDEF

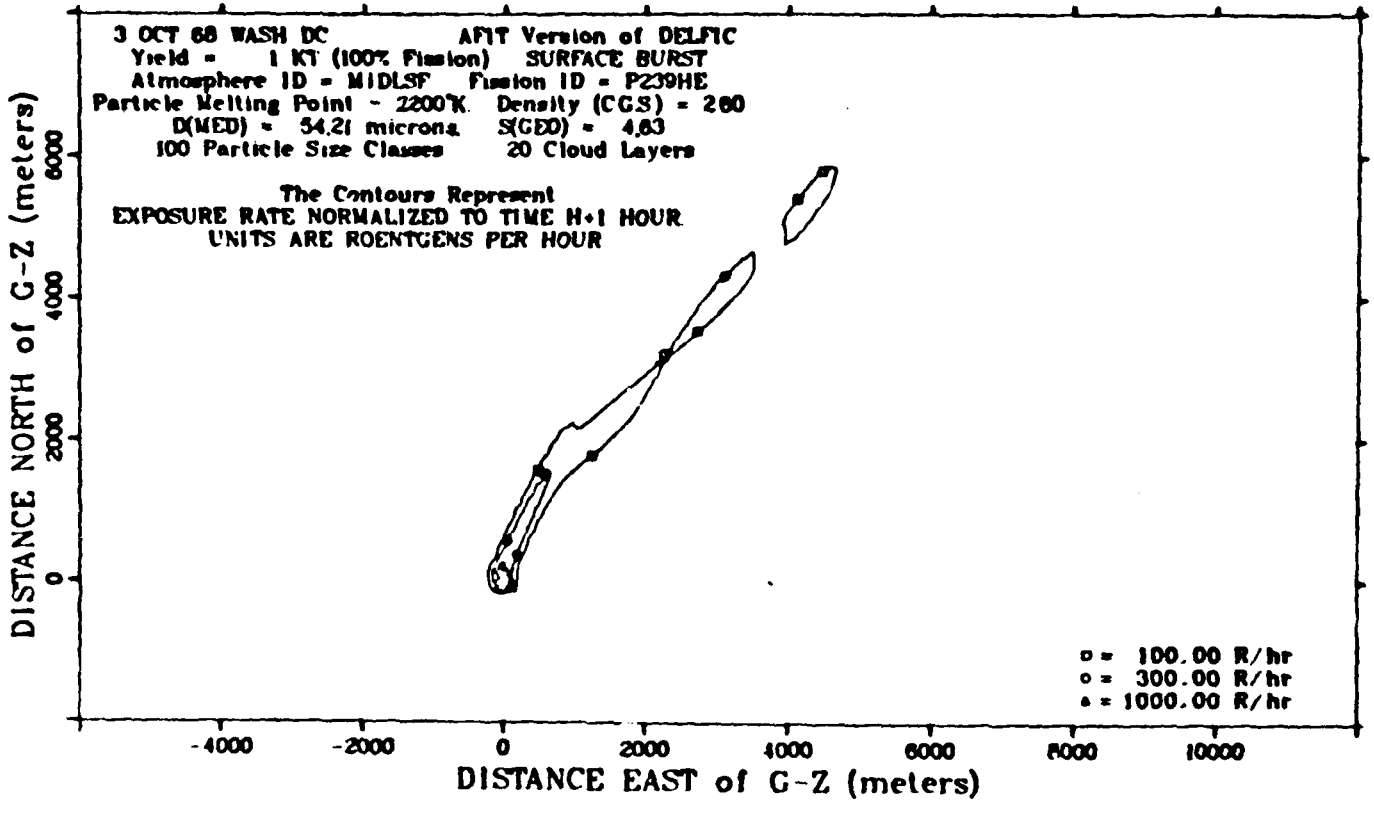

Figure A-20 Fallout Contours for 03WISP314

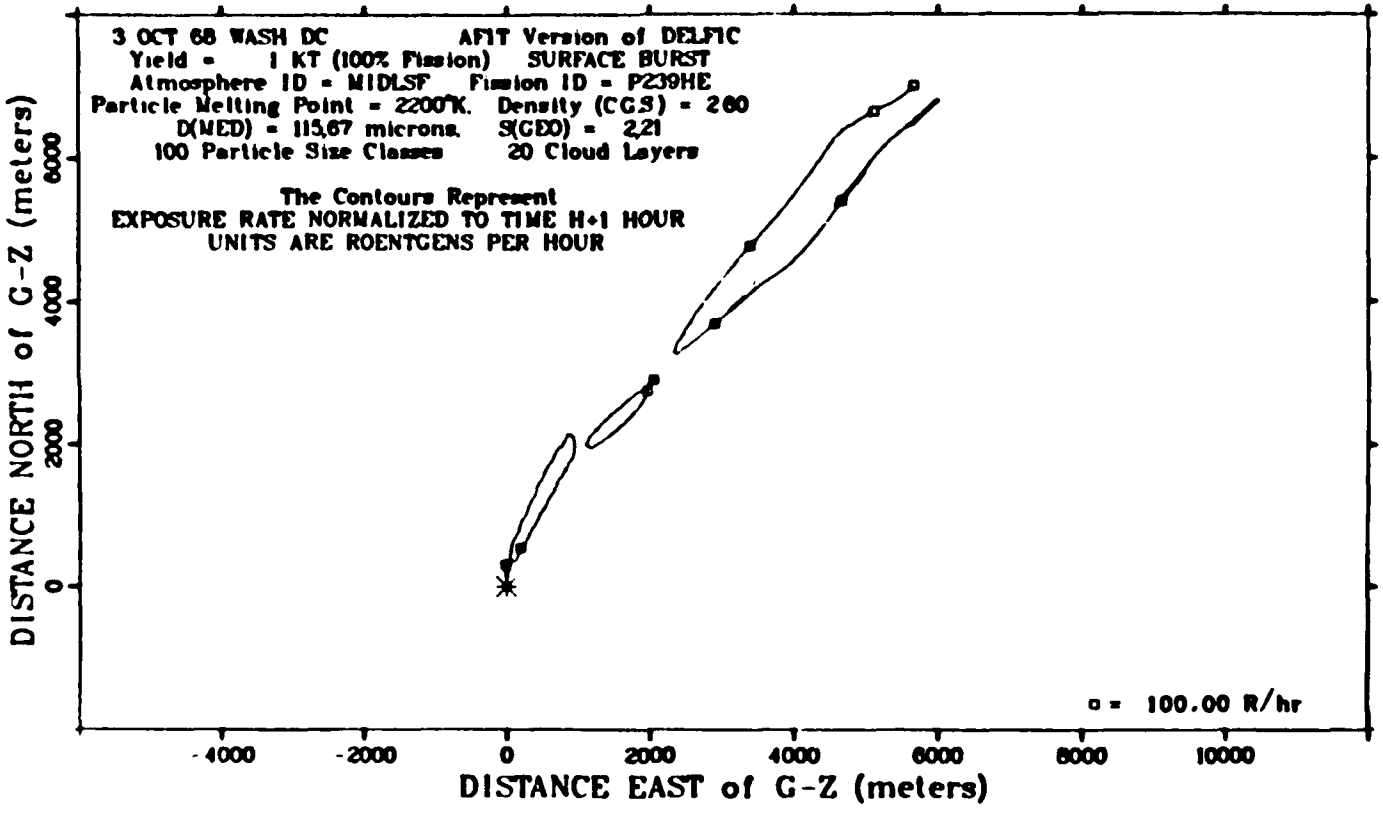

Figure A-21 Fallout Contours for 03W1S22P7

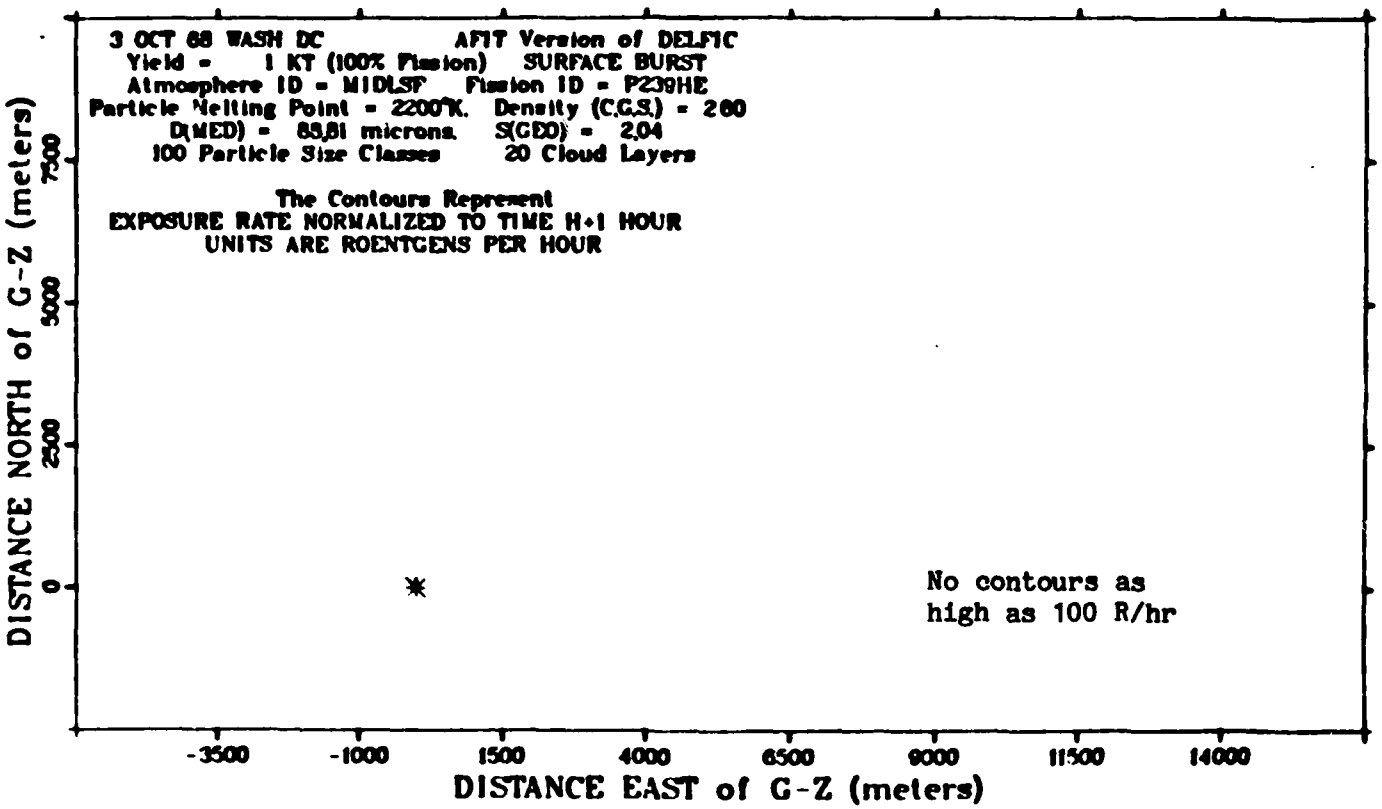

Figure A-22 Fallout Contours for 03W1SWSEG

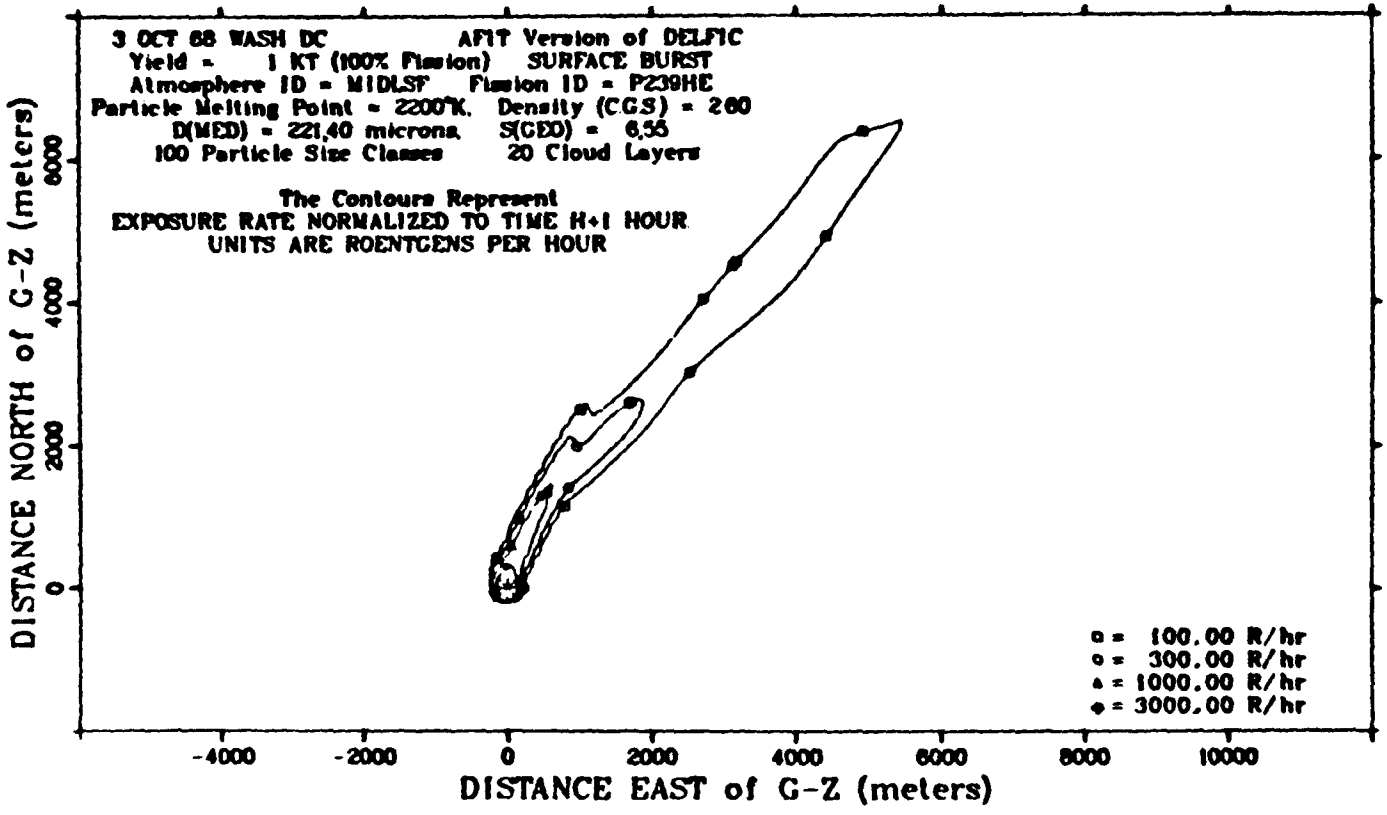

Figure A-23 Fallout Contours for 03WISP0849

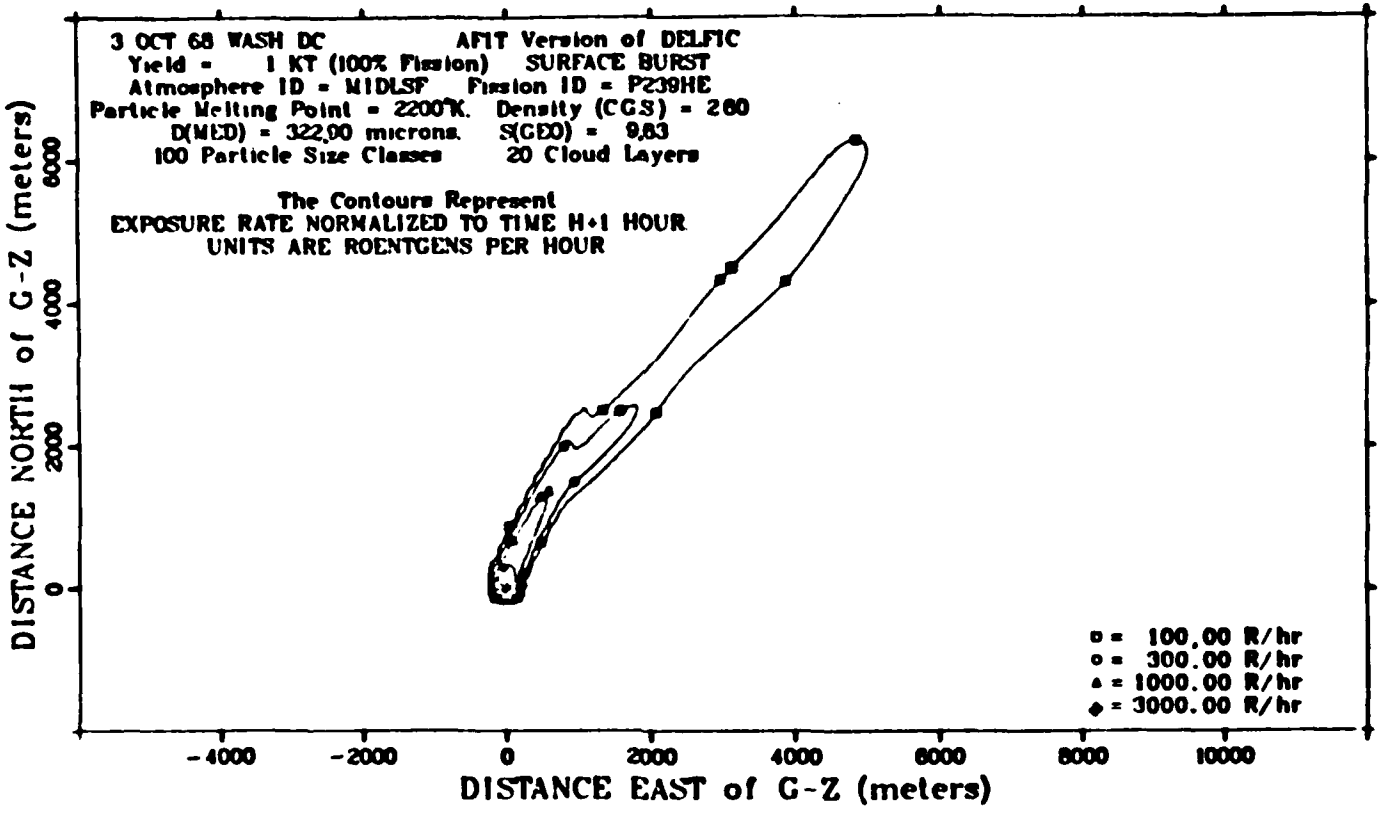

Figure A-24 Fallout Contours for 03W1SP00558

Appendix B

Particle Fall Rate Expansion Coefficients

Table B-1 Particle Fall Rate Expansion Coefficients
(r in meters, t in hours, z in kilometers)

z	C(1)	C(2)	C(3)	C(4)	C(5)	C(6)	C(7)
0.2	-.42494E-15	0.37874E-12	-.99764E-10	0.23375E-07	0.83123E-06	-.17840E-05	0.13110E-04
0.4	-.13323E-13	0.59598E-11	-.78875E-09	0.92734E-07	0.16550E-05	-.17823E-05	0.18523E-04
0.6	-.99099E-13	0.29668E-10	-.26305E-08	0.20692E-06	0.24713E-05	-.17806E-05	0.22664E-04
0.8	-.40897E-12	0.92185E-10	-.61605E-08	0.36479E-06	0.32801E-05	-.17789E-05	0.26144E-04
1.0	-.12220E-11	0.22123E-09	-.11887E-07	0.56516E-06	0.40812E-05	-.17771E-05	0.29202E-04
1.2	-.29772E-11	0.45092E-09	-.20291E-07	0.80695E-06	0.48748E-05	-.17754E-05	0.31958E-04
1.4	-.63023E-11	0.82136E-09	-.31838E-07	0.10892E-05	0.56610E-05	-.17744E-05	0.34484E-04
1.6	-.12036E-10	0.13778E-08	-.46963E-07	0.14107E-05	0.64397E-05	-.17740E-05	0.36829E-04
1.8	-.21240E-10	0.21698E-08	-.66068E-07	0.17705E-05	0.72111E-05	-.17732E-05	0.39024E-04
2.0	-.35220E-10	0.32509E-08	-.89534E-07	0.21673E-05	0.79750E-05	-.17721E-05	0.41093E-04
2.2	-.55534E-10	0.46784E-08	-.11772E-06	0.26002E-05	0.87317E-05	-.17709E-05	0.43055E-04
2.4	-.84005E-10	0.65129E-08	-.15098E-06	0.30682E-05	0.94814E-05	-.17695E-05	0.44924E-04
2.6	-.12271E-09	0.88171E-08	-.18962E-06	0.35702E-05	0.10224E-04	-.17681E-05	0.46711E-04
2.8	-.17400E-09	0.11656E-07	-.23394E-06	0.41052E-05	0.10959E-04	-.17664E-05	0.48425E-04
3.0	-.24045E-09	0.15094E-07	-.28419E-06	0.46722E-05	0.11688E-04	-.17647E-05	0.50073E-04
3.2	-.32495E-09	0.19202E-07	-.34063E-06	0.52701E-05	0.12409E-04	-.17630E-05	0.51662E-04
3.4	-.43064E-09	0.24047E-07	-.40353E-06	0.58983E-05	0.13123E-04	-.17611E-05	0.53196E-04
3.6	-.56087E-09	0.29700E-07	-.47308E-06	0.65556E-05	0.13831E-04	-.17592E-05	0.54681E-04
3.8	-.71923E-09	0.36229E-07	-.54947E-06	0.72411E-05	0.14531E-04	-.17572E-05	0.56121E-04
4.0	-.90951E-09	0.43702E-07	-.63286E-06	0.79537E-05	0.15225E-04	-.17552E-05	0.57518E-04
4.2	-.11358E-08	0.52189E-07	-.72345E-06	0.86927E-05	0.15912E-04	-.17531E-05	0.58875E-04
4.4	-.14023E-08	0.61762E-07	-.82138E-06	0.94573E-05	0.16593E-04	-.17510E-05	0.60196E-04
4.6	-.17135E-08	0.72488E-07	-.92678E-06	0.10247E-04	0.17266E-04	-.17489E-05	0.61483E-04
4.8	-.20740E-08	0.84430E-07	-.10398E-05	0.11060E-04	0.17934E-04	-.17467E-05	0.62738E-04

z	C(1)	C(2)	C(3)	C(4)	C(5)	C(6)	C(7)
5.0	-.24884E-08	0.97653E-07	-.11604E-05	0.11895E-04	0.18594E-04	-.17444E-05	0.63962E-04
5.2	-.29616E-08	0.11222E-06	-.12887E-05	0.12753E-04	0.19248E-04	-.17422E-05	0.65158E-04
5.4	-.34988E-08	0.12820E-06	-.14250E-05	0.13632E-04	0.19896E-04	-.17399E-05	0.66327E-04
5.6	-.41051E-08	0.14566E-06	-.15691E-05	0.14532E-04	0.20537E-04	-.17375E-05	0.67470E-04
5.8	-.47859E-08	0.16464E-06	-.17212E-05	0.15452E-04	0.21171E-04	-.17353E-05	0.68588E-04
6.0	-.55464E-08	0.18522E-06	-.18814E-05	0.16390E-04	0.21799E-04	-.17331E-05	0.69684E-04
6.2	-.63918E-08	0.20744E-06	-.20495E-05	0.17347E-04	0.22420E-04	-.17310E-05	0.70757E-04
6.4	-.73276E-08	0.23135E-06	-.22256E-05	0.18321E-04	0.23035E-04	-.17287E-05	0.71809E-04
6.6	-.83591E-08	0.25700E-06	-.24098E-05	0.19312E-04	0.23645E-04	-.17264E-05	0.72840E-04
6.8	-.94915E-08	0.28444E-06	-.26018E-05	0.20318E-04	0.24248E-04	-.17241E-05	0.73852E-04
7.0	-.10730E-07	0.31370E-06	-.28018E-05	0.21340E-04	0.24844E-04	-.17217E-05	0.74845E-04
7.2	-.12080E-07	0.34482E-06	-.30096E-05	0.22375E-04	0.25435E-04	-.17192E-05	0.75819E-04
7.4	-.13547E-07	0.37786E-06	-.32254E-05	0.23425E-04	0.26020E-04	-.17167E-05	0.76777E-04
7.6	-.15136E-07	0.41285E-06	-.34489E-05	0.24487E-04	0.26600E-04	-.17141E-05	0.77718E-04
7.8	-.16852E-07	0.44981E-06	-.36801E-05	0.25562E-04	0.27173E-04	-.17115E-05	0.78642E-04
8.0	-.18700E-07	0.48876E-06	-.39189E-05	0.26648E-04	0.27741E-04	-.17088E-05	0.79551E-04
8.2	-.20685E-07	0.52973E-06	-.41652E-05	0.27745E-04	0.28302E-04	-.17061E-05	0.80445E-04
8.4	-.22812E-07	0.57277E-06	-.44190E-05	0.28852E-04	0.28859E-04	-.17034E-05	0.81324E-04
8.6	-.25085E-07	0.61788E-06	-.46802E-05	0.29970E-04	0.29409E-04	-.17006E-05	0.82189E-04
8.8	-.27509E-07	0.66508E-06	-.49486E-05	0.31096E-04	0.29955E-04	-.16977E-05	0.83040E-04
9.0	-.30087E-07	0.71436E-06	-.52241E-05	0.32230E-04	0.30494E-04	-.16948E-05	0.83878E-04
9.2	-.32824E-07	0.76576E-06	-.55066E-05	0.33372E-04	0.31028E-04	-.16918E-05	0.84702E-04
9.4	-.35727E-07	0.81932E-06	-.57962E-05	0.34522E-04	0.31556E-04	-.16889E-05	0.85514E-04
9.6	-.38798E-07	0.87504E-06	-.60928E-05	0.35680E-04	0.32079E-04	-.16859E-05	0.86314E-04
9.8	-.42040E-07	0.93289E-06	-.63960E-05	0.36843E-04	0.32596E-04	-.16829E-05	0.87102E-04
10.0	-.45454E-07	0.99285E-06	-.67056E-05	0.38012E-04	0.33108E-04	-.16799E-05	0.87878E-04
10.2	-.49044E-07	0.10549E-05	-.70214E-05	0.39185E-04	0.33614E-04	-.16768E-05	0.88642E-04
10.4	-.52814E-07	0.11191E-05	-.73434E-05	0.40363E-04	0.34116E-04	-.16736E-05	0.89395E-04
10.6	-.56767E-07	0.11855E-05	-.76715E-05	0.41544E-04	0.34613E-04	-.16704E-05	0.90137E-04
10.8	-.60903E-07	0.12539E-05	-.80053E-05	0.42729E-04	0.35105E-04	-.16672E-05	0.90868E-04

z	C(1)	C(2)	C(3)	C(4)	C(5)	C(6)	C(7)
11.0	-.65224E-07	0.13243E-05	-.83446E-05	0.43916E-04	0.35592E-04	-.16639E-05	0.91589E-04
11.2	-.69730E-07	0.13968E-05	-.86892E-05	0.45105E-04	0.36074E-04	-.16604E-05	0.92301E-04
11.4	-.74421E-07	0.14712E-05	-.90389E-05	0.46294E-04	0.36550E-04	-.16568E-05	0.93006E-04
11.6	-.79296E-07	0.15476E-05	-.93934E-05	0.47484E-04	0.37020E-04	-.16530E-05	0.93705E-04
11.8	-.84357E-07	0.16258E-05	-.97528E-05	0.48674E-04	0.37483E-04	-.16490E-05	0.94397E-04
12.0	-.89603E-07	0.17059E-05	-.10117E-04	0.49862E-04	0.37941E-04	-.16449E-05	0.95082E-04
12.2	-.95031E-07	0.17878E-05	-.10485E-04	0.51049E-04	0.38393E-04	-.16406E-05	0.95761E-04
12.4	-.10065E-06	0.18715E-05	-.10857E-04	0.52234E-04	0.38840E-04	-.16361E-05	0.96434E-04
12.6	-.10644E-06	0.19569E-05	-.11233E-04	0.53417E-04	0.39282E-04	-.16314E-05	0.97101E-04
12.8	-.11242E-06	0.20439E-05	-.11612E-04	0.54598E-04	0.39719E-04	-.16266E-05	0.97761E-04
13.0	-.11858E-06	0.21326E-05	-.11995E-04	0.55774E-04	0.40152E-04	-.16216E-05	0.98416E-04
13.2	-.12491E-06	0.22229E-05	-.12381E-04	0.56947E-04	0.40578E-04	-.16164E-05	0.99064E-04
13.4	-.13144E-06	0.23149E-05	-.12771E-04	0.58119E-04	0.41000E-04	-.16110E-05	0.99707E-04
13.6	-.13814E-06	0.24084E-05	-.13164E-04	0.59286E-04	0.41418E-04	-.16055E-05	0.10034E-03
13.8	-.14501E-06	0.25033E-05	-.13559E-04	0.60449E-04	0.41832E-04	-.15998E-05	0.10097E-03
14.0	-.15205E-06	0.25996E-05	-.13956E-04	0.61605E-04	0.42242E-04	-.15939E-05	0.10160E-03
14.2	-.15926E-06	0.26971E-05	-.14356E-04	0.62756E-04	0.42649E-04	-.15879E-05	0.10222E-03
14.4	-.16663E-06	0.27961E-05	-.14757E-04	0.63902E-04	0.43052E-04	-.15817E-05	0.10283E-03
14.6	-.17418E-06	0.28964E-05	-.15161E-04	0.65044E-04	0.43450E-04	-.15753E-05	0.10344E-03
14.8	-.18189E-06	0.29980E-05	-.15567E-04	0.66180E-04	0.43845E-04	-.15688E-05	0.10405E-03
15.0	-.18975E-06	0.31006E-05	-.15973E-04	0.67309E-04	0.44237E-04	-.15621E-05	0.10464E-03
15.2	-.19776E-06	0.32043E-05	-.16381E-04	0.68430E-04	0.44626E-04	-.15552E-05	0.10524E-03
15.4	-.20593E-06	0.33090E-05	-.16790E-04	0.69545E-04	0.45012E-04	-.15482E-05	0.10582E-03
15.6	-.21423E-06	0.34147E-05	-.17200E-04	0.70652E-04	0.45396E-04	-.15410E-05	0.10640E-03
15.8	-.22269E-06	0.35214E-05	-.17610E-04	0.71753E-04	0.45777E-04	-.15337E-05	0.10698E-03
16.0	-.23128E-06	0.36290E-05	-.18021E-04	0.72846E-04	0.46155E-04	-.15261E-05	0.10755E-03
16.2	-.24001E-06	0.37373E-05	-.18432E-04	0.73930E-04	0.46531E-04	-.15184E-05	0.10812E-03
16.4	-.24886E-06	0.38464E-05	-.18843E-04	0.75006E-04	0.46906E-04	-.15106E-05	0.10868E-03
16.6	-.25783E-06	0.39561E-05	-.19254E-04	0.76072E-04	0.47279E-04	-.15027E-05	0.10924E-03
16.8	-.26692E-06	0.40664E-05	-.19663E-04	0.77129E-04	0.47651E-04	-.14946E-05	0.10979E-03

z	C(1)	C(2)	C(3)	C(4)	C(5)	C(6)	C(7)
17.0	-.27611E-06	0.41772E-05	-.20072E-04	0.78177E-04	0.48021E-04	-.14863E-05	0.11033E-03
17.2	-.28543E-06	0.42886E-05	-.20481E-04	0.79217E-04	0.48388E-04	-.14778E-05	0.11087E-03
17.4	-.29484E-06	0.44004E-05	-.20889E-04	0.80246E-04	0.48756E-04	-.14692E-05	0.11141E-03
17.6	-.30435E-06	0.45125E-05	-.21295E-04	0.81265E-04	0.49122E-04	-.14604E-05	0.11194E-03
17.8	-.31393E-06	0.46248E-05	-.21698E-04	0.82273E-04	0.49489E-04	-.14516E-05	0.11246E-03
18.0	-.32361E-06	0.47374E-05	-.22101E-04	0.83270E-04	0.49855E-04	-.14425E-05	0.11298E-03
18.2	-.33336E-06	0.48501E-05	-.22502E-04	0.84258E-04	0.50219E-04	-.14332E-05	0.11350E-03
18.4	-.34319E-06	0.49630E-05	-.22900E-04	0.85234E-04	0.50584E-04	-.14239E-05	0.11401E-03
18.6	-.35308E-06	0.50758E-05	-.23296E-04	0.86199E-04	0.50949E-04	-.14144E-05	0.11451E-03
18.8	-.36302E-06	0.51885E-05	-.23689E-04	0.87151E-04	0.51316E-04	-.14048E-05	0.11501E-03
19.0	-.37301E-06	0.53010E-05	-.24079E-04	0.88091E-04	0.51682E-04	-.13950E-05	0.11551E-03
19.2	-.38305E-06	0.54134E-05	-.24467E-04	0.89020E-04	0.52048E-04	-.13851E-05	0.11600E-03
19.4	-.39313E-06	0.55256E-05	-.24851E-04	0.89937E-04	0.52415E-04	-.13750E-05	0.11649E-03
19.6	-.40323E-06	0.56373E-05	-.25231E-04	0.90840E-04	0.52784E-04	-.13649E-05	0.11697E-03
19.8	-.41334E-06	0.57484E-05	-.25607E-04	0.91729E-04	0.53155E-04	-.13546E-05	0.11744E-03
20.0	-.42347E-06	0.58590E-05	-.25979E-04	0.92605E-04	0.53527E-04	-.13442E-05	0.11791E-03
20.2	-.43361E-06	0.59692E-05	-.26347E-04	0.93468E-04	0.53900E-04	-.13335E-05	0.11838E-03
20.4	-.44374E-06	0.60786E-05	-.26710E-04	0.94317E-04	0.54276E-04	-.13228E-05	0.11884E-03
20.6	-.45385E-06	0.61871E-05	-.27068E-04	0.95150E-04	0.54655E-04	-.13120E-05	0.11930E-03
20.8	-.46391E-06	0.62945E-05	-.27420E-04	0.95967E-04	0.55037E-04	-.13011E-05	0.11975E-03
21.0	-.47392E-06	0.64007E-05	-.27765E-04	0.96766E-04	0.55423E-04	-.12901E-05	0.12020E-03
21.2	-.48387E-06	0.65057E-05	-.28104E-04	0.97549E-04	0.55812E-04	-.12790E-05	0.12064E-03
21.4	-.49377E-06	0.66095E-05	-.28437E-04	0.98317E-04	0.56206E-04	-.12679E-05	0.12108E-03
21.6	-.50362E-06	0.67121E-05	-.28763E-04	0.99068E-04	0.56603E-04	-.12566E-05	0.12151E-03
21.8	-.51338E-06	0.68133E-05	-.29083E-04	0.99802E-04	0.57003E-04	-.12452E-05	0.12194E-03
22.0	-.52306E-06	0.69131E-05	-.29396E-04	0.10052E-03	0.57408E-04	-.12337E-05	0.12237E-03
22.2	-.53265E-06	0.70113E-05	-.29701E-04	0.10122E-03	0.57817E-04	-.12220E-05	0.12278E-03
22.4	-.54217E-06	0.71083E-05	-.30001E-04	0.10190E-03	0.58229E-04	-.12103E-05	0.12320E-03
22.6	-.55159E-06	0.72038E-05	-.30293E-04	0.10257E-03	0.58646E-04	-.11984E-05	0.12361E-03
22.8	-.56091E-06	0.72977E-05	-.30579E-04	0.10323E-03	0.59066E-04	-.11863E-05	0.12401E-03

z	C(1)	C(2)	C(3)	C(4)	C(5)	C(6)	C(7)
23.0	-.57012E-06	0.73900E-05	-.30857E-04	0.10386E-03	0.59490E-04	-.11741E-05	0.12442E-03
23.2	-.57922E-06	0.74806E-05	-.31128E-04	0.10448E-03	0.59919E-04	-.11618E-05	0.12481E-03
23.4	-.58822E-06	0.75697E-05	-.31393E-04	0.10508E-03	0.60351E-04	-.11493E-05	0.12520E-03
23.6	-.59710E-06	0.76573E-05	-.31651E-04	0.10567E-03	0.60787E-04	-.11366E-05	0.12559E-03
23.8	-.60586E-06	0.77431E-05	-.31901E-04	0.10625E-03	0.61227E-04	-.11238E-05	0.12597E-03
24.0	-.61448E-06	0.78271E-05	-.32144E-04	0.10680E-03	0.61671E-04	-.11108E-05	0.12635E-03
24.2	-.62297E-06	0.79093E-05	-.32379E-04	0.10734E-03	0.62119E-04	-.10976E-05	0.12672E-03
24.4	-.63134E-06	0.79898E-05	-.32608E-04	0.10786E-03	0.62571E-04	-.10843E-05	0.12709E-03
24.6	-.63956E-06	0.80687E-05	-.32829E-04	0.10837E-03	0.63027E-04	-.10708E-05	0.12745E-03
24.8	-.64764E-06	0.81456E-05	-.33043E-04	0.10887E-03	0.63487E-04	-.10572E-05	0.12781E-03
25.0	-.65556E-06	0.82205E-05	-.33249E-04	0.10934E-03	0.63951E-04	-.10433E-05	0.12816E-03
25.2	-.66333E-06	0.82936E-05	-.33447E-04	0.10981E-03	0.64420E-04	-.10293E-05	0.12851E-03
25.4	-.67094E-06	0.83648E-05	-.33639E-04	0.11025E-03	0.64893E-04	-.10151E-05	0.12885E-03
25.6	-.67840E-06	0.84341E-05	-.33823E-04	0.11068E-03	0.65370E-04	-.10008E-05	0.12919E-03
25.8	-.68569E-06	0.85014E-05	-.33999E-04	0.11110E-03	0.65852E-04	-.98627E-06	0.12952E-03
26.0	-.69279E-06	0.85665E-05	-.34167E-04	0.11150E-03	0.66338E-04	-.97158E-06	0.12985E-03
26.2	-.69972E-06	0.86296E-05	-.34327E-04	0.11188E-03	0.66829E-04	-.95672E-06	0.13018E-03
26.4	-.70648E-06	0.86907E-05	-.34479E-04	0.11225E-03	0.67324E-04	-.94173E-06	0.13050E-03
26.6	-.71306E-06	0.87498E-05	-.34624E-04	0.11260E-03	0.67823E-04	-.92658E-06	0.13081E-03
26.8	-.71944E-06	0.88066E-05	-.34761E-04	0.11294E-03	0.68328E-04	-.91128E-06	0.13112E-03
27.0	-.72562E-06	0.88612E-05	-.34890E-04	0.11326E-03	0.68837E-04	-.89583E-06	0.13143E-03
27.2	-.73160E-06	0.89136E-05	-.35010E-04	0.11356E-03	0.69351E-04	-.88023E-06	0.13173E-03
27.4	-.73740E-06	0.89639E-05	-.35123E-04	0.11385E-03	0.69869E-04	-.86450E-06	0 13202E-03
27.6	-.74299E-06	0.90120E-05	-.35227E-04	0.11413E-03	0.70392E-04	-.84864E-06	0.13232E-03
27.8	-.74836E-06	0.90578E-05	-.35324E-04	0.11439E-03	0.70920E-04	-.83264E-06	0.13260E-03
28.0	-.75352E-06	0.91012E-05	-.35411E-04	0.11463E-03	0.71453E-04	-.81651E-06	0.13289E-03
28.2	-.75845E-06	0.91423E-05	-.35491E-04	0.11486E-03	0.71991E-04	-.80026E-06	0.13316E-03
28.4	-.76318E-06	0.91811E-05	-.35562E-04	0.11507E-03	0.72534E-04	-.78391E-06	0.13344E-03
28.6	-.76769E-06	0.92177E-05	-.35626E-04	0.11527E-03	0.73081E-04	-.76745E-06	0.13371E-03
28.8	-.77197E-06	0.92518E-05	-.35681E-04	0.11545E-03	0.73634E-04	-.75090E-06	0.13397E-03

z	C(1)	C(2)	C(3)	C(4)	C(5)	C(6)	C(7)
29.0	-.77601E-06	0.92835E-05	-.35727E-04	0.11562E-03	0.74191E-04	-.73423E-06	0.13423E-03
29.2	-.77982E-06	0.93127E-05	-.35764E-04	0.11577E-03	0.74754E-04	-.71748E-06	0.13449E-03
29.4	-.78340E-06	0.93397E-05	-.35794E-04	0.11590E-03	0.75321E-04	-.70066E-06	0.13474E-03
29.6	-.78676E-06	0.93643E-05	-.35816E-04	0.11602E-03	0.75893E-04	-.68376E-06	0.13498E-03
29.8	-.78987E-06	0.93864E-05	-.35829E-04	0.11613E-03	0.76470E-04	-.66679E-06	0.13523E-03
30.0	-.79273E-06	0.94060E-05	-.35833E-04	0.11622E-03	0.77051E-04	-.64975E-06	0.13546E-03
30.2	-.79537E-06	0.94235E-05	-.35831E-04	0.11630E-03	0.77636E-04	-.63250E-06	0.13570E-03
30.4	-.79781E-06	0.94390E-05	-.35822E-04	0.11637E-03	0.78223E-04	-.61506E-06	0.13593E-03
30.6	-.80000E-06	0.94520E-05	-.35805E-04	0.11642E-03	0.78815E-04	-.59760E-06	0.13615E-03
30.8	-.80194E-06	0.94624E-05	-.35779E-04	0.11646E-03	0.79412E-04	-.58015E-06	0.13637E-03
31.0	-.80360E-06	0.94701E-05	-.35743E-04	0.11648E-03	0.80016E-04	-.56273E-06	0.13659E-03
31.2	-.80500E-06	0.94752E-05	-.35699E-04	0.11649E-03	0.80625E-04	-.54536E-06	0.13680E-03
31.4	-.80615E-06	0.94778E-05	-.35646E-04	0.11648E-03	0.81239E-04	-.52805E-06	0.13701E-03
31.6	-.80704E-06	0.94779E-05	-.35584E-04	0.11645E-03	0.81859E-04	-.51081E-06	0.13722E-03
31.8	-.80766E-06	0.94752E-05	-.35513E-04	0.11641E-03	0.82485E-04	-.49365E-06	0.13742E-03
32.0	-.80800E-06	0.94699E-05	-.35433E-04	0.11636E-03	0.83116E-04	-.47658E-06	0.13761E-03
32.2	-.80806E-06	0.94618E-05	-.35344E-04	0.11629E-03	0.83753E-04	-.45960E-06	0.13781E-03
32.4	-.80784E-06	0.94510E-05	-.35246E-04	0.11620E-03	0.84397E-04	-.44269E-06	0.13800E-03
32.6	-.80734E-06	0.94374E-05	-.35138E-04	0.11610E-03	0.85046E-04	-.42588E-06	0.13818E-03
32.8	-.80653E-06	0.94209E-05	-.35020E-04	0.11598E-03	0.85702E-04	-.40915E-06	0.13836E-03
33.0	-.80543E-06	0.94015E-05	-.34893E-04	0.11584E-03	0.86364E-04	-.39252E-06	0.13854E-03
33.2	-.80404E-06	0.93793E-05	-.34757E-04	0.11569E-03	0.87031E-04	-.37599E-06	0.13872E-03
33.4	-.80236E-06	0.93545E-05	-.34611E-04	0.11552E-03	0.87705E-04	-.35956E-06	0.13889E-03
33.6	-.80040E-06	0.93269E-05	-.34457E-04	0.11534E-03	0.88383E-04	-.34322E-06	0.13905E-03
33.8	-.79816E-06	0.92966E-05	-.34294E-04	0.11514E-03	0.89068E-04	-.32699E-06	0.13922E-03
34.0	-.79562E-06	0.92636E-05	-.34122E-04	0.11493E-03	0.89757E-04	-.31087E-06	0.13938E-03
34.2	-.79279E-06	0.92279E-05	-.33941E-04	0.11471E-03	0.90452E-04	-.29485E-06	0.13954E-03
34.4	-.78970E-06	0.91897E-05	-.33752E-04	0.11447E-03	0.91151E-04	-.27895E-06	0.13969E-03
34.6	-.78634E-06	0.91490E-05	-.33555E-04	0.11422E-03	0.91855E-04	-.26316E-06	0.13984E-03
34.8	-.78271E-06	0.91057E-05	-.33350E-04	0.11395E-03	0.92563E-04	-.24749E-06	0.13999E-03

z	C(1)	C(2)	C(3)	C(4)	C(5)	C(6)	C(7)
35.0	-.77880E-06	0.90600E-05	-.33137E-04	0.11367E-03	0.93275E-04	-.23195E-06	0.14013E-03
35.2	-.77463E-06	0.90118E-05	-.32916E-04	0.11338E-03	0.93992E-04	-.21654E-06	0.14027E-03
35.4	-.77021E-06	0.89613E-05	-.32688E-04	0.11308E-03	0.94712E-04	-.20125E-06	0.14041E-03
35.6	-.76555E-06	0.89086E-05	-.32454E-04	0.11277E-03	0.95435E-04	-.18611E-06	0.14055E-03
35.8	-.76063E-06	0.88537E-05	-.32212E-04	0.11245E-03	0.96162E-04	-.17110E-06	0.14068E-03
36.0	-.75546E-06	0.87965E-05	-.31963E-04	0.11211E-03	0.96892E-04	-.15625E-06	0.14081E-03
36.2	-.75006E-06	0.87371E-05	-.31707E-04	0.11176E-03	0.97625E-04	-.14155E-06	0.14093E-03
36.4	-.74442E-06	0.86757E-05	-.31445E-04	0.11141E-03	0.98361E-04	-.12699E-06	0.14106E-03
36.6	-.73852E-06	0.86120E-05	-.31177E-04	0.11104E-03	0.99098E-04	-.11248E-06	0.14118E-03
36.8	-.73236E-06	0.85462E-05	-.30903E-04	0.11067E-03	0.99836E-04	-.98035E-07	0.14130E-03
37.0	-.72599E-06	0.84784E-05	-.30623E-04	0.11029E-03	0.10058E-03	-.83804E-07	0.14141E-03
37.2	-.71942E-06	0.84088E-05	-.30337E-04	0.10989E-03	0.10132E-03	-.69791E-07	0.14153E-03
37.4	-.71267E-06	0.83376E-05	-.30046E-04	0.10949E-03	0.10207E-03	-.55995E-07	0.14164E-03
37.6	-.70573E-06	0.82648E-05	-.29750E-04	0.10909E-03	0.10281E-03	-.42435E-07	0.14174E-03
37.8	-.69862E-06	0.81905E-05	-.29449E-04	0.10867E-03	0.10356E-03	-.29125E-07	0.14185E-03
38.0	-.69133E-06	0.81146E-05	-.29144E-04	0.10824E-03	0.10432E-03	-.16081E-07	0.14195E-03
38.2	-.68388E-06	0.80372E-05	-.28834E-04	0.10781E-03	0.10507E-03	-.32943E-08	0.14205E-03
38.4	-.67627E-06	0.79584E-05	-.28520E-04	0.10737E-03	0.10583E-03	0.92451E-08	0.14215E-03
38.6	-.66851E-06	0.78783E-05	-.28202E-04	0.10692E-03	0.10658E-03	0.21527E-07	0.14225E-03
38.8	-.66060E-06	0.77968E-05	-.27879E-04	0.10647E-03	0.10734E-03	0.33541E-07	0.14234E-03
39.0	-.65254E-06	0.77141E-05	-.27553E-04	0.10601E-03	0.10810E-03	0.45276E-07	0.14243E-03
39.2	-.64434E-06	0.76302E-05	-.27223E-04	0.10554E-03	0.10887E-03	0.56745E-07	0.14252E-03
39.4	-.63600E-06	0.75451E-05	-.26890E-04	0.10507E-03	0.10963E-03	0.67961E-07	0.14261E-03
39.6	-.62754E-06	0.74589E-05	-.26554E-04	0.10459E-03	0.11039E-03	0.78915E-07	0.14269E-03
39.8	-.61895E-06	0.73717E-05	-.26215E-04	0.10411E-03	0.11115E-03	0.89600E-07	0.14278E-03
40.0	-.61024E-06	0.72835E-05	-.25873E-04	0.10362E-03	0.11192E-03	0.10001E-06	0.14286E-03
40.2	-.60142E-06	0.71944E-05	-.25529E-04	0.10313E-03	0.11268E-03	0.11015E-06	0.14294E-03
40.4	-.59249E-06	0.71043E-05	-.25182E-04	0.10263E-03	0.11344E-03	0.12004E-06	0.14302E-03
40.6	-.58346E-06	0.70135E-05	-.24833E-04	0.10213E-03	0.11420E-03	0.12967E-06	0.14309E-03
40.8	-.57433E-06	0.69218E-05	-.24482E-04	0.10163E-03	0.11496E-03	0.13904E-06	0.14317E-03

z	C(1)	C(2)	C(3)	C(4)	C(5)	C(6)	C(7)
41.0	-.56510E-06	0.68294E-05	-.24129E-04	0.10113E-03	0.11572E-03	0.14813E-06	0.14324E-03
41.2	-.55579E-06	0.67364E-05	-.23775E-04	0.10062E-03	0.11648E-03	0.15696E-06	0.14331E-03
41.4	-.54628E-06	0.66418E-05	-.23417E-04	0.10011E-03	0.11724E-03	0.16559E-06	0.14338E-03
41.6	-.53659E-06	0.65458E-05	-.23055E-04	0.99589E-04	0.11800E-03	0.17398E-06	0.14345E-03
41.8	-.52687E-06	0.64496E-05	-.22693E-04	0.99071E-04	0.11875E-03	0.18211E-06	0.14351E-03
42.0	-.51714E-06	0.63533E-05	-.22332E-04	0.98553E-04	0.11950E-03	0.18996E-06	0.14358E-03
42.2	-.50739E-06	0.62571E-05	-.21970E-04	0.98035E-04	0.12025E-03	0.19755E-06	0.14364E-03
42.4	-.49765E-06	0.61610E-05	-.21610E-04	0.97517E-04	0.12100E-03	0.20488E-06	0.14370E-03
42.6	-.48791E-06	0.60650E-05	-.21250E-04	0.97000E-04	0.12175E-03	0.21195E-06	0.14376E-03
42.8	-.47820E-06	0.59693E-05	-.20892E-04	0.96483E-04	0.12249E-03	0.21876E-06	0.14382E-03
43.0	-.46853E-06	0.58740E-05	-.20535E-04	0.95968E-04	0.12323E-03	0.22528E-06	0.14387E-03
43.2	-.45889E-06	0.57791E-05	-.20180E-04	0.95454E-04	0.12397E-03	0.23155E-06	0.14393E-03
43.4	-.44927E-06	0.56845E-05	-.19826E-04	0.94942E-04	0.12470E-03	0.23757E-06	0.14398E-03
43.6	-.43970E-06	0.55904E-05	-.19474E-04	0.94431E-04	0.12544E-03	0.24334E-06	0.14404E-03
43.8	-.43017E-06	0.54968E-05	-.19124E-04	0.93923E-04	0.12616E-03	0.24885E-06	0.14409E-03
44.0	-.42070E-06	0.54038E-05	-.18776E-04	0.93416E-04	0.12689E-03	0.25409E-06	0.14414E-03
44.2	-.41128E-06	0.53112E-05	-.18431E-04	0.92913E-04	0.12761E-03	0.25909E-06	0.14419E-03
44.4	-.40191E-06	0.52192E-05	-.18087E-04	0.92411E-04	0.12833E-03	0.26385E-06	0.14424E-03
44.6	-.39259E-06	0.51278E-05	-.17746E-04	0.91912E-04	0.12904E-03	0.26837E-06	0.14428E-03
44.8	-.38332E-06	0.50370E-05	-.17406E-04	0.91417E-04	0.12975E-03	0.27265E-06	0.14433E-03
45.0	-.37413E-06	0.49468E-05	-.17070E-04	0.90924E-04	0.13046E-03	0.27668E-06	0.14437E-03
45.2	-.36483E-06	0.48559E-05	-.16732E-04	0.90431E-04	0.13116E-03	0.28044E-06	0.14442E-03
45.4	-.35544E-06	0.47644E-05	-.16393E-04	0.89936E-04	0.13186E-03	0.28395E-06	0.14446E-03
45.6	-.34614E-06	0.46737E-05	-.16057E-04	0.89446E-04	0.13256E-03	0.28725E-06	0.14450E-03
45.8	-.33696E-06	0.45842E-05	-.15726E-04	0.88961E-04	0.13325E-03	0.29033E-06	0.14454E-03
46.0	-.32791E-06	0.44960E-05	-.15398E-04	0.88482E-04	0.13393E-03	0.29320E-06	0.14458E-03
46.2	-.31901E-06	0.44092E-05	-.15076E-04	0.88009E-04	0.13461E-03	0.29587E-06	0.14462E-03
46.4	-.31025E-06	0.43237E-05	-.14758E-04	0.87541E-04	0.13529E-03	0.29836E-06	0.14466E-03
46.6	-.30164E-06	0.42396E-05	-.14444E-04	0.87079E-04	0.13596E-03	0.30066E-06	0.14470E-03
46.8	-.29320E-06	0.41570E-05	-.14136E-04	0.86624E-04	0.13662E-03	0.30278E-06	0.14473E-03

z	C(1)	C(2)	C(3)	C(4)	C(5)	C(6)	C(7)
47.0	-.28493E-06	0.40760E-05	-.13833E-04	0.86176E-04	0.13728E-03	0.30471E-06	0.14477E-03
47.2	-.27682E-06	0.39966E-05	-.13536E-04	0.85735E-04	0.13793E-03	0.30646E-06	0.14480E-03
47.4	-.26887E-06	0.39186E-05	-.13244E-04	0.85300E-04	0.13858E-03	0.30806E-06	0.14484E-03
47.6	-.26108E-06	0.38421E-05	-.12956E-04	0.84872E-04	0.13922E-03	0.30949E-06	0.14487E-03
47.8	-.25345E-06	0.37672E-05	-.12674E-04	0.84452E-04	0.13985E-03	0.31077E-06	0.14490E-03
48.0	-.24600E-06	0.36939E-05	-.12398E-04	0.84038E-04	0.14048E-03	0.31189E-06	0.14493E-03
48.2	-.23870E-06	0.36221E-05	-.12127E-04	0.83632E-04	0.14110E-03	0.31286E-06	0.14496E-03
48.4	-.23156E-06	0.35517E-05	-.11860E-04	0.83233E-04	0.14171E-03	0.31369E-06	0.14499E-03
48.6	-.22457E-06	0.34828E-05	-.11599E-04	0.82841E-04	0.14232E-03	0.31438E-06	0.14502E-03
48.8	-.21759E-06	0.34140E-05	-.11339E-04	0.82452E-04	0.14292E-03	0.31486E-06	0.14505E-03
49.0	-.21062E-06	0.33455E-05	-.11080E-04	0.82065E-04	0.14352E-03	0.31514E-06	0.14508E-03
49.2	-.20383E-06	0.32786E-05	-.10827E-04	0.81686E-04	0.14411E-03	0.31529E-06	0.14510E-03
49.4	-.19722E-06	0.32133E-05	-.10580E-04	0.81315E-04	0.14470E-03	0.31534E-06	0.14513E-03
49.6	-.19078E-06	0.31498E-05	-.10338E-04	0.80952E-04	0.14527E-03	0.31528E-06	0.14516E-03
49.8	-.18455E-06	0.30881E-05	-.10103E-04	0.80598E-04	0.14584E-03	0.31512E-06	0.14518E-03
50.0	-.17852E-06	0.30283E-05	-.98739E-05	0.80252E-04	0.14641E-03	0.31486E-06	0.14521E-03

Appendix C

Activity Deposition Rates for DELFIC and the AFIT Model

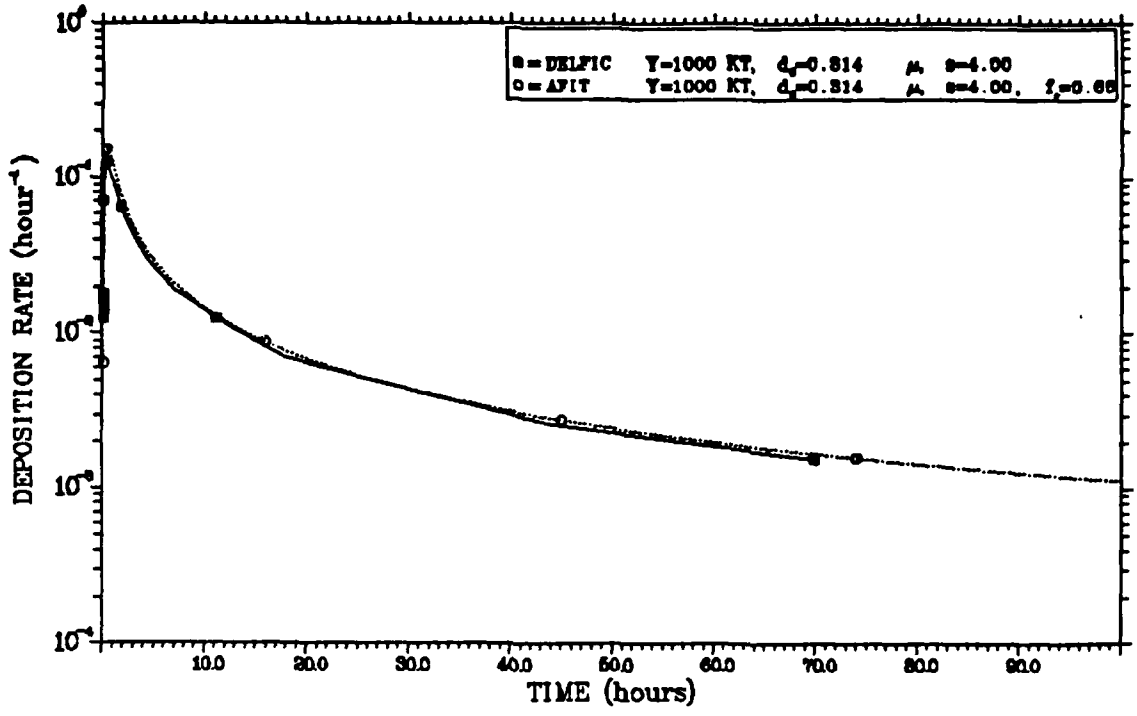

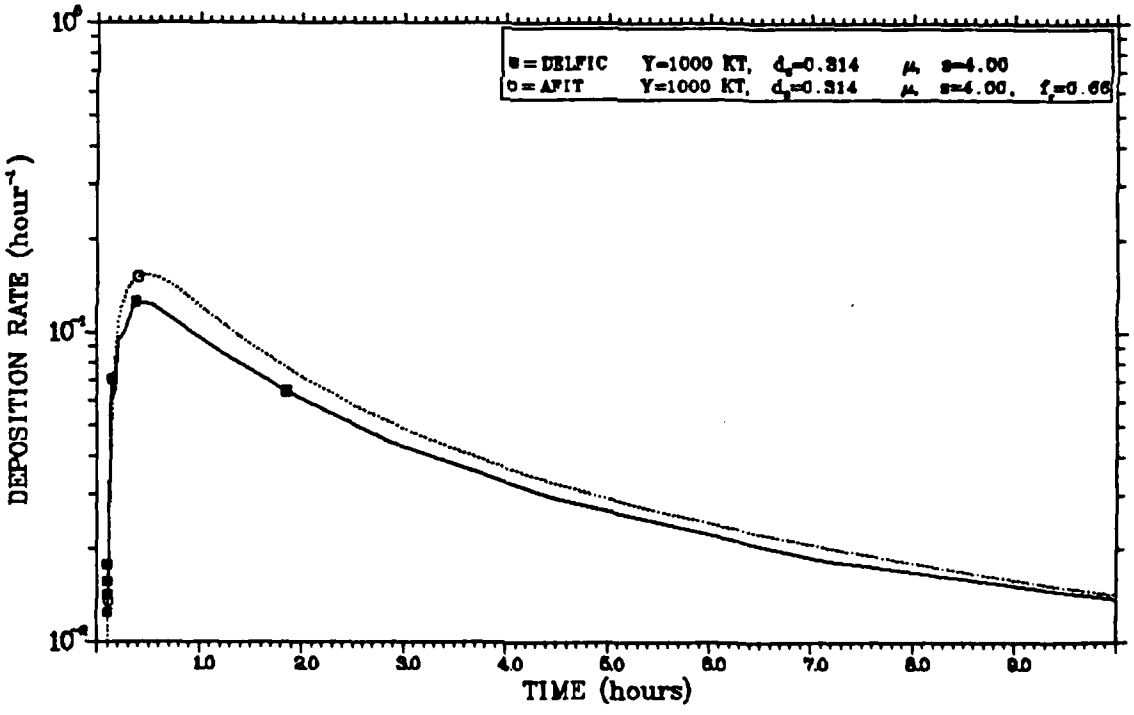

Figure C-1 Deposition Rates for the LYSTND Distribution

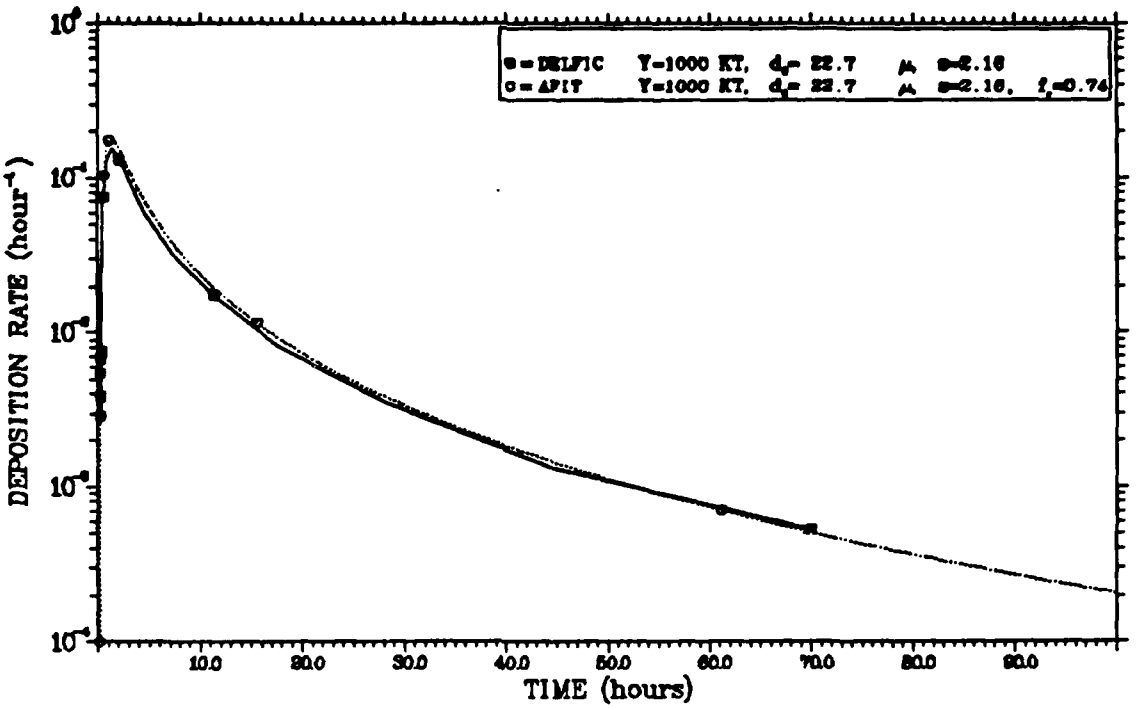

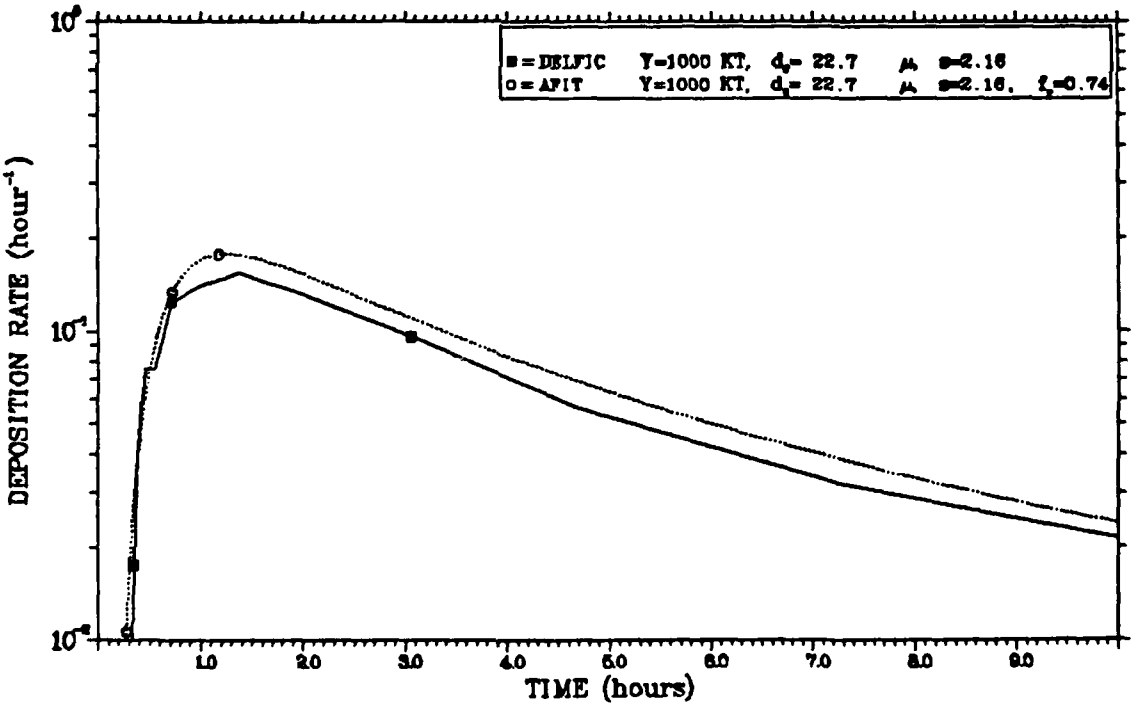

Figure C-2 Deposition Rates for the HYSTND Distribution

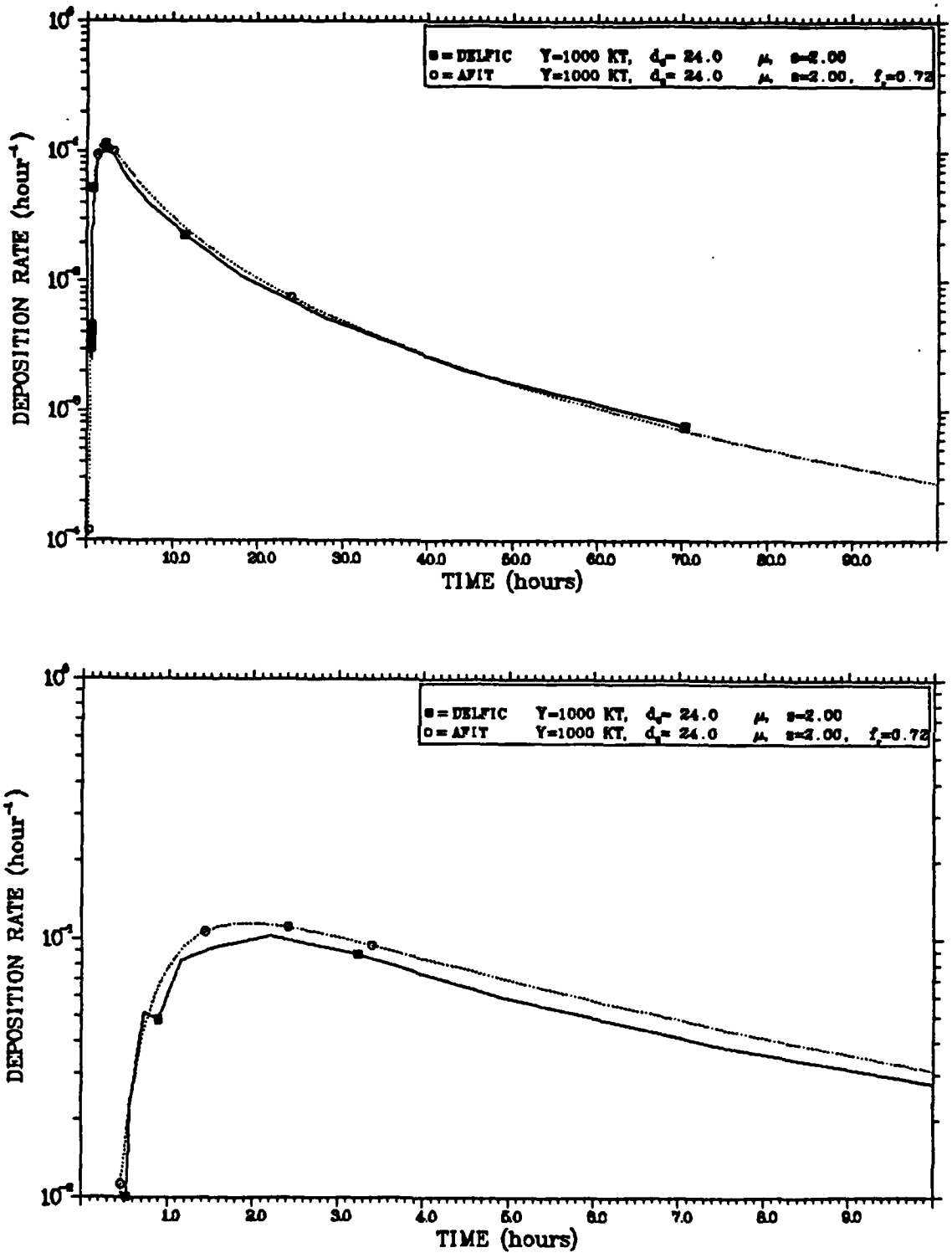

Figure C-3 Deposition Rates for the WSEG-10 Distribution

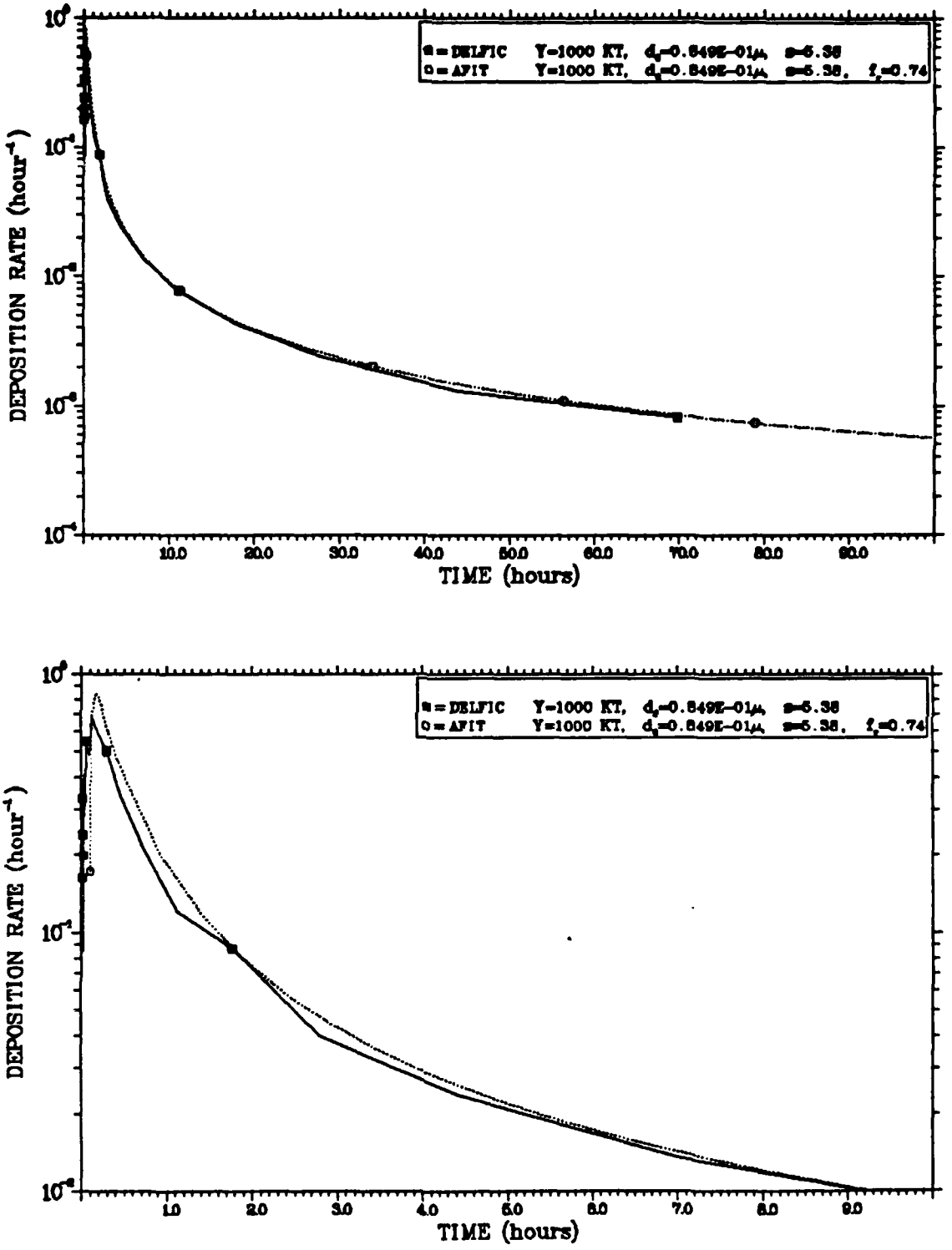

Figure C-4 Deposition Rates for the NRDLC61 Distribution

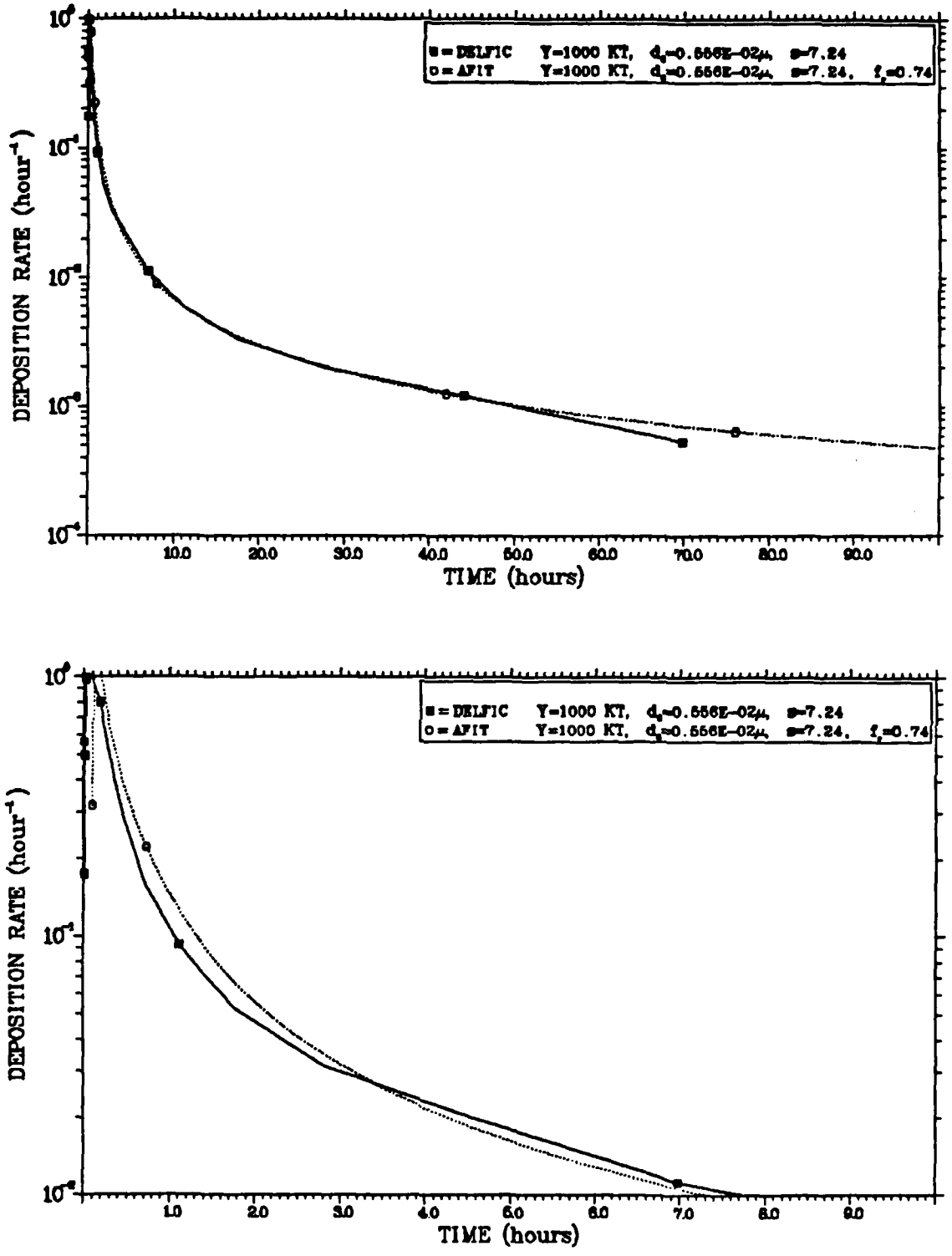

Figure C-5 Deposition Rates for the NRDLN61 Distribution

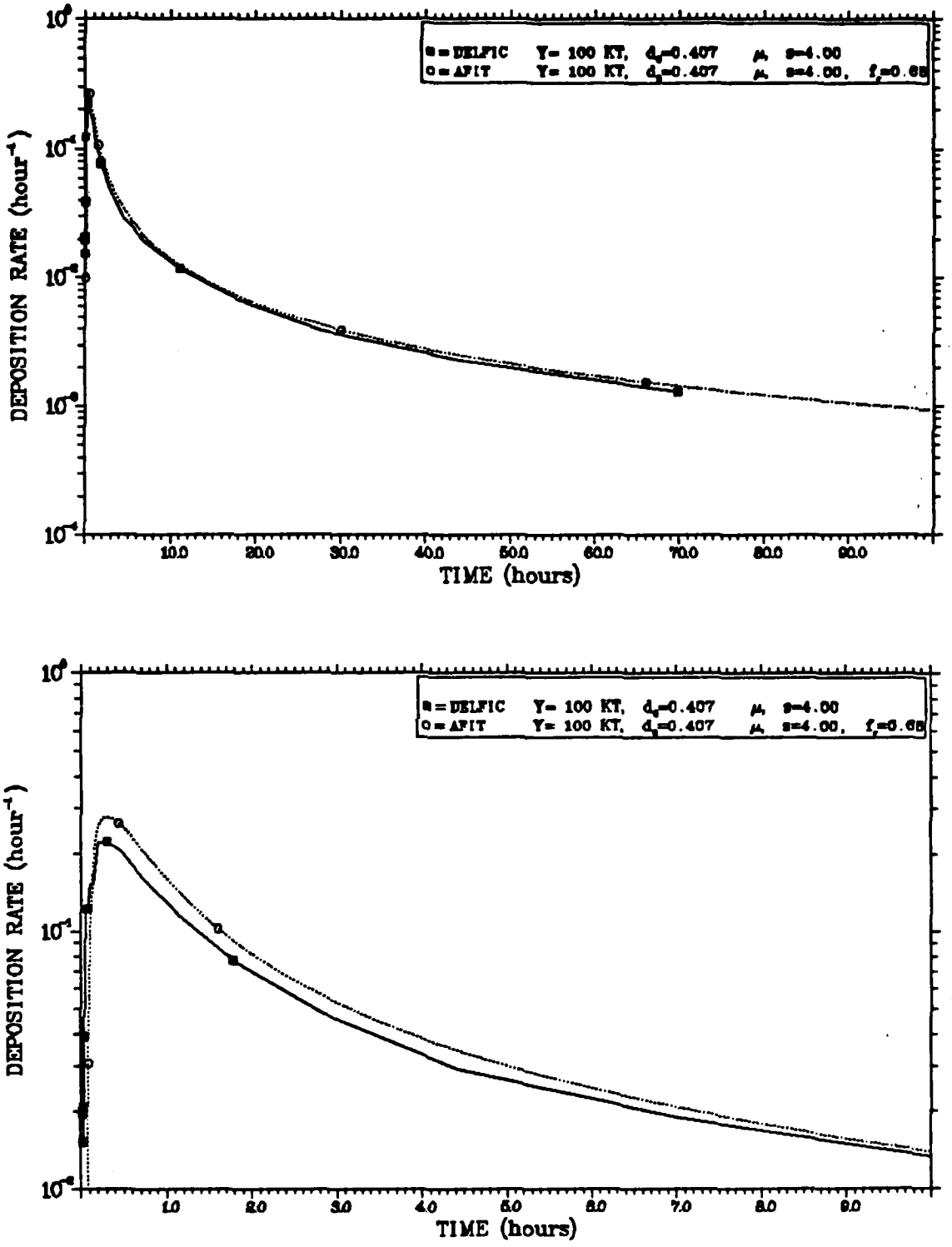

Figure C-6 Deposition Rates for the DEFAULT Distribution

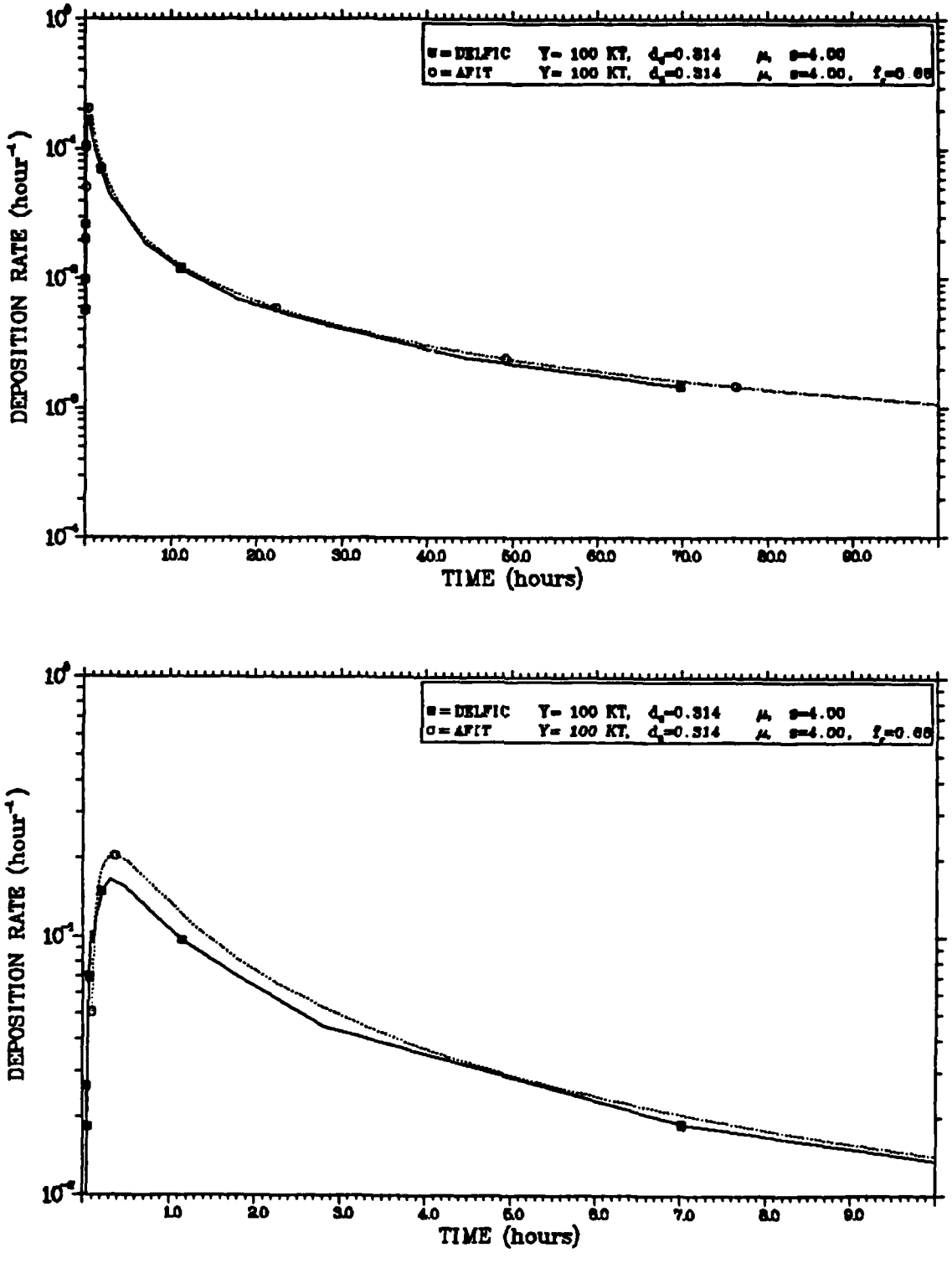

Figure C-7 Deposition Rates for the LYSTND Distribution

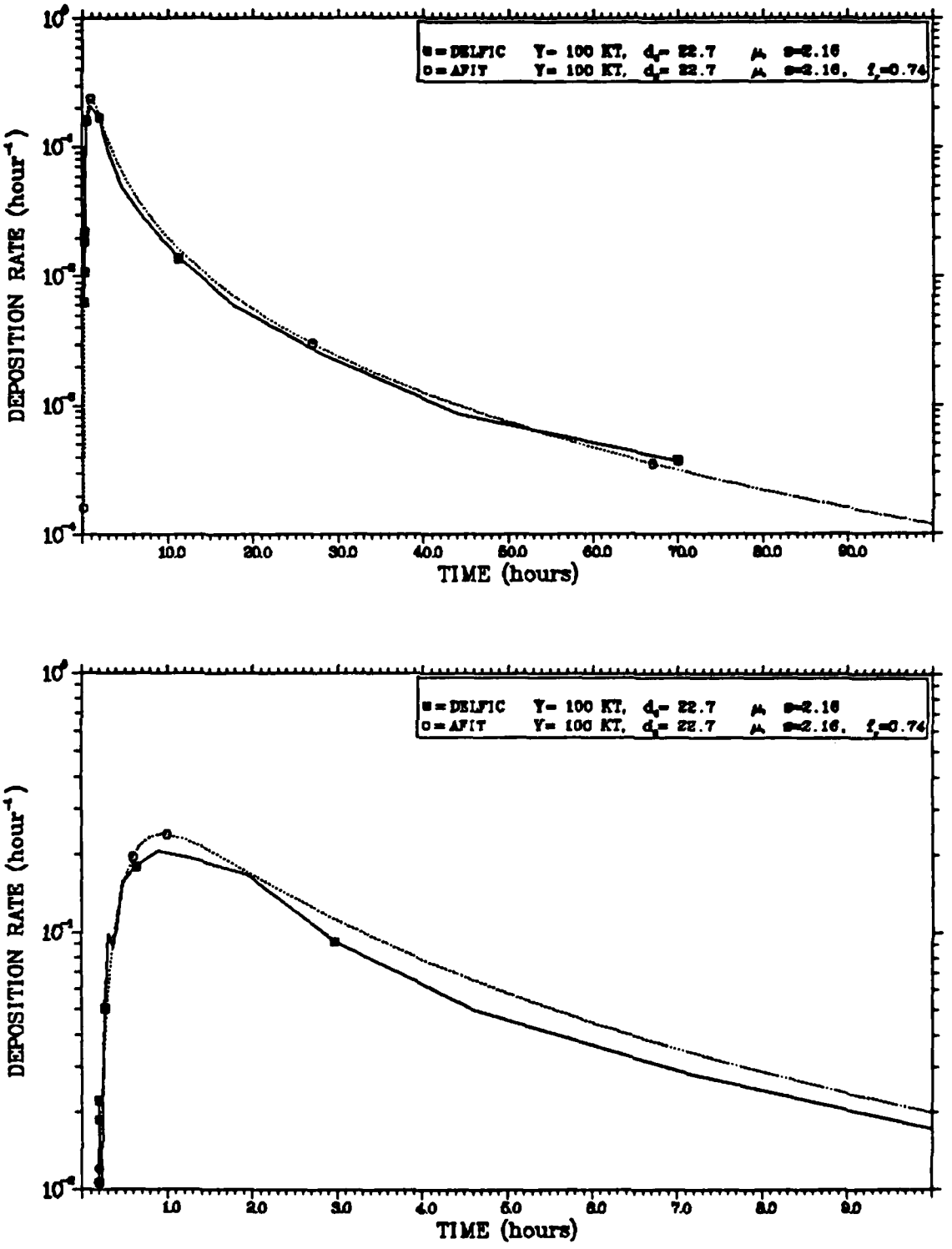

Figure C-8 Deposition Rates for the HYSTND Distribution

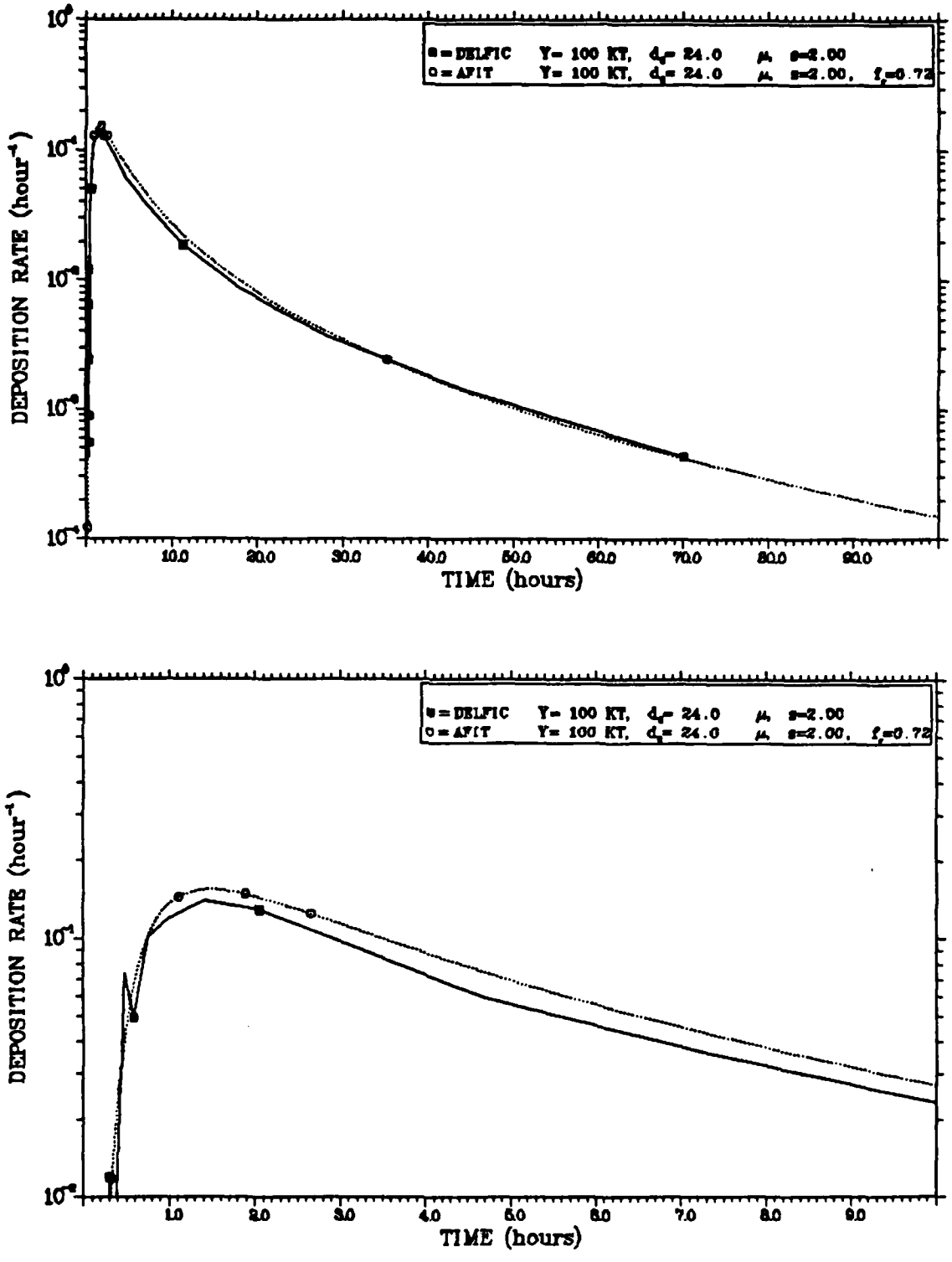

Figure C-9 Deposition Rates for the WSEG-10 Distribution

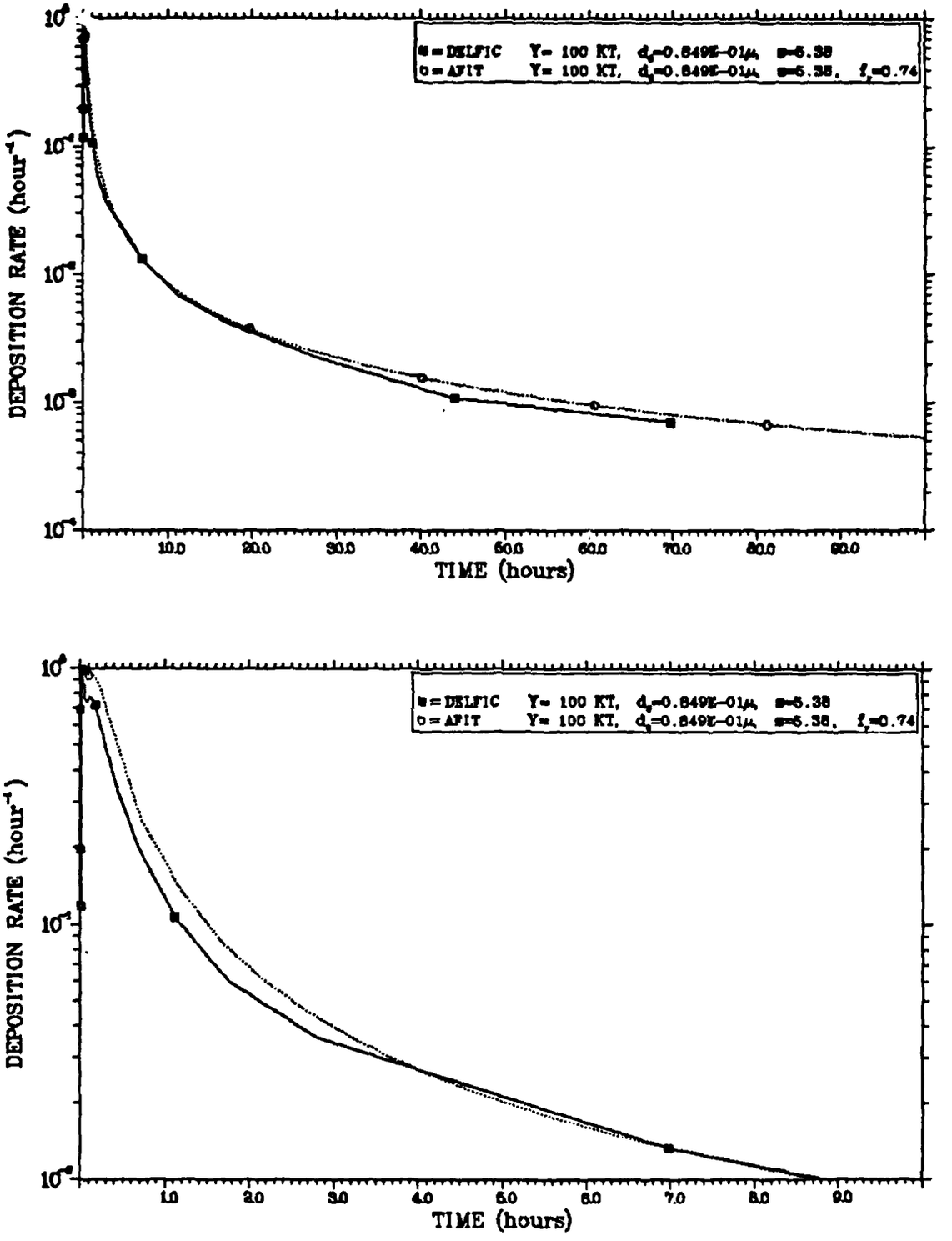

Figure C-10 Deposition Rates for the NRDLC61 Distribution

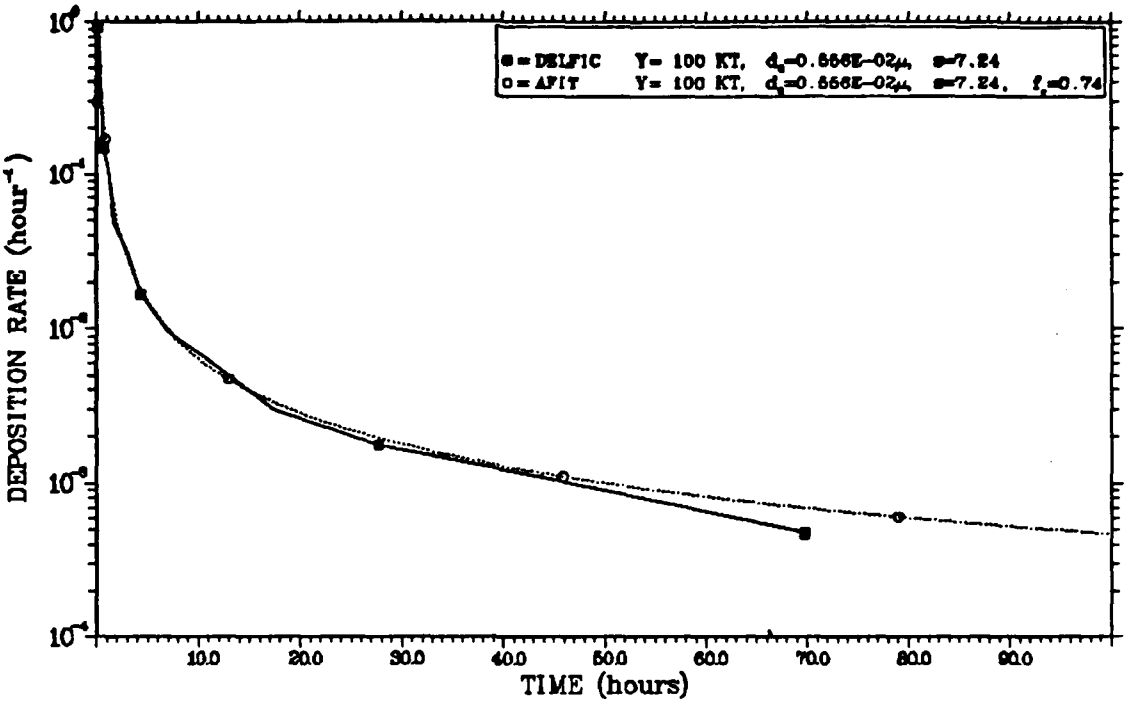

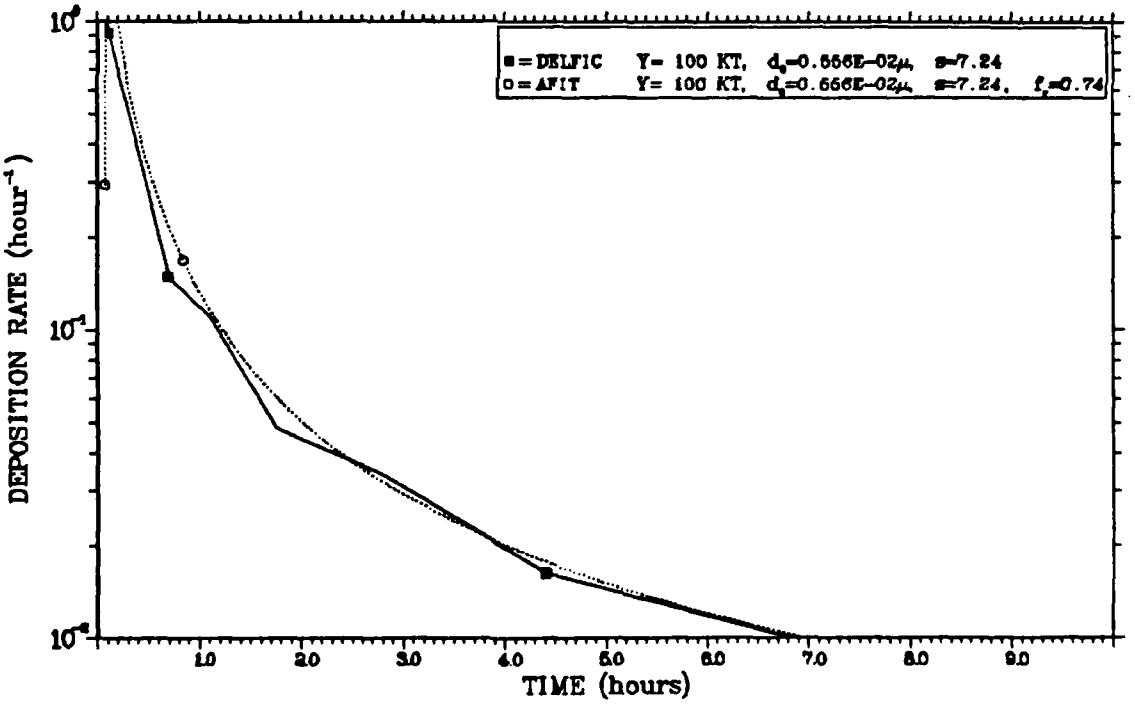

Figure C-11 Deposition Rates for the NRDLN61 Distribution

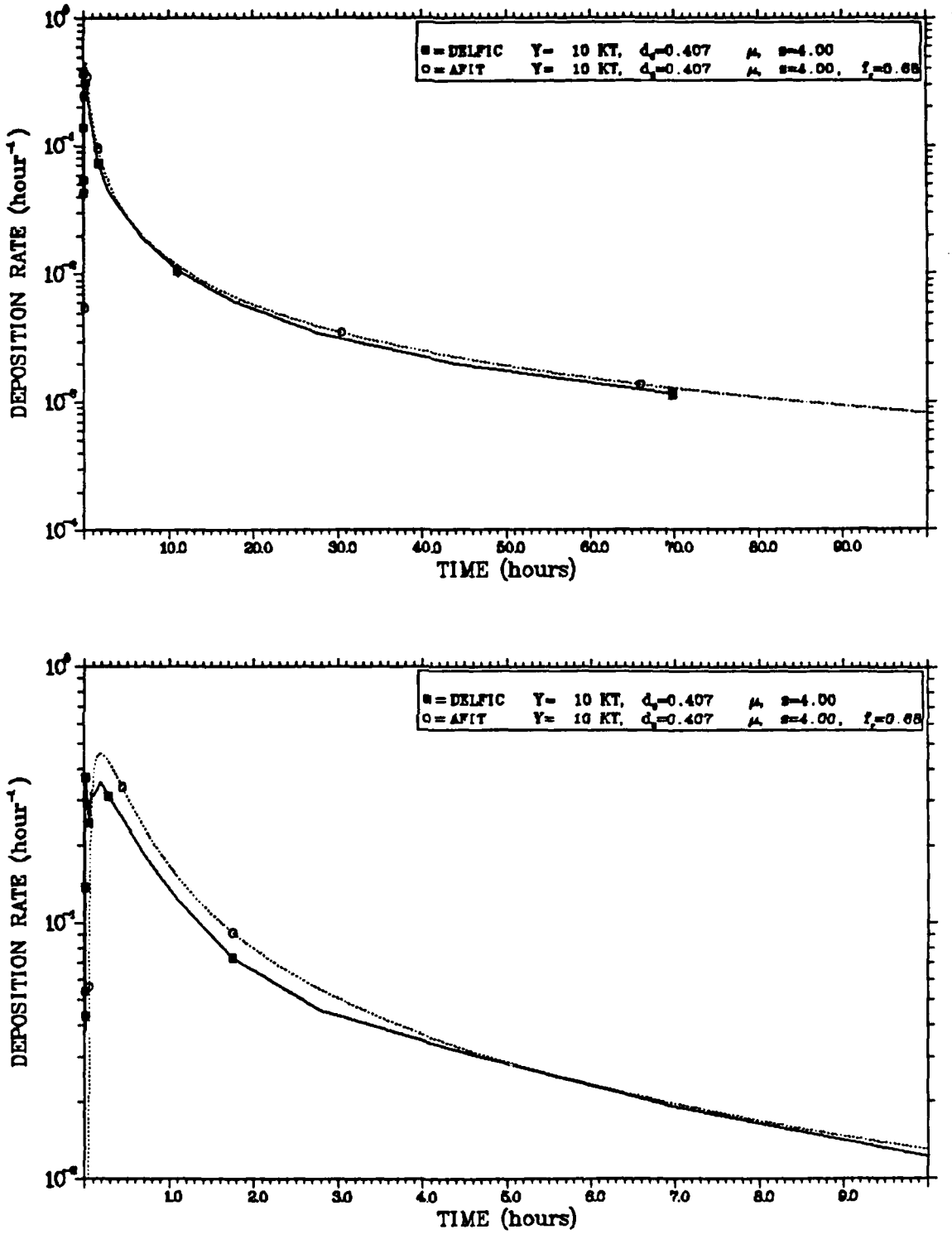

Figure C-12 Deposition Rates for the DEFAULT Distribution

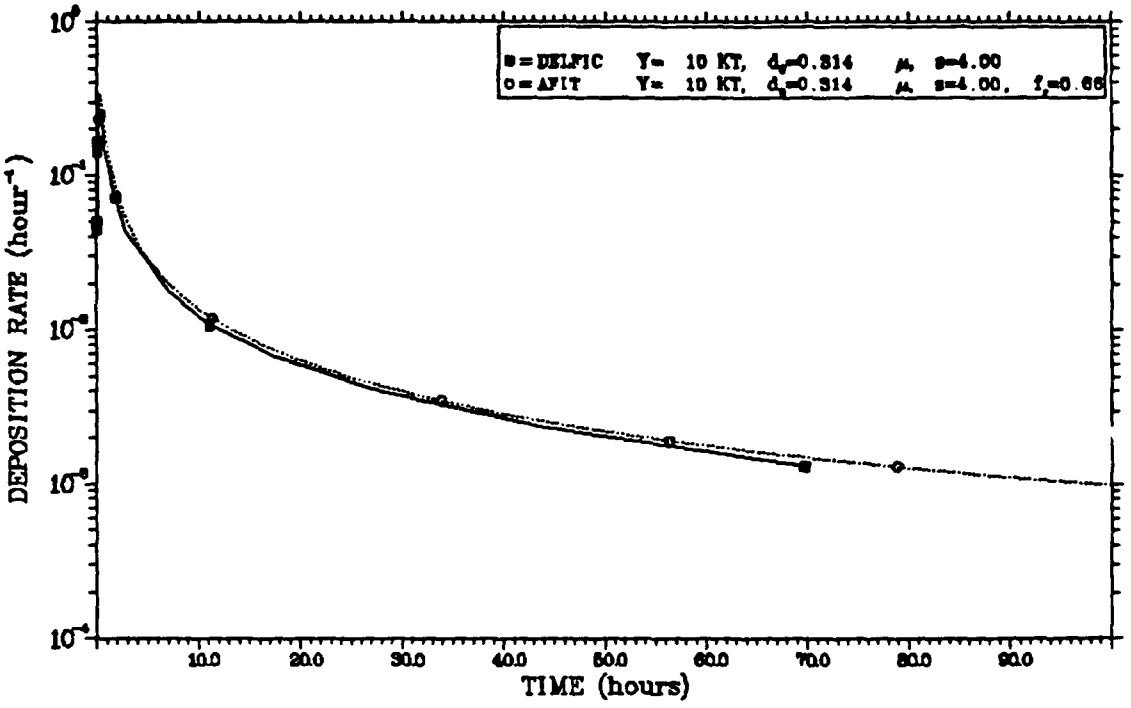

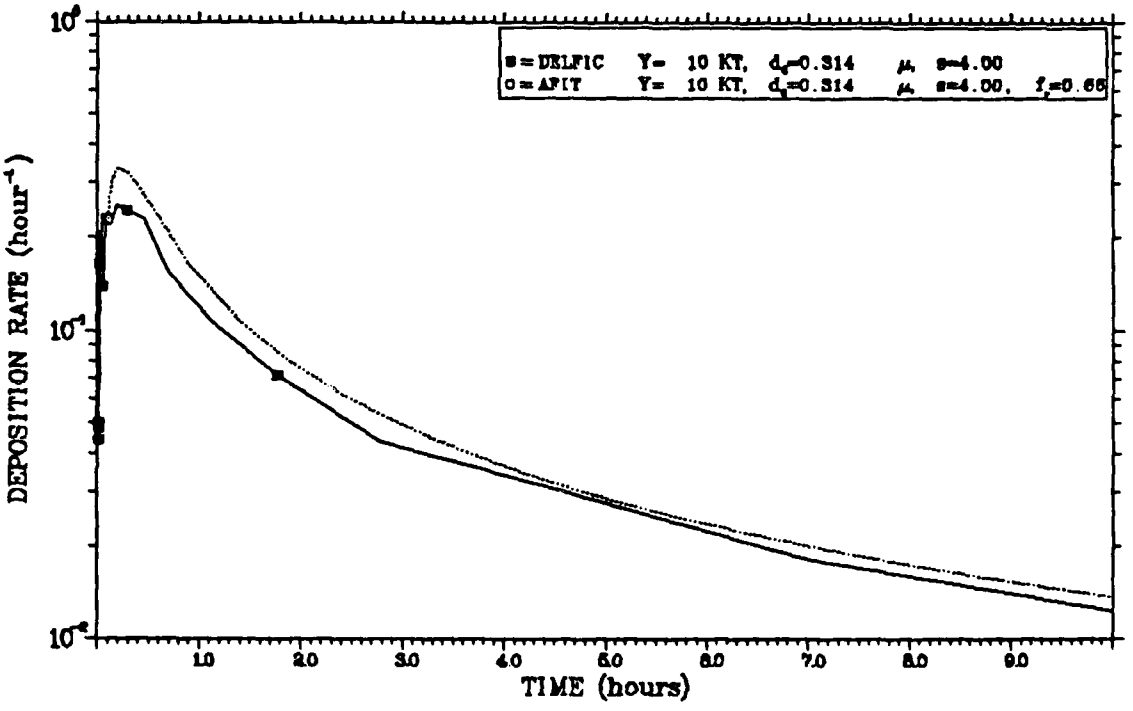

Figure C-13 Deposition Rates for the LYSTND Distribution

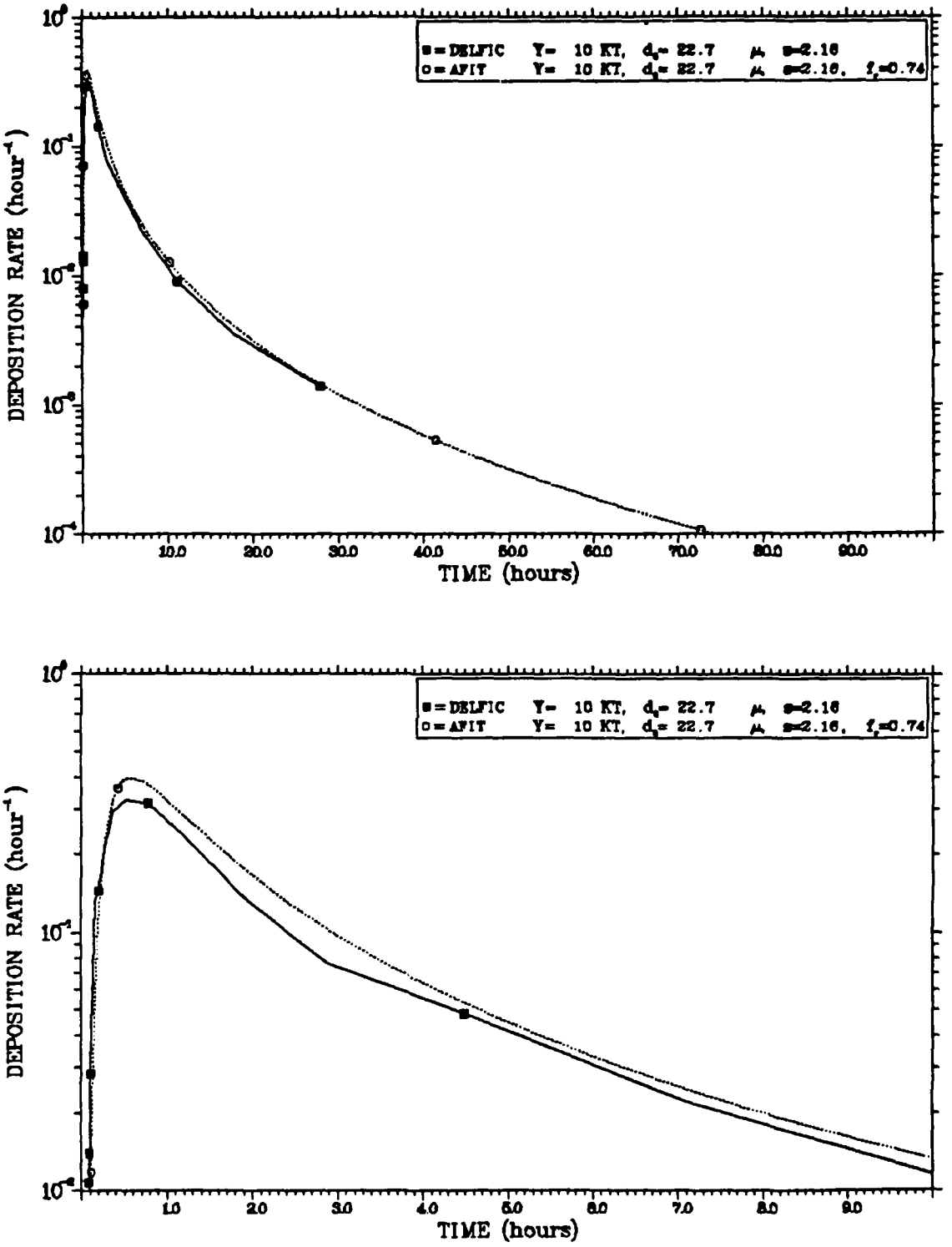

Figure C-14 Deposition Rates for the HYSTND Distribution

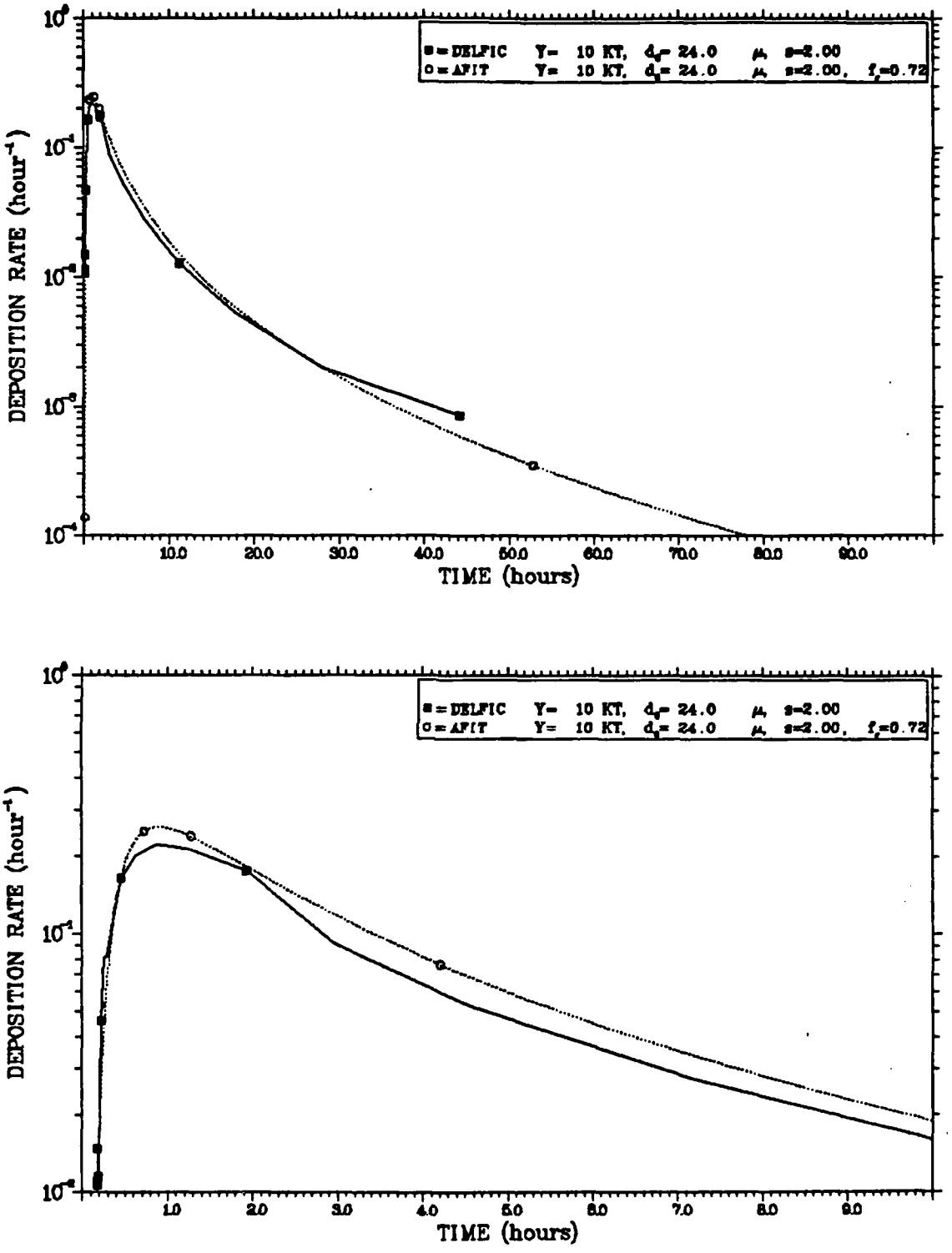

Figure C-15 Deposition Rates for the WSEG-10 Distribution

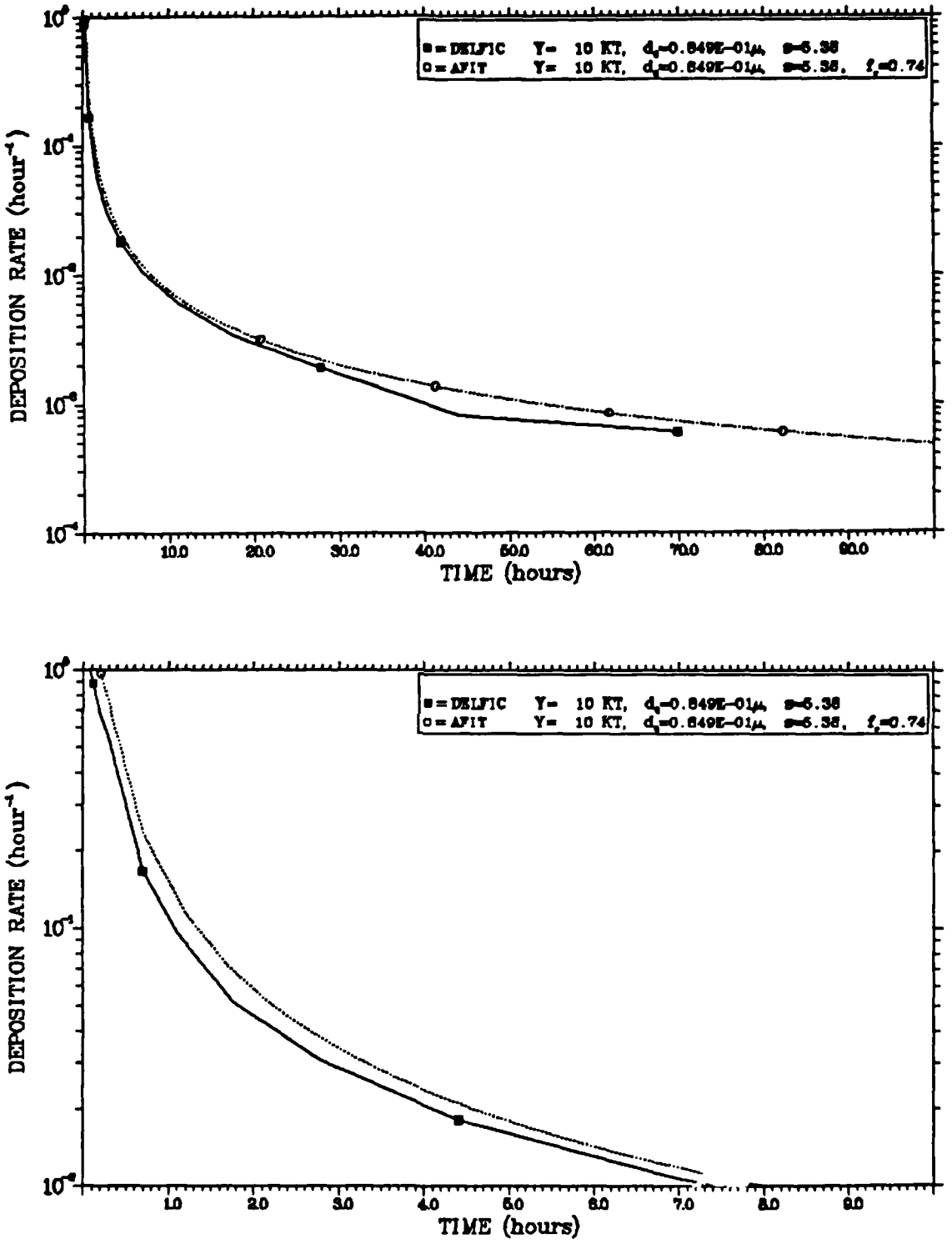

Figure C-16 Deposition Rates for the NRDLC61 Distribution

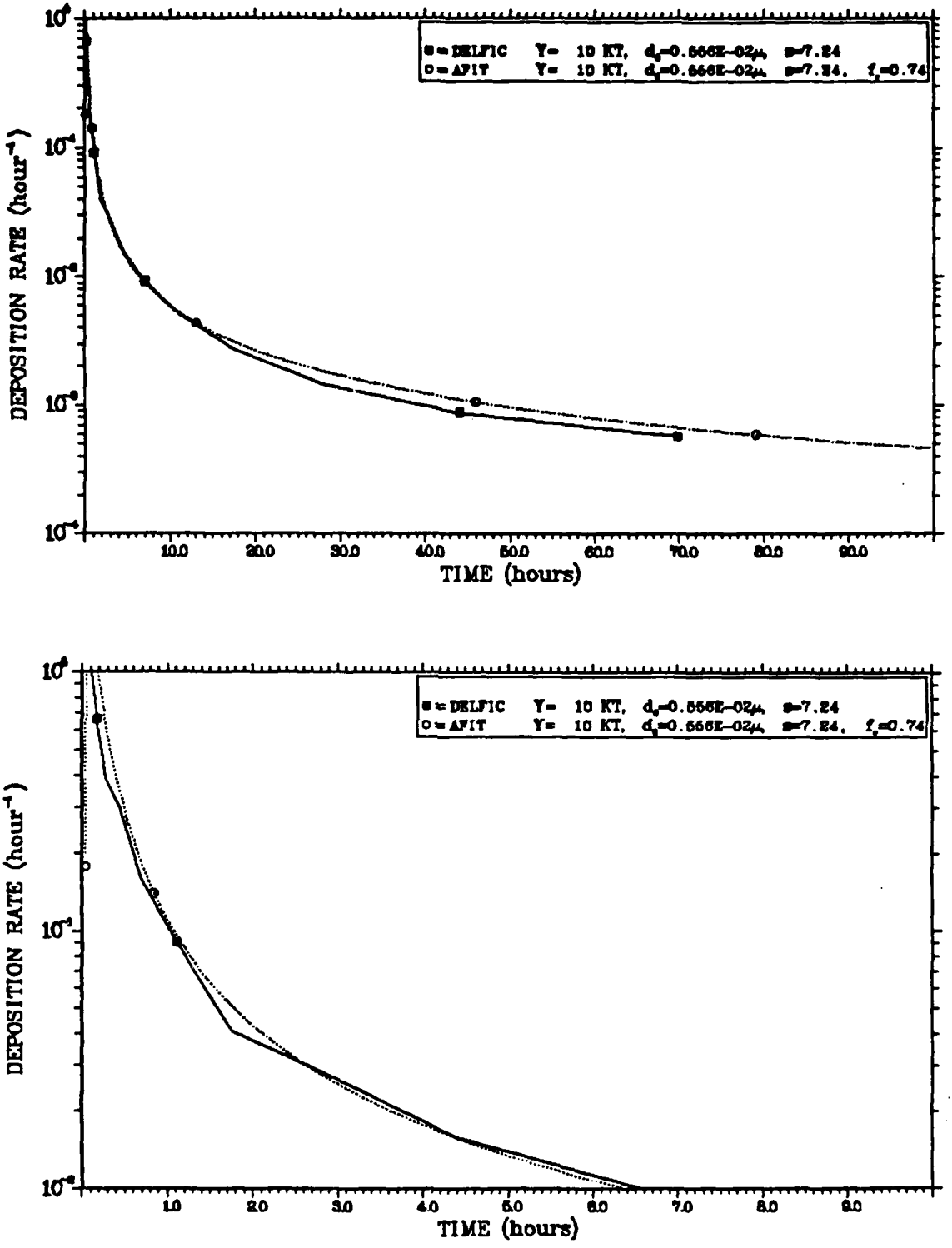

Figure C-17 Deposition Rates for the NRDLN61 Distribution

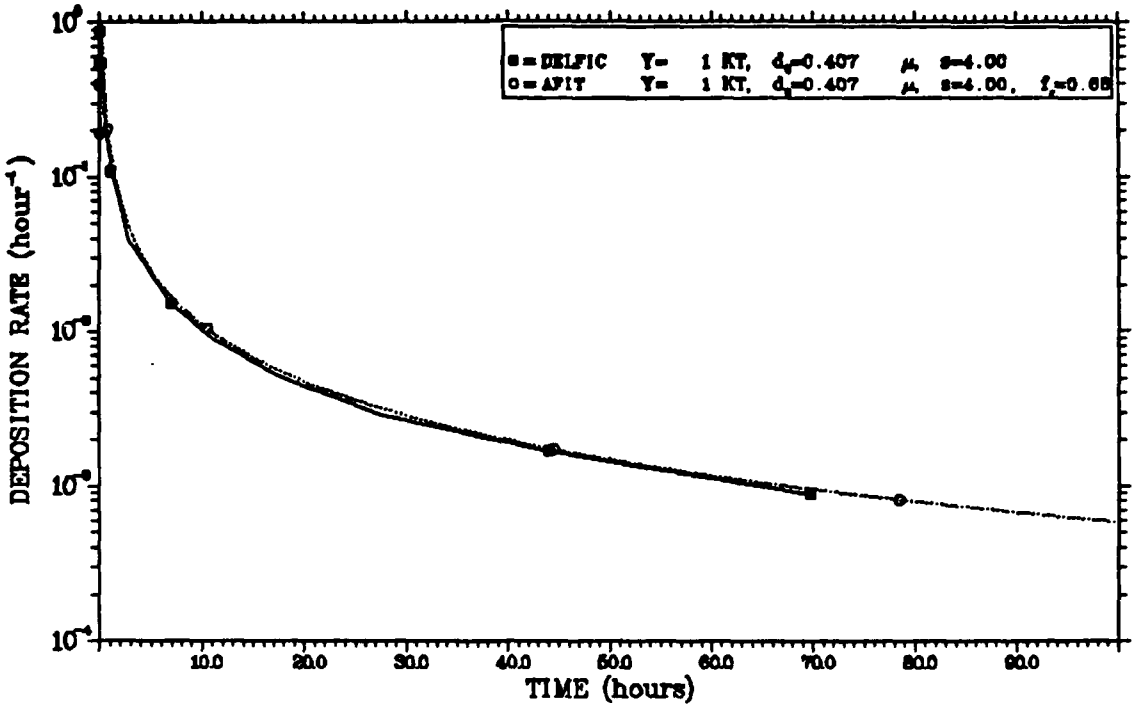

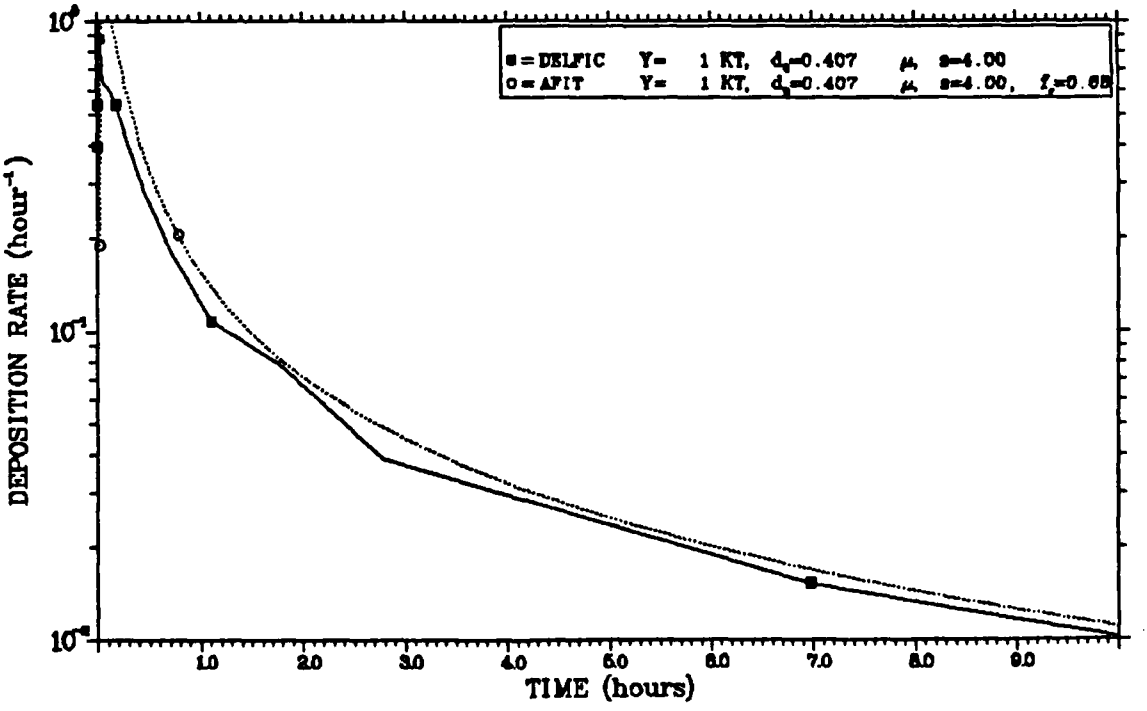

Figure C-18 Deposition Rates for the DEFAULT Distribution

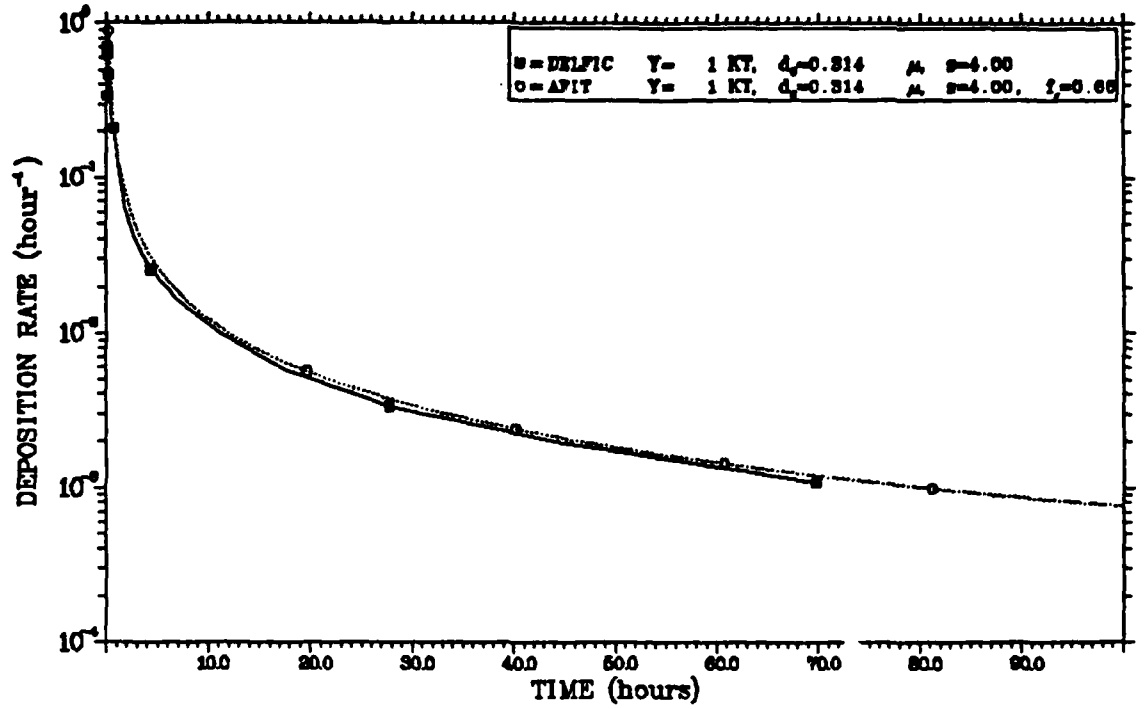

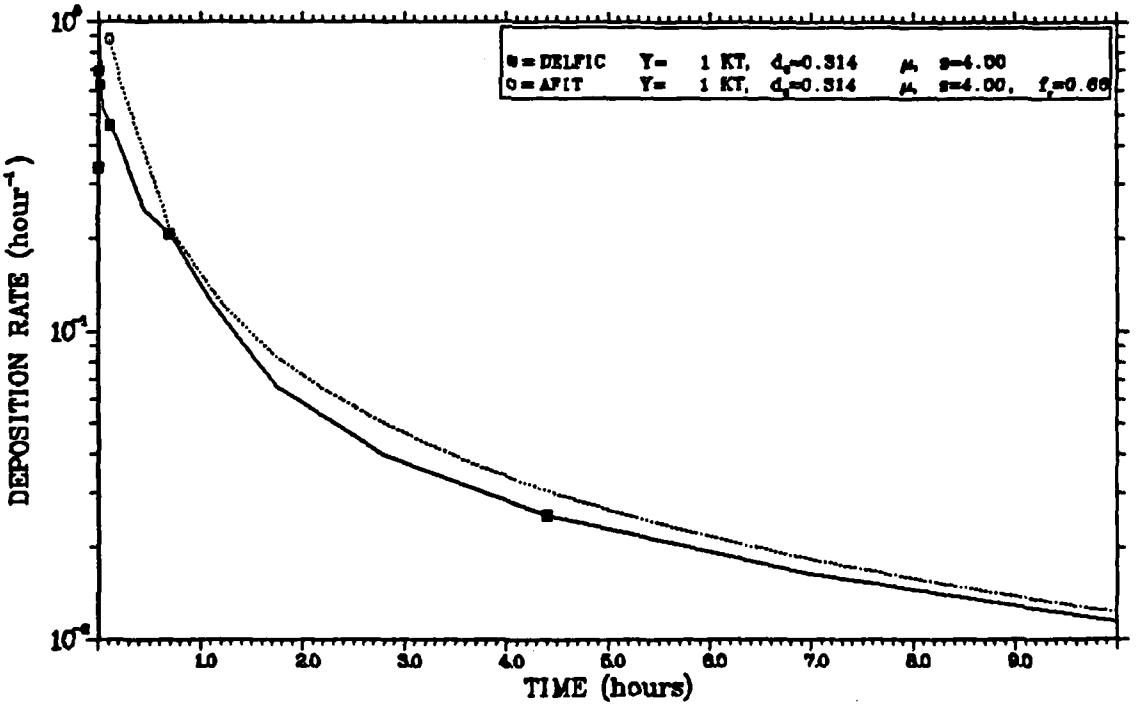

Figure C-19 Deposition Rates for the LYSTND Distribution

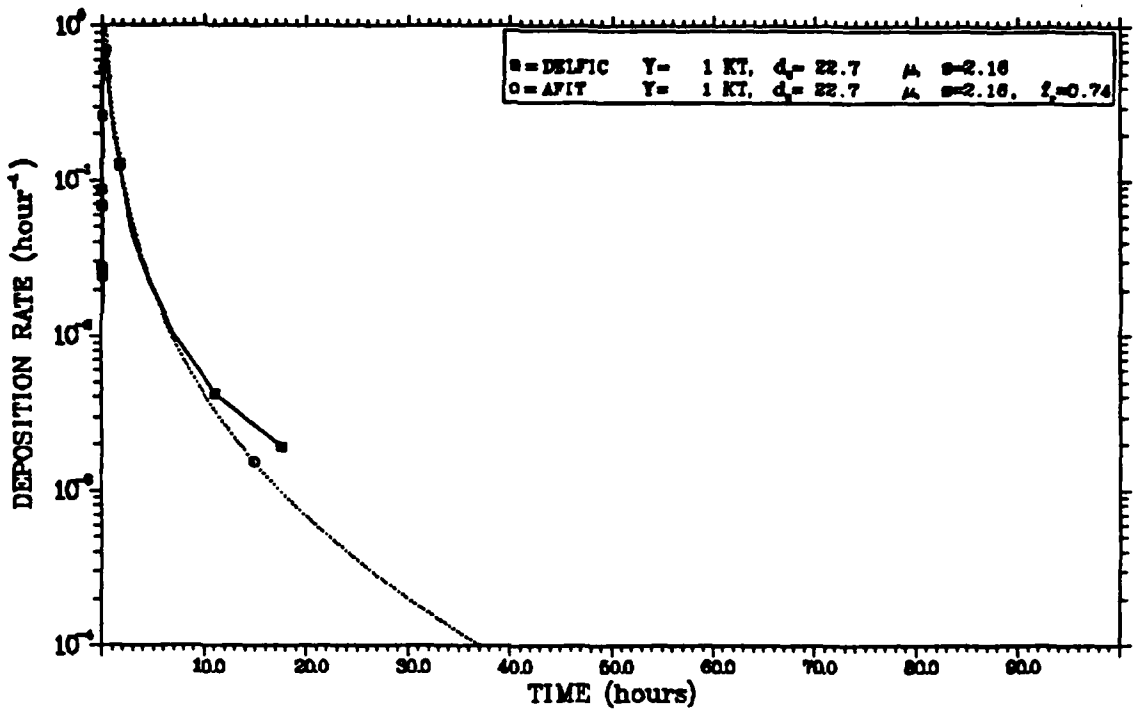

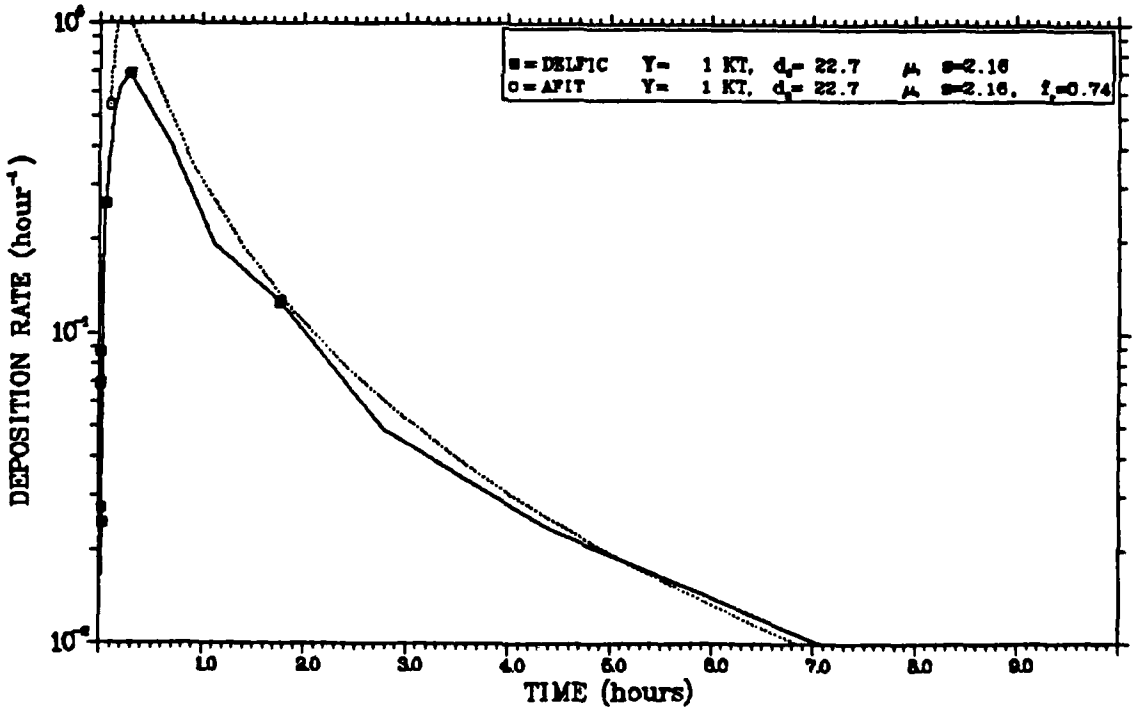

Figure C-20 Deposition Rates for the HYSTND Distribution

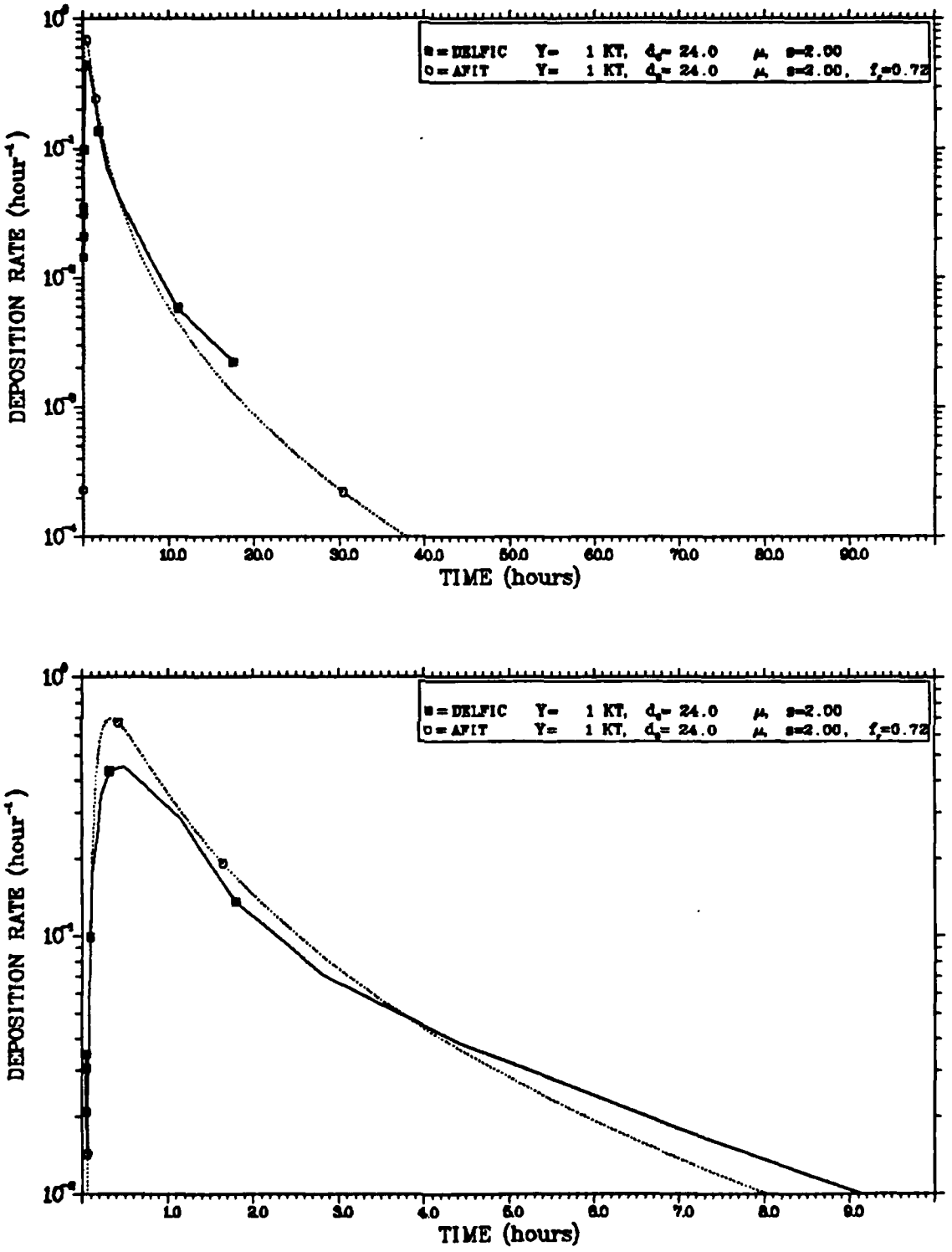

Figure C-21 Deposition Rates for the WSEG-10 Distribution

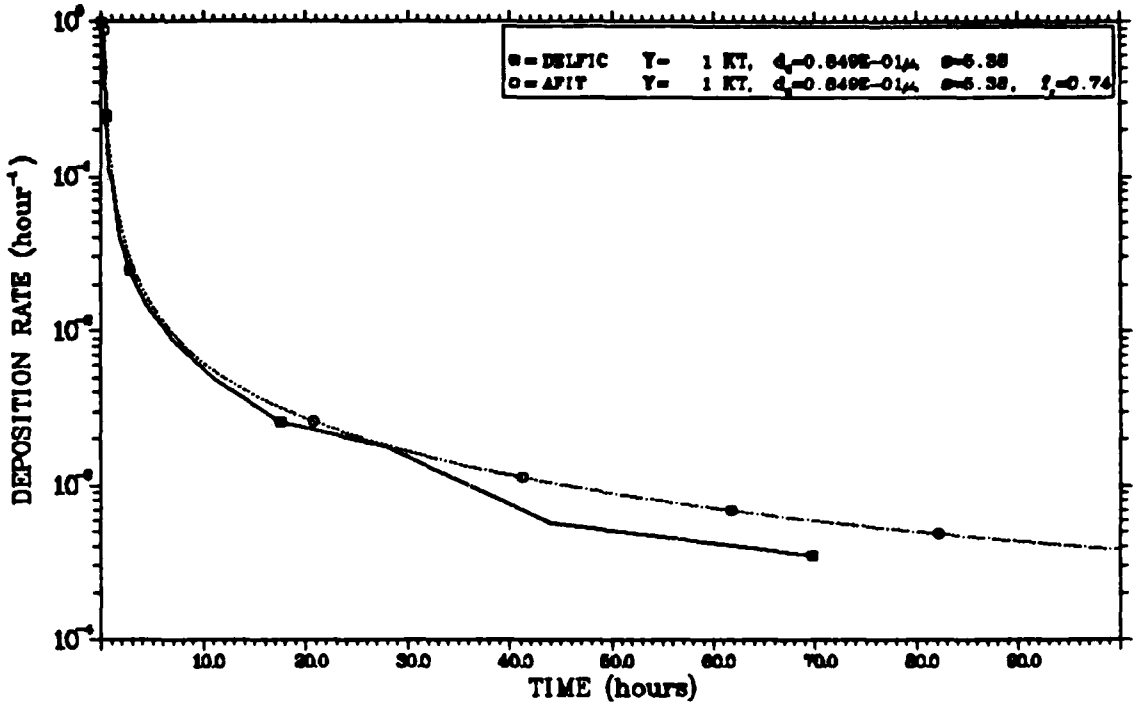

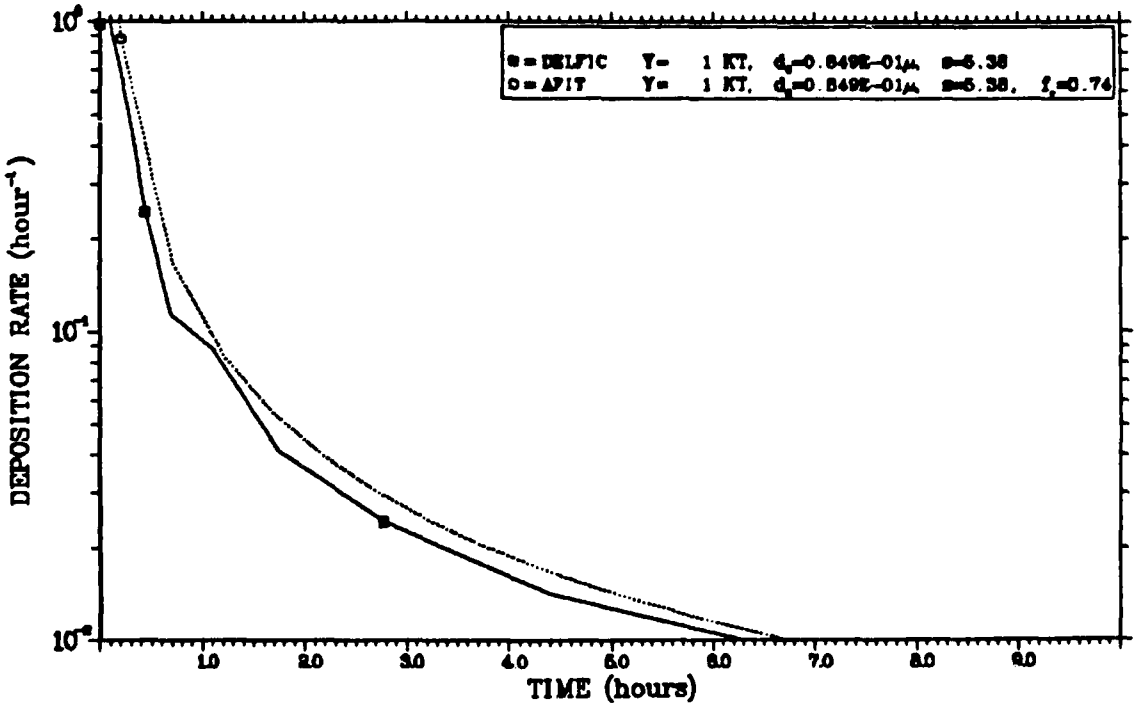

Figure C-22 Deposition Rates for the NRDLC61 Distribution

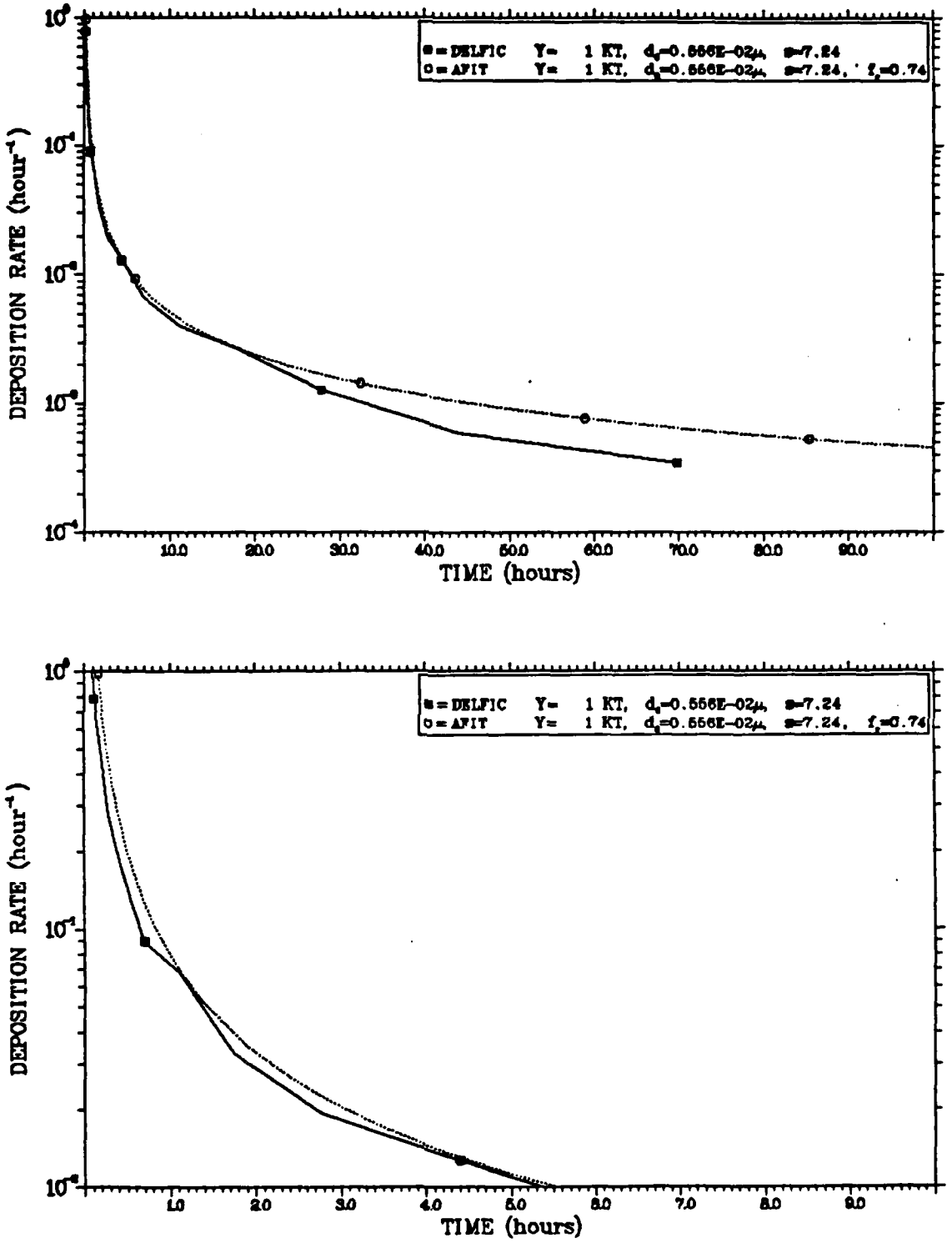

Figure C-23 Deposition Rates for the NRDLN61 Distribution

Bibliography

1. Norment H. G., 1979, "DELFIC: Department of Defense Fallout Prediction System, Volume I - Fundamentals". Report DNA 5159F-1, Atmospheric Science Associates for Defense Nuclear Agency, Washington DC 20305.

2. Kaplan I., 1962, "Nuclear Physics", 2nd ed., p. 242., Addison-Wesley, Inc., Reading, MA.

3. Norment H. G., 1977, "Analysis and Comparison of Fallout Prediction Models", DNA 4569F, Atmospheric Science Associates for Defense Nuclear Agency, Washington DC 20305.

4. Pugh G. E. and Galiano R. J., 1959, "An Analytical Model of Close-In Deposition of Fallout for Use in Operational Type Studies", WSEG Research Memorandum Report RM10, Weapon Systems Evaluation Group, The Pentagon, Washington, D.C.

5. Mason R. B., 1977, "Description of Mathematics for the Single Integrated Damage Analysis Capability (SIDAC)", National Military Command System Support Center, Technical Memorandum TM 15-73, The Pentagon, Washington DC 20301.

6. Horizons Technology HTI-78-R-109, 1978, "Nuclear Weapon Effects Programs: Reference Manual", Horizons Technology, Inc., 7830 Clairmont Mesa Blvd., San Diego, CA (Defense Nuclear Agency, Washington DC 20305,

Contract No. DNA 001-78-C-0247).

7. Norment H. G., 1978, "Evaluation of Three Fallout Models: DELFIC, SEER and WSEG-10", Atmospheric Science Associates, Bedford MA. Draft dated 28 Apr 78 for Defense Nuclear Agency.

8. Russell I. J., 1966, "A Critique of Land-Surface Fallout Models", p.209. Report AFWL-TR-65-76, Air Force Weapons Laboratory, Kirtland AFB NM.

9. Polan M., 1968, "An Analysis of the Fallout Prediction Models Presented at the USNRDL-DASA Fallout Symposium of September 1962, Vol. I: Analysis, Comparison and Classification of Models", p. 31. Report USNRDL-TRC-68, U.S. Naval Radiological Defense Laboratory, San Francisco, CA.

10. Bridgman C. J. and Bigelow W. S., 1982, "A New Fallout Prediction Model," Health Physics Vol. 43, No. 2, 207.

11. Glasstone S. and Dolan P. J., 1977, "The Effects of Nuclear Weapons", p. 391. U.S. Government Printing Office, Washington DC 20402, 3rd Ed.

12. Pugh G. E., 1960, "Revision of Fallout Parameters for Low-Yield Detonations", Supplement to WSEG Research Memorandum No. 10, Weapon System Evaluation Group, The Pentagon, Washington DC.

13. McDonald J. E., 1960, "An Aid to Computation of Terminal Fall Velocities of Spheres", Journal of Meteorology 17, 463.

14. Davies C. N., 1945, "Definitive Equations for the Fluid Resistance of Spheres", Proc. of the Physical Society, London 57, 259-270.

15. Schwenke T. W., Kohlberg I., Norment H. G. and Ing W. Y. G., 1967, "Department of Defense Land Fallout Prediction System, Vol. IV. Atmospheric Transport", p. 6. Report DASA-1800-IV, Defense Nuclear Agency, Washington DC 20305.

16. Colarco R. F., 1980, "A Computer Fallout Model for Operational Type Studies", M.S. Thesis, Air Force Institute of Technology, Wright-Patterson AFB, OH.

17. Batten E. S., Iglehart D. L. and Rapp R. R., 1960, "Derivation of Two Simple Methods for the Computing of Radioactive Fallout", Report RM 2460, The RAND Corporation, Santa Monica, CA.

18. Freiling E. C., 1963, "Fractionation III. Estimation of Degree of Fractionation and Radionuclide Partition for Nuclear Debris", p. 6. U.S. Naval Radiological Defense Laboratory Report USNRDL-TR-680, San Francisco CA.

19. Aitchison J. and Brown J. A. C., 1957, "The Lognormal Distribution", p. 12. Cambridge, Cambridge University Press.

20. Hopkins A. T., 1982, "A Two-Step Method to Treat Variable Winds in Fallout Smearing Codes", M.S. Thesis, Air Force Institute of Technology, Wright-Patterson AFB, OH.

21. Norment H. G., 1968, "Deposition Pattern Sensitivity Analysis of

the Defense Land Fallout Interpretive Code (DELFIC)", p. 25. Report DASA-2328, Defense Nuclear Agency, Washington DC 20305.

VITA

Major Winfield Scott Bigelow, Jr. was born on [redacted] in [redacted]. He graduated from [redacted] in 1962, and attended Union College, Schenectady, New York, from which he received the Bachelor of Science in Chemistry in 1966. He received a regular commission in July 1966, and began active duty as a student at the Air Force Institute of Technology. He received his Master of Science degree in Nuclear Engineering in July 1968. His thesis, "Photon Transport from a Point Source in the Atmosphere", employed a polynomial reconstruction of the flux distribution from its spatial moments. From July 1968 to December 1970, he served as a Nuclear Research Officer, working in alpha and gamma spectroscopy at the McClellan Central Laboratory, 1155th Technical Operations Squadron, McClellan AFB, California. Major Bigelow attended Squadron Officers' School from January 1971 to April 1971. From May 1971 until May 1976, he was assigned to Detachment 407, 1156th Technical Operations Squadron, where he served as Laboratory Chief. Major Bigelow returned to the Air Force Institute of Technology as a doctoral student in July 1976.

REPORT DOCUMENTATION PAGE

1a. REPORT SECURITY CLASSIFICATION: UNCLASSIFIED	1b. RESTRICTIVE MARKINGS
2a. SECURITY CLASSIFICATION AUTHORITY	3. DISTRIBUTION/AVAILABILITY OF REPORT: Approved for public release; distribution unlimited
2b. DECLASSIFICATION/DOWNGRADING SCHEDULE	
4. PERFORMING ORGANIZATION REPORT NUMBER(S): AFIT/DS/PH/83-2	5. MONITORING ORGANIZATION REPORT NUMBER(S)
6a. NAME OF PERFORMING ORGANIZATION: School of Engineering, Air Force Institute of Technology; 6b. OFFICE SYMBOL (If applicable): AFIT/EN	7a. NAME OF MONITORING ORGANIZATION
6c. ADDRESS (City, State and ZIP Code): Wright-Patterson AFB, Ohio 45433	7b. ADDRESS (City, State and ZIP Code)
8a. NAME OF FUNDING/SPONSORING ORGANIZATION: Defense Nuclear Agency; 8b. OFFICE SYMBOL (If applicable): HQ DNA/STBE	9. PROCUREMENT INSTRUMENT IDENTIFICATION NUMBER
8c. ADDRESS (City, State and ZIP Code): Washington, DC 20305	10. SOURCE OF FUNDING NOS.

PROGRAM ELEMENT NO.	PROJECT NO.	TASK NO.	WORK UNIT NO.
62704H	V990AXNA0	11	11

11. TITLE (Include Security Classification): FAR FIELD FALLOUT PREDICTION TECHNIQUES

12. PERSONAL AUTHOR(S): Winfield Scott Bigelow, Jr., Major, USAF

13a. TYPE OF REPORT	13b. TIME COVERED	14. DATE OF REPORT (Yr., Mo., Day)	15. PAGE COUNT
PhD Dissertation	FROM _____ TO _____	1983, December	152

16. SUPPLEMENTARY NOTATION

17. COSATI CODES			18. SUBJECT TERMS (Continue on reverse if necessary and identify by block number)	
FIELD	GROUP	SUB. GR.		
18	H		Fallout modeling	Nuclear weapons effects
15	F		Fallout prediction	Nuclear weapons debris
			Analytical model	Radioactive contamination

19. ABSTRACT (Continue on reverse if necessary and identify by block number)

Chairman of Advisory Committee: Dr. Charles J. Bridgman

[illegible] 7 Feb 84
Dean [illegible] Professional Development
Air Force Institute of Technology (AIC)
Wright-Patterson AFB OH [illegible]

20. DISTRIBUTION/AVAILABILITY OF ABSTRACT	21. ABSTRACT SECURITY CLASSIFICATION
UNCLASSIFIED/UNLIMITED ☒ SAME AS RPT. ☐ DTIC USERS ☐	UNCLASSIFIED

22a. NAME OF RESPONSIBLE INDIVIDUAL	22b. TELEPHONE NUMBER (Include Area Code)	22c. OFFICE SYMBOL
Dr. Charles J. Bridgman, Associate Professor	513-255-2012	AFIT/ENP

DD FORM 1473, 83 APR EDITION OF 1 JAN 73 IS OBSOLETE.

19. ABSTRACT

A calculational technique for use in predicting fallout far downwind from nuclear bursts is developed and validated. Numerical fallout models currently available cannot be extended to arbitrarily large downwind distances because of the artificial pattern break up inherent in their numerical quadrature. Two approaches to this problem are taken here. First, a numerical smoothing which conserves radioactivity is developed to help prevent pattern break up. This eliminates downwind pattern voids, but cannot eliminate artificial pattern structure. The second approach is to abandon the numerical quadrature and adopt a whole cloud smearing approach. The key function needed for this approach, the fractional arrival rate of activity on the ground, is derived from physical principles and validated by comparison with detailed numerical predictions. The prediction of activity arrival rate appears to be successful; the smearing model results agree with the numerical method over a wide range of weapon yields and activity distributions. This function is also employed in a limited sensitivity study of particle size-activity distribution effects on the ground arrival rate of activity. This sensitivity study confirms that the range of carrier soil particle sizes available and the distribution of bomb activity over those particles is crucial in establishing the time history of fallout arrival.